Modeling curvature effects on turbulence for turbomachinery flows

Roberto Suarez Raspopov

Master of Science Thesis

TU Delft Delft University of Technology

Mechanical, Maritime and Materials Engineering

Modeling curvature effects on turbulence for turbomachinery flows

Master of Science Thesis

For the degree of Master of Science in Mechanical Engineering: Sustainable Process and Energy Technology at Delft University of Technology

Roberto Suarez Raspopov

July 11, 2013

Faculty of Mechanical, Maritime and Materials Engineering (3mE) · Delft University of Technology

Delft University of Technology
Department of
Energy Technology

The undersigned hereby certify that they have read and recommend to the Faculty of Mechanical, Maritime and Materials Engineering (3mE) for acceptance a thesis entitled

Modeling curvature effects on turbulence for turbomachinery flows

by

Roberto Suarez Raspopov

in partial fulfillment of the requirements for the degree of

Master of Science Mechanical Engineering: Sustainable Process and Energy Technology

Dated: July 11, 2013

Supervisor(s):

Dr.Ir. Rene Pecnik

Ir. Enrico Rinaldi

Reader(s):

Prof.Dr.Ir. Bendiks Jan Boersma

Dr.Ir. Arvind Gangoli Rao

Abstract

Turbulent flows that are subject to streamline curvature and rotation experience additional forces that can enhance or suppress turbulence. A particular case where streamline curvature and rotation play an important role is in flows over aircraft engine components; such as: flows over compressor and turbine blades, flows around the spinning discs carrying the blades in axial turbines, flows in cooling channels of rotating blades, and flows over curved diffuser passages between compressor and turbine stages. The turbulence in a boundary layer entering a convex curve is diminished by the centrifugal acceleration while the turbulence of a flow entering a concave surface is amplified. These changes in the turbulence levels can significantly affect the nature of the flow, and in particular, the laminar-to-turbulent transition process. The boundary layer transition typically occurs around compressor and turbine blades, which consist of a concave surface (pressure side) and a convex surface (suction side). The transition phenomena can significantly affect the frictional losses, efficiency, and heat transfer over the component. Therefore, further improvements in the engine performance require a thorough understanding of the curvature effects in the boundary layer development.

This thesis presents an analysis of the curvature effects on turbulent flows for turbomachinery applications and it documents the improvement in their prediction capability by standard turbulence and transition models coupled with a curvature correction term on a series of two dimensional flows. For this purpose, an in-house Reynolds-Averaged Navier-Stokes (RANS) solver [18] is used, and the curvature correction proposed by Spalart and Shur [12] is implemented in the $k-\omega$ shear stress transport (SST) model of Menter [19] and the $\gamma - Re_{\theta t}$ (ReT) transition model of Langtry and Menter [8].

The curvature correction is first validated on two well known test cases, namely a subsonic flow over an adiabatic flat plate [22], and the fully turbulent flow inside a U-duct channel [23, 11]. As expected, the results for the flat plate indicate that the curvature correction term has no effect on the solution. For the U-duct test case, the solution obtained from the curvature corrected SST model is closer to the experimental data than the original SST.

Next, the performance of the curvature correction is analyzed for two well documented turbomachinery test cases. The first one being the prediction of the heat transfer coefficient over a Von Karman Institute (VKI) transonic turbine guide vane [3], and the second the prediction of the pressure coefficient over the high lift T106 low pressure turbine blade [21]. For the VKI

test case, two different flow configurations are considered, both characterized by the presence of boundary layer transition over the suction side of the profile. The results obtained from the curvature corrected SST and the original SST models overestimate the heat transfer coefficient over the surface of the blade, and, in general, are not able to capture the transition. On the other hand, the ReT transition model is able to predict laminar-to-turbulent transition over the suction side. Moreover, when combined with curvature correction, the ReT model predicts the transition onset closer to the experimental data, providing a much more accurate calculation of the heat transfer coefficient.
Finally, for the T106 turbine blade two flow configurations with different turbulence intensities are considered. In the case of high freestream turbulence, transition occurs before the boundary layer separates. However, for the lower freestream turbulence case the boundary layer separates and transition occurs in the shear layer above the laminar separation bubble. Here, the transition model is essential for the predictive capability of the simulation and the results are in good agreement with experimental data. For the two different flow configurations no significant improvements are observed when using the curvature correction term.

Table of Contents

List of Figures

List of Tables

Acknowledgements

First, I want to thank my father and friend, Dr. Raúl Suárez Parra for providing me with the necessary education and support to pursue my dreams.
I have to thank my supervisor, Dr.Ir. Rene Pecnik for giving me the chance of working with him and providing me with the necessary guidance and support in order to finish this project. This thesis has been an important learning experience for me and has fulfilled my expectations.
I want to thank my daily supervisor, Ir. Enrico Rinaldi for his valuable assistance during the development of my thesis.
I am also grateful to Dr.Ir. Piero Colonna for his advice and support during the last year of my Master studies.
I want to thank the close friends I have made during my stay in the Netherlands, and in particular, Horacio Jimenez, Eduardo Allison and Hugo Cruz for sharing with me their experience, and showing me life from a different perspective.
Finally, I have to acknowledge the "Consejo Nacional de Ciencia y Tecnología" (CONACyT), for providing me with the financial support necessary to perform my Master studies in the Netherlands.

Delft, University of Technology — Roberto Suarez Raspopov
July 11, 2013

Chapter 1

Introduction

1-1 Motivation

In aircraft engines, especially in turbomachinery components, the Reynolds numbers that determine the evolution of the boundary layers are relatively low, hence a large part of the flow along the blades surface is laminar or transitional. The boundary layer development, losses, efficiency, and heat transfer are greatly affected by the location and extent of the laminar-to-turbulent transition. The ability to accurately predict the transition process is therefore crucial for the design of efficient and reliable machines [4].

The main goal of gas turbine development is to increase its thermodynamic performance which depends on several factors such as the turbine inlet temperature, the selection of the optimal compression ratio and system configuration (intercasing cooling, regeneration, etc). However, nowadays the most substantial source of improvement comes from increasing the turbine inlet temperature, which affects both the specific power and thermal efficiency of the cycle [5]. The development in this area has been possible due to the progress in material engineering, however, the temperatures are so high nowadays that the improvement of material performance and specific design of new materials is not sufficient and the application of cooling systems for the hot components is necessary. The cooling of gas turbine vanes demands for accurate estimates of the cooling system location within the components and the amount of cooling needed in order to achieve an economical use of the available cooling air supply. In addition, there is a trend towards achieving a higher power output per stage, necessitating larger turning angles in cascades. For these reasons, designers have to understand the development of the boundary layers on turbine airfoils to obtain as much information as possible to mitigate the frictional losses and heat transfer. Despite the technical maturity of gas turbines, the research, optimization and development concerning this technology still continues, as increasing the engine's performance by a small amount or improving the cooling system provides substantial economic benefits.

1-2 Laminar to Turbulent Transition

The heat transfer and boundary layer separation strongly depend on the condition of the boundary layer. In a turbulent boundary layer, heat transfer and friction losses can be about five times higher than in a corresponding laminar boundary layer. In general, boundary layers always change from a laminar to a turbulent state, whereby this process is called laminar to turbulent transition. The location and extent of the transition process depend on the Reynolds number, the freestream turbulence intensity, the pressure gradient and geometry of the walls.

In practice, there are three important modes of laminar to turbulent transition. The first mode is called *natural transition*, which starts with a weak instability in the laminar boundary layer and continues through various stages of amplified instability until the flow is fully turbulent. The second mode is called *separated flow transition* which occurs in a separated laminar boundary layer. The third mechanism is called *bypass transition* and is caused by large disturbances in the external flow such as freestream turbulence. This is the most common mode of transition in gas turbine engines.

At present, there are mainly three concepts used to model transition in industry [6]. The first one is the application of low Reynolds number turbulent models, which are relatively easy to implement and in some cases are capable of predicting transition in three dimensional flows. Low Reynolds number turbulence models employ damping functions that are designed to predict the viscous sublayer behaviour. These models do not require wall functions. In order to predict transition they rely on the diffusion of turbulence from the freestream into the boundary layer and the interaction of this freestream turbulence with the model source terms [7]. On the other hand, a few of these models were found to predict transition at reasonable Reynolds numbers when the freestream turbulence level was sufficiently high. The ability of these models to predict transition seems to be coincidental and is due to the similarities between the viscous sublayer and the developing laminar boundary layer where the production of turbulence is damped.

The second approach is the so called e^N method, which is based on the local, linear stability theory and the parallel flow assumption in order to calculate the growth of the disturbance amplitude from the boundary layer neutral point to the transition location. It requires three successive steps: the first step consists of the calculation of the laminar velocity and temperature profiles along the body of interest. In the second step the local growth rates of the unstable waves are computed for each of these profiles. This can be accomplished by solving either the local stability equations or the Parabolized Stability Equations (PSE). In the third step, the local growth rates are integrated along each stream line in order to determine the N factor. Once the disturbance amplitude ratio (e^N) exceeds the limiting N factor transition is assumed to start. One issue with the e^N method is that the N factor does not represent the amplitude of a disturbance in the boundary layer, but rather the amplification factor from an initial unknown amplitude. This initial amplitude of the disturbance is related to external disturbance environment through an unknown receptivity process. For this reason, the limiting factor N must be determined by calibration to wind tunnel or flight tests making from the e^N approach a semi-empirical method. However, there are several drawbacks in applying the e^N method in general aerospace applications. The first is that since it is based on the linear stability theory, it cannot predict transition due to non-linear effects such as bypass transition or surface roughness induced transition. In addition, the need to track the

growth of the disturbance amplitude ratio along the streamline results in a significant issue for 3D flows where the streamline direction is not aligned with the grid [7].

The third approach for predicting transition, which is favoured by the gas turbine industry, is the use of experimental correlations. The empirical correlations usually relate the freestream turbulence intensity Tu to the transition Reynolds number based on the momentum thickness Reynolds number $Re_{\theta t}$. These correlations are attractive because they have been successfully used for several years and provide consistent results even when used in 3D structured Navier-Stokes codes. In order to employ an empirical correlation for a transition onset, the laminar solution around the body of interest must be first calculated. In a second step the boundary layer quantities are integrated to obtain the momentum thickness Reynolds number Re_θ along the whole body. The transition onset is then assumed to occur at the position where the local value of $Re_{\theta t}$ exceeds the one predicted by the correlation. Once the starting location of the transition is determined, a turbulence model is turned on and the subsequent flow development is calculated.

While empirical correlation methods prove to be sufficiently accurate, they present numerical and programming drawbacks in Navier-Stokes codes. As mentioned before, for correlation based transition models it is necessary to compare the actual momentum thickness Reynolds number Re_θ to the transition value from the correlation $Re_{\theta t}$. This represents a difficult task in a Navier-Stokes environment since the boundary layer edge is not well defined and the integration will therefore depend on the implementation of a search algorithm. In addition, there are serious difficulties regarding the implementation of non-local formulations in modern CFD codes based on unstructured grids and massive parallel execution. Unstructured grids do not easily provide the infrastructure needed to integrate global boundary layer parameters because the grid lines normal to the surface cannot be easily identified. In the case of a general parallelized code, the boundary layer can be divided between different CPU domains making the integration very complex to perform in parallel. Despite the implementation difficulties, empirical correlation methods are very attractive, as they allow for the inclusion of experimental data and additional parameters that are believed to affect transition. As a consequence, the accuracy of the empirical correlations can be improved as better experimental data on transition becomes available, and for this reason empirical correlations remain as an attractive method for predicting transition [7].

In this work, the recent $\gamma - Re_{\theta t}$ transition model proposed by Langtry and Menter in Ref. [8] will be used. The central mechanism by which this model operates is the intermittency parameter γ, which is the fraction of time for which the flow is turbulent at a certain location in space. The formulation proposed by Langtry and Menter is based on two transport equations. The first is an equation of the intermittency used to trigger the transition process by controlling the production term of kinetic energy in the boundary layer. The second transport is formulated in terms of the transition onset Reynolds number $Re_{\theta t}$. Outside the boundary layer, the transported variable is forced to follow the value of $Re_{\theta t}$ provided by the experimental correlation which is then diffused into the boundary layer. By this mechanism, the strong variations of turbulence intensity and pressure gradient in the freestream can be taken into account. At every location of the flow the local vorticity Reynolds number is compared to the transition Reynolds number to determine if the transition criterion is satisfied. If the vorticity Reynolds number exceeds the local transition Reynolds number, a source term in the intermittency equation is activated and turbulence is produced. In chapter 2 a detailed description of this method is provided.

1-3 The Role of Computational Fluid Dynamics

The understanding of the laminar to turbulent transition is important to incorporate new modeling methods into Computational Fluid Dynamics (CFD) codes, which are an effective and powerful tool in the design of turbomachinery components and other aerospace devices where wall shear stress or wall heat transfer are of interest. Currently, the transition modeling largely limits the quality of CFD codes, and the error in the estimation of the onset and extent of the transition can affect the calculated machine efficiency by several percent and the component life by more than an order of magnitude [9]. An important feature of thin shear flows around turbomachinery components is the presence of significant streamline curvature and rotation. For example the flow over compressor and turbine blades, the flow around the spinning discs carrying the blades in axial turbines, and the flow over curved diffuser passages between the compressor and turbine. For these type of flows streamline curvature and rotation exert additional forces which can change the turbulence levels in a boundary layer. These changes in the turbulence levels can affect the process of laminar to turbulent transition, the heat transfer and frictional losses over a surface.

Despite a fast growth of computer power and more and more intensive use, the Reynolds averaged Navier-Stokes equations still remain as the most widely used modeling approach in industrial applications. At the present, it is widely thought that linear eddy-viscosity turbulence models fail to accurately predict (or even fail to predict them at all) the effects of surface curvature and rotation [10]. Further progress in this area is often associated with Reynolds stress models (RSMs) [11]. The explicit appearance of rotation and curvature terms in the turbulence equations is cited as the fundamental advantage of RSMs over the simpler eddy viscosity models (EVMs). However, these models are not robust enough for practical applications in complex geometries [12]. Therefore, an effective alteration of the simple EVMs to incorporate curvature effects represents the most practical solution to the problem.

1-4 Curvature Effects

The surface curvature can suppress or amplify turbulence, depending on whether is convex or concave. The turbulence level in a boundary layer entering a convex curve (like the suction side of a turbine guide vane) is diminished by the centrifugal acceleration, while the turbulence of a flow entering a concave surface (pressure side) is amplified [2].

In 1937, Clauser and Clauser [13] recognized by means of experiments that laminar flows in a concave surface become turbulent at lower Reynolds numbers than on flat or convex surfaces. In his work, Görtler [14] determined that the laminar boundary layer on a concave surface becomes unstable as a result of centrifugal forces. The instability results in a secondary flow in the form of counter-rotating vortices (see Fig. 1-1) with axes parallel to the direction of the mean flow [1]. Görtler vortices have been observed by Han and Cox [15] in cascade flows. Their experiments suggested that the presence of the vortices could account for the increased heat transfer experienced on the turbine pressure surfaces. At the present, many rotation and/or streamline curvature (RC) corrections have been suggested in the literature. Howard et al. [16] performed a numerical analysis to predict the flow in a straight, radial rotating channel or rectangular cross section. The two equation $k - \varepsilon$ model was employed, with alternative modifications to include the influence of Coriolis force on the turbulent kinetic energy. The

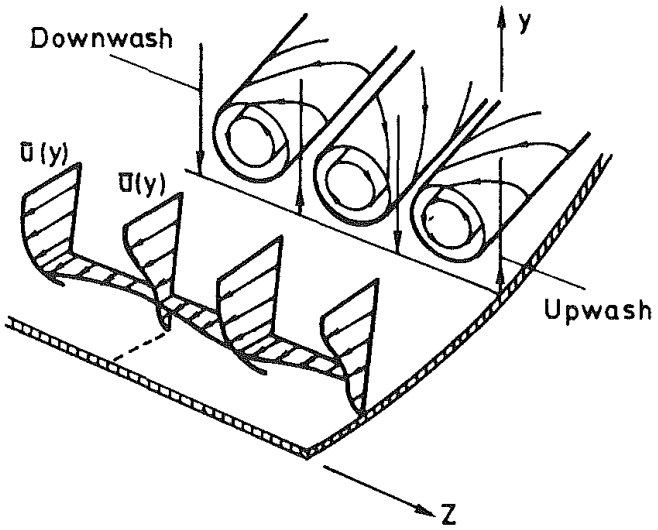

Figure 1-1: Görtler vortices in the boundary layer of a concave wall. (Adapted from Finnis and Brown [1].)

results shown moderate agreement with experimental data, confirming nevertheless the need for inclusion of Coriolis effects in the turbulence model.

Launder et al. [17] proposed an empirical coefficient to account for curvature effects which is directly proportional to the Richardson number Ri based on the eddy time scale (k/ϵ). The curvature correction term was implemented on the $k-\epsilon$ model by modifying the transport equation for the turbulent energy dissipation ϵ. The modified turbulence model was validated on a series of turbulent shear flows like the fully developed turbulent flow in a curved channel; and the boundary layer over a convex and concave surfaces. The results shown a moderate improvement over the results obtainable with the conventional $k-\varepsilon$ model.

Though the above mentioned corrections are moderately successful in the specific flows for which they were designed, they are still not universal, as they treat curvature and rotation differently, and, in addition, often suffer from Galilean non-invariance. In this work, the empirical function proposed by Spalart and Shur [12] to account for the effects of streamline curvature and rotation will be used. This correction term is based on intuitive arguments developed in thin shear layers, it is Galilean-invariant and fully defined in three dimensions.

1-5 Thesis Outline

The present work is concerned with curvature effects on the transition modeling over turbomachinery components. The curvature of a gas turbine guide vane can affect the extent an location of the laminar to turbulent transition over its surface. The purpose of this work is to improve the reliability of CFD calculations by incorporating the effect of surface curvature into the transition modeling. For this purpose, the Stanford University in-house Reynolds-Averaged Navier-Stokes (RANS) solver, developed by Pecnik et al. [18] is used. The curvature correction proposed by Spalart and Shur in Ref. [12] is implemented in the $k-\omega$ SST turbulence model coupled with the $\gamma - Re_{\theta t}$ transition model and the results of several test cases

are discussed.

The structure of this thesis is the following: in Chapter 2, a survey on turbulence modeling, transition and curvature effects is given. In chapter 3 the implementation of the curvature correction term in the RANS solver is discussed. Chapter 4 presents the results of implementing the curvature correction on four different test cases: a flat plate, a U-duct channel, the VKI turbine guide vane and the low pressure T106 blade profile. Finally, in Chapter 5 a brief summary and the conclusions of this thesis are given.

Chapter 2

Theoretical Framework

In the present chapter, a brief discussion of turbulence modeling, laminar to turbulent transition and curvature effects is provided. The $k-\omega$ SST turbulence model of Menter [19] and the $\gamma - Re_{\theta t}$ transition model proposed by Langtry and Menter [8] are presented. In addition, the modified Spalart and Shur correction term proposed by Smirnov and Menter [11] to account for curvature effects in turbulent flows is discussed.

2-1 Turbulence Modeling

The motion of a fluid is governed by the Navier Stokes equations. In the turbulent regime, the solution to these equations is a chaotic, three dimensional and unsteady. Such solutions are not easily obtained, even on massively parallel supercomputers. A much simpler level of description is required: this calls for a statistical approach. As it will be seen in the following, there are no closed equations for the statistics of turbulent flow, which means that there is a larger number of unknowns than equations. In the present survey only incompressible, constant density flow will be considered.

The equations governing incompressible flow, whether laminar or turbulent, are

$$\begin{aligned} \frac{\partial \tilde{u}_i}{\partial t} + \tilde{u}_j \frac{\partial \tilde{u}_i}{\partial x_j} &= -\frac{1}{\rho}\frac{\partial p}{\partial x_i} + \nu \nabla^2 \tilde{u}_i, \\ \frac{\partial \tilde{u}_i}{\partial x_i} &= 0. \end{aligned} \tag{2-1}$$

The first equation expresses the conservation of momentum. The second expresses the incompressibility of fluid volumes, which is equivalent to mass conservation in the present case. The total instantaneous velocity is denoted by $\tilde{u}$ and it can be decomposed in a mean velocity component U and a fluctuating component u, in other words $\tilde{u} = U + u$. The fluctuation u is usually referred to as the turbulence and U as the mean flow. If the previous decomposition

is substituted into Eqs. (2-1) they become

$$\begin{aligned} \frac{\partial}{\partial t}(U_i + u_i) + (U_j + u_j)\frac{\partial}{\partial x_j}(U_i + u_i) &= -\frac{1}{\rho}\frac{\partial}{\partial x_i}(P + p) + \nu\nabla^2(U_i + u_i), \\ \frac{\partial}{\partial x_i}(U_i + u_i) &= 0. \end{aligned} \tag{2-2}$$

The average of this equations is obtained by drawing a bar over each term, and considering that $\bar{U} = U$ and $\bar{u} = 0$:

$$\begin{aligned} \frac{\partial U_i}{\partial t} + U_j\frac{\partial U_i}{\partial x_j} &= -\frac{1}{\rho}\frac{\partial P}{\partial x_i} + \nu\nabla^2 U_i - \underbrace{\frac{\partial}{\partial x_j}\overline{u_j u_i}}, \\ \frac{\partial U_i}{\partial x_i} &= 0. \end{aligned} \tag{2-3}$$

These are the Reynolds-Averaged Navier-Stokes (RANS) equations. Equations (2-3) for the mean flow are the same as Eqs. (2-1), except for the last term of the momentum equation. This term is highlighted with an underbrace and corresponds to the derivative of the Reynolds stress tensor $\overline{u_i u_j}$.

The set of equations for the mean flow (2-3) define an unclosed mathematical problem because they are a set of four equations ($i = 1, 2, 3$) with ten unknowns (P; $U_i,\ i = 1, 2, 3$; and $\overline{u_j u_i},\ i = 1, 2, 3,\ j \leq i$). The extra six unknowns are the components of the Reynolds stress tensor. It is necessary to point out that the statistical problem (2-3) for the mean, or first moment requires knowledge of the covariance or second moment. This is because the Navier-Stokes equations have a quadratic non-linearity [2]. Any non-linearity causes moment equations to be unclosed; here the first moment equation contains second moments, the second moment equation will contain third moments.

The formulation of additional equations to obtain a solvable set of the Navier-Stokes equations (2-3) is called *closure modeling*. When the purpose is to predict non-homogeneous flow, possibly in complex engineering geometries, semi-empirical formulations to predict $\overline{u_i u_j}$ are required. In this work, an eddy viscosity model will be implemented. In this approach, the Reynolds stress tensor is explicitly related to the mean flow by a Newtonian constitutive equation with an eddy viscosity: $\overline{u_i u_j} = -2\nu_T S_{ij} + \frac{2}{3}\delta_{ij}k$. The term semi-empirical means that the model is obtained from a combination of theoretical analysis of simplified models, fluid mechanics, and experimental data. The semi-empirical model used here to calculate the eddy viscosity is the $k - \omega$ SST model and it will be described in detail in the following section.

2-2 The $k - \omega$ SST Model

The $k - \omega$ Shear Stress Transport model (SST) proposed by Menter in Ref. [19] utilizes the original $k - \omega$ model of Wilcox in the inner region of the boundary layer and switches to the standard $k - \epsilon$ model in the outer region and the free shear flow. In addition, it incorporates a modification of the definition of the eddy viscosity which accounts for the effect of the transport of the principal turbulent shear stress.

The $k-\omega$ model is chosen in the sublayer and the logarithmic part of the boundary layer since it has better performance than the $k-\epsilon$ model in equilibrium adverse pressure gradient flows and in compressible flows. On the other hand, the $k-\epsilon$ model is adopted in the wake region of the boundary layer and in free shear layers away from any surface. The reason is the high sensitivity of the $k-\omega$ model to the freestream values ω_f specified for ω outside the boundary layer.

In order to achieve the desired behaviour of the model in the different regions, the $k-\epsilon$ model is transformed into the $k-\omega$ formulation. It is then multiplied by the blending function $(1-F_1)$ and added to the original $k-\omega$ model times F_1. The blending function F_1 is designed to be zero in the wake region and to be one in the sublayer and the logarithmic region of the boundary layer. The original $k-\omega$ model is given by:

$$\frac{D\rho k}{Dt} = \tau_{ij}\frac{\partial U_i}{\partial x_j} - \beta^\star \rho\omega k + \frac{\partial}{\partial x_j}\left[(\mu+\sigma_{k1}\mu_t)\frac{\partial k}{\partial x_j}\right], \tag{2-4}$$

$$\frac{D\rho\omega}{Dt} = \frac{\gamma_1}{\nu_t}\tau_{ij}\frac{\partial U_i}{\partial x_j} - \beta_1\rho\omega^2 + \frac{\partial}{\partial x_j}\left[(\mu+\sigma_{\omega1}\mu_t)\frac{\partial \omega}{\partial x_j}\right]. \tag{2-5}$$

Next, the $k-\epsilon$ model is transformed into a $k-\omega$ formulation, where an additional cross-diffusion term appears in the ω equation. The transformed $k-\epsilon$ is given by

$$\frac{D\rho k}{Dt} = \tau_{ij}\frac{\partial U_i}{\partial x_j} - \beta^\star \rho\omega k + \frac{\partial}{\partial x_j}\left[(\mu+\sigma_{k2}\mu_t)\frac{\partial k}{\partial x_j}\right], \tag{2-6}$$

$$\frac{D\rho\omega}{Dt} = \frac{\gamma_2}{\nu_t}\tau_{ij}\frac{\partial U_i}{\partial x_j} - \beta_2\rho\omega^2 + \frac{\partial}{\partial x_j}\left[(\mu+\sigma_{\omega2}\mu_t)\frac{\partial \omega}{\partial x_j}\right] + 2\rho\sigma_{\omega2}\frac{1}{\omega}\frac{\partial k}{\partial x_j}\frac{\partial \omega}{\partial x_j}. \tag{2-7}$$

Now, Eqs. (2-4) and (2-5) are multiplied by F_1 while Eqs. (2-6) and (2-7) are multiplied by $(1-F_1)$ and the corresponding equations of each set are added to obtain the new model:

$$\frac{D\rho k}{Dt} = \tau_{ij}\frac{\partial U_i}{\partial x_j} - \beta^\star \rho\omega k + \frac{\partial}{\partial x_j}\left[(\mu+\sigma_{k}\mu_t)\frac{\partial k}{\partial x_j}\right], \tag{2-8}$$

$$\frac{D\rho\omega}{Dt} = \frac{\gamma}{\nu_t}\tau_{ij}\frac{\partial U_i}{\partial x_j} - \beta\rho\omega^2 + \frac{\partial}{\partial x_j}\left[(\mu+\sigma_{\omega}\mu_t)\frac{\partial \omega}{\partial x_j}\right] + 2*\rho(1-F_1)\sigma_{\omega2}\frac{1}{\omega}\frac{\partial k}{\partial x_j}\frac{\partial \omega}{\partial x_j}, \tag{2-9}$$

where any constant $\alpha \in (\sigma_{k1}, ...)$ is given by $\alpha = F_1\alpha_1 + (1-F_1)\alpha_2$, being α_1 and α_2 the constants of the original $k-\omega$ model and the transformed $k-\epsilon$ model respectively.

In order to account for the effect of the transport of the principal turbulent shear stress the eddy viscosity is redefined as

$$\nu_t = \frac{a_1 k}{\max(a_1\omega; \Omega F_2)}, \tag{2-10}$$

where a_1 is a constant, Ω is the absolute value of the vorticity and F_2 is a function that is one for boundary layer flows and zero for free shear layers.

2-3 Transition Prediction

The process by which a laminar flow turns into a turbulent one is called transition. The transition process and the important role played by the Reynolds number $Re = Ud/\nu$ in this transition was first pointed out by Reynolds in 1883. Reynolds was concerned with the water flow along a straight smooth pipe, where a filament of coloured fluid was introduced at the inlet (see Fig. 2-1). When the speed of the water was low, the filament remained distinct through the entire length of the tube. When the speed was increased, the filament broke up at a given point and diffused throughout the cross-section. In his paper, Reynolds distinguished these two flow regimes (laminar and turbulent) and he argued that the parameter that controlled the transition from wan regime to another had to be $Re = Ud/\nu$. He also noted that the critical value of Re at which turbulence first appears is very sensitive to disturbances at the entrance of the pipe.

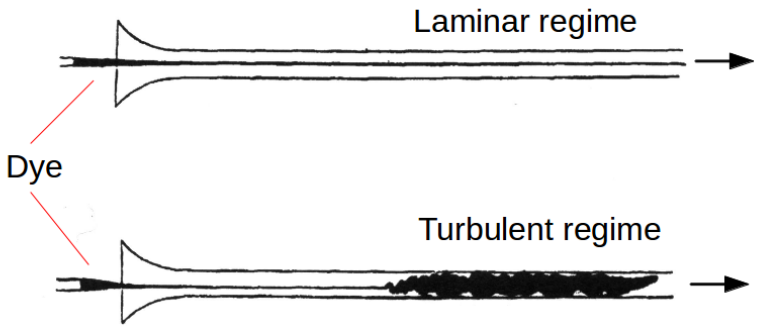

Figure 2-1: Schematic representation of Reynolds' observations in 1883. Reynolds distinguished two flow regime, laminar and turbulent, and he argued that the parameter that controlled the transition from wan regime to another had to be $Re = Ud/\nu$. (Adapted from Dubrin and Pettersson Reif [2].)

In general, there are three important modes of transition, natural, bypass and separated flow transition. Each one of these modes depends on the flow conditions such as the intensity of fluctuations in the freestream, roughness and geometry of the walls.

For the case of *natural transition*, it is presently known that it envolves several stages [20]. First, at a critical value of momentum thickness Reynolds number the boundary layer becomes susceptible to small disturbances and develops an instability in the form of a two dimensional Tollmien-Schlichting wave. Second, the instability amplifies in the layer to a point where three-dimensional instabilities grow and develop into loop vortices with large fluctuations. Finally, the highly fluctuating portions of the flow develop into turbulent spots, which then grow and convect downstream within the boundary layer to eventually merge into a fully developed turbulent boundary layer. In the case of *bypass transition*, at high freestream turbulence levels, the first and possibly the second stages of the natural transition are omitted (or bypassed) such that the turbulent spots are directly produced within the boundary layer by the influence of freestream disturbances. For this case, no Tollmien-Schlichting waves are

found.

Finally, when a laminar boundary layer separates, transition may occur in the free-shear-layer-like flow near the surface, this is called *separated flow transition*. In this case, the flow may reattach as turbulent forming a laminar separation/turbulent reattachment bubble on the surface. In gas turbines separated flow transition is common and may occur in an over-speed region near an airfoil's leading edge on either the suction side, the pressure side or both. Long bubbles can produce large losses and deviations in exit flow angles, for this reason they should be avoided. On the other hand, short bubbles are an effective way to force the flow to become turbulent and this can be considered as a means to control performance [20]. One of the difficulties in transition modelling is to predict whether the bubble will be large or short.

In order to predict the transition process one could rely directly on the turbulence model such as the $k-\omega$ SST which was described in the previous section. It is necessary to mention that most of the transport equation models such as $k-\epsilon$ and $k-\omega$ do converge to a laminar solution at low Reynolds numbers and to a turbulent solution at sufficiently high Reynolds number exhibiting a transition in between (see Fig. 2-2). However, turbulence models are in

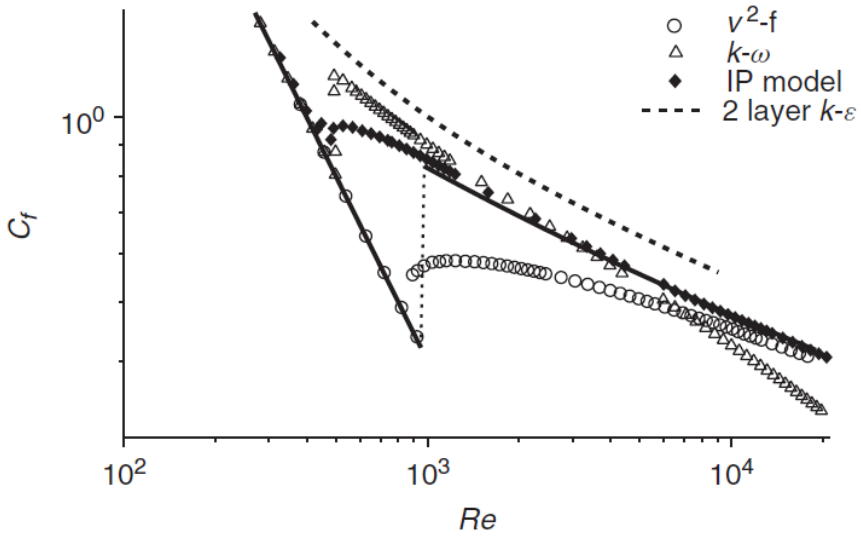

Figure 2-2: Skin friction coefficient in a plane channel versus Reynolds number based on the centerline velocity and channel half width. Many turbulence models display laminar to turbulent transition as the Reynolds number increases. (From Dubrin and Pettersson Reif [2].)

general developed for fully turbulent conditions and calibrated with turbulence data. Their ability to capture accurately the transition mechanism is a property of the model equations, not of the fluid dynamical mechanisms. For this reason, the prediction of laminar to turbulent transition provided by turbulence models is seriously limited and therefore a different approach is required. In this work, the recent $\gamma - Re_{\theta t}$ transition model proposed by Langtry and Menter [8] will be used. The central idea behind this model is to use an intermittency parameter γ to modulate the production of turbulent kinetic energy in the turbulence model. The intermittency γ takes values from 0 to 1 and represents the probability that a given point is located inside a turbulent region. A detailed description of the $\gamma - Re_{\theta t}$ transition model is provided in the next section.

2-4 The $\gamma - Re_{\theta t}$ Transition Model

In the present section the $\gamma - Re_{\theta t}$ correlation based transition model proposed by Langtry and Menter in [8] is described. This model is built strictly on local variables making it compatible with modern CFD techniques such as unstructured grids and parallel computation.

The $\gamma - Re_{\theta t}$ transition model is based on the transport equation for intermittency, which is used to trigger the transition locally. In addition, a second transport equation is solved for the transition onset momentum thickness Reynolds number $Re_{\theta t}$. This is required to capture the non-local influence of turbulence intensity, which changes due to the decay of the turbulence kinetic energy in the freestream, as well as to changes in the freestream velocity outside the boundary layer. This second transport equation ties the empirical correlation to the onset criteria in the intermittency equation.

The transport equation for intermittency is given by

$$\frac{\partial \rho\gamma}{\partial t} + \frac{\partial}{\partial x_j}(\rho U_j \gamma) = P_\gamma + E_\gamma + \frac{\partial}{\partial x_j}\left[\left(\mu + \frac{\mu_t}{\sigma_f}\right)\frac{\partial \gamma}{\partial x_j}\right]. \tag{2-11}$$

The transition source is defined as

$$P_{\gamma 1} = F_{lenght} C_{a1} \rho S \sqrt{\gamma F_{onset}}(1 - c_{e1}\gamma), \tag{2-12}$$

where S is the strain rate magnitude and F_{lenght} is an empirical correlation that controls the length of the transition region. This function is based on a series of flat plate test cases and is defined as

$$F_{lenght} = \begin{cases} 398.189 \cdot 10^{-1} + (-119.270 \cdot 10^{-4})\tilde{Re}_{\theta t} + (-132.567 \cdot 10^{-6})\tilde{Re}_{\theta t}^2, & \tilde{Re}_{\theta t} < 400 \\ 263.404 + (-123.939 \cdot 10^{-2})\tilde{Re}_{\theta t} + (194.548 \cdot 10^{-5})\tilde{Re}_{\theta t}^2 + (-101.695 \cdot 10^{-8})\tilde{Re}_{\theta t}^3 & 400 \leq \tilde{Re}_{\theta t} \leq 596 \\ 0.5 - (\tilde{Re}_{\theta t} - 596.0) \cdot 3.0 \cdot 10^4 & 596 \leq \tilde{Re}_{\theta t} < 1200 \\ 0.3188 & 1200 \leq \tilde{Re}_{\theta t} \end{cases}$$

The function F_{onset} is used to trigger the intermittency production (i.e. activate Eq. (2-12)). It is designed to switch rapidly from a value of zero in a laminar boundary layer to a value of one at every location in the flow field where the local vorticity Reynolds number exceeds the local transition onset criteria. The transition onset is controlled by the following equations:

$$Re_v = \frac{\rho y^2 S}{\mu} \; ; \; R_T = \frac{\rho k}{\mu \omega}, \tag{2-13}$$

$$F_{onset1} = \frac{Re_v}{2.193 \cdot Re_{\theta c}}, \tag{2-14}$$

$$F_{onset2} = \min(\max(F_{onset1, F_{onset1}^4}), 2.0), \tag{2-15}$$

$$F_{onset3} = \max\left(1 - \left(\frac{R_T}{2.5}\right)^3, 0\right), \tag{2-16}$$

$$F_{onset} = \max(F_{onset2} - F_{onset3}, 0). \tag{2-17}$$

$Re_{\theta c}$ in Eq. (2-14) is the critical Reynolds number where the intermittency first starts to increase in the boundary layer. This occurs upstream of the transition Reynolds number $\tilde{Re}_{\theta t}$ because there is a delay due to the fact that turbulence must first build up to appreciable levels in the boundary layer before any change in the laminar profile can occur. For this reason, $Re_{\theta c}$ can be thought of as the location where turbulence starts to grow while $\tilde{Re}_{\theta t}$ is

the location where the velocity profile first starts to deviate from the purely laminar profile. The connection between the two must be obtained from an empirical correlation were

$$Re_{\theta c} = \begin{cases} \tilde{Re}_{\theta t} - 396.035 \cdot 10^{-2} + (-120.656 \cdot 10^{-4})\tilde{Re}_{\theta t} + (868.23 \cdot 10^{-6})\tilde{Re}_{\theta t}^2 \\ +(-696.596 \cdot 10^{-9})\tilde{Re}_{\theta t}^3 . (174.105 \cdot 10^{-12})\tilde{Re}_{\theta t}^4 & \tilde{Re}_{\theta t} \leq 1870 \\ \tilde{Re}_{\theta t} - (593.11 + (\tilde{Re}_{\theta t} - 1870) \cdot 0.482) & \tilde{Re}_{\theta t} > 1870 \end{cases} \tag{2-18}$$

and $\tilde{Re}_{\theta t}$ from the transport Eq. (2-22). This correlation is determined based on a series of numerical experiments on a flat plate where the critical Reynolds number was varied along with the freestream turbulence intensity and the subsequent transition Reynolds number was measured based on the most upstream location where the skin friction started to increase. The destruction or relaminarization source is defined as

$$E_\gamma = c_{a2}\rho\Omega\gamma F_{turb}(c_{es}\gamma - 1), \tag{2-19}$$

where Ω is the vorticity magnitude. This term acts like a sink term and ensures that the intermittency remains close to zero in the laminar boundary layer. It also enables the model to predict relaminarisation because it provides a means for the intermittency to return to zero once the transition criteria in the F_{onset} function is no longer satisfied. F_{turb} is used to disable the destruction/relaminarization source outside of a laminar boundary layer and is defined as follows:

$$F_{turb} = e^{-\left(\frac{R_T}{4}\right)^4}. \tag{2-20}$$

The boundary condition for γ at a wall is zero normal flux while at an inlet the value of γ is equal to 1. In order to capture the laminar and transitional boundary layers correctly, the grid must have a y^+ of approximately 1 [8].

The experimental transition correlations relate the Reynolds number of transition onset, $Re_{\theta t}$ to the turbulence intensity, Tu, and other quantities in the freestream where

$$Re_{\theta t} = f(Tu, ..)_{freestream}. \tag{2-21}$$

This is a non-local operation since the value of $Re_{\theta t}$ is required by the intermittency equation inside the boundary layer, and not only in the freestream. On the other hand, the turbulence intensity can change strongly inside the domain and one global value over the entire flowfield is not acceptable. In order to use only local quantities, a different way for passing information from the freestream to the boundary layer is required. The solution to this problem is provided by a second transport equation which treats the transition momentum thickness Reynolds number $Re_{\theta t}$ as a transported scalar quantity. An empirical correlation is used to calculate $Re_{\theta t}$ in the freestream and then its value is merged by the transport equation into the boundary layer. This transport equation essentially takes a non-local empirical correlation (i.e. Eq. (2-32)) and transforms it into a local quantity, which then can be used to compute the transition length F_{lenght} and the critical Reynolds number $Re_{\theta c}$ at every location of the flow field.

The transport equation for the transition onset momentum thickness Reynolds number is given by

$$\frac{\partial(\rho\tilde{Re}_{\theta t})}{\partial t} - \frac{\partial(\rho U_j\tilde{Re}_{\theta t})}{\partial x_j} = P_{\theta t} + \frac{\partial}{\partial x_j}\left[\sigma_{\theta t}(\mu + \mu_t)\frac{\partial\tilde{Re}_{\theta t}}{\partial x_j}\right]. \tag{2-22}$$

Outside the boundary layer, the source term $P_{\theta t}$ is designed to force the transported scalar $\tilde{Re}_{\theta t}$ to match the local value of $Re_{\theta t}$ calculated from an empirical correlation. The production term can be computed from the relations below:

$$P_{\theta t} = c_{\theta t}\frac{\rho}{t}(Re_{\theta t} - \tilde{Re}_{\theta t})(1 - F_{\theta t}), \tag{2-23}$$

$$t = \frac{500\mu}{\rho U^2} \tag{2-24}$$

$$F_{\theta t} = \min\left(\max\left(F_{wake}e^{-\left(\frac{y}{\delta}\right)^4}, 1 - \left(\frac{\gamma - 1/c_{e2}}{1 - 1/C_{e2}}\right)^2\right), 1\right), \tag{2-25}$$

$$\theta_{BL} = \frac{\tilde{Re}_{\theta t}\mu}{\rho U}\ ;\ \delta_{BL} = \frac{15}{2}\theta_{BL}\ ;\ \delta = \frac{50\Omega y}{U}\delta_{BL}, \tag{2-26}$$

$$Re_\omega = \frac{\rho\omega y^2}{\mu}\ ;\ F_{wake} = e^{\left(\frac{Re_\omega}{1\times10^5}\right)^2}, \tag{2-27}$$

were t is a time scale defined for dimensional reasons. The blending function $F_{\theta t}$ is used to turn off the source term in the boundary layer and allow the transported scalar $\tilde{Re}_{\theta t}$ to diffuse in from the freestream. $F_{\theta t}$ is equal to zero in the freestream and 1 in the boundary layer.

The following constants are used in the model:

$$c_{a1} = 1,\ c_{a2} = 0.03,\ c_{e2} = 50,\ \sigma_f = 1,\ c_{\theta t} = 0.03,\ \sigma_{\theta t} = 2. \tag{2-28}$$

During the development of the $\gamma - Re_{\theta t}$ model it was observed that whenever a laminar boundary layer separation occurred, the model predicted the turbulent reattachment location too far downstream. By comparison with experimental results it was found that the accuracy of the model tended to decrease as the freestream turbulence was lowered. The reason for this is that the turbulent kinetic energy k in the separating shear layer is smaller at lower freestream turbulence levels. As a consequence, it takes longer for k to become large enough to make the boundary layer to reattach. In order to solve this problem, the following modification to handle separation induced transition was implemented:

$$\gamma_{sep} = \min\left(s_1 \max\left[0, \left(\frac{Re_v}{3.235Re_{\theta c}}\right) - 1\right]F_{reattach}, 2\right)F_{\theta t}, \tag{2-29}$$

where,

$$F_{reattach} = e^{-\left(\frac{R_T}{20}\right)^4},\ s_1 = 2, \tag{2-30}$$

$$\gamma_{eff} = \max(\gamma, \gamma_{sep}). \tag{2-31}$$

This modification allows k to grow rapidly once the laminar boundary layer separates and has a negligible effect for attached transition. The main idea behind this correction is to allow the local intermittency to exceed 1 whenever the laminar boundary layer separates. This will result in a large production of k, which in turn will cause earlier reattachment. The size of the separation bubble is controlled with the constant s_1. The $F_{reattach}$ term disables the modification once the viscosity ratio is large enough to cause reattachment and $F_{\theta t}$ is the blending function that confines the modification to boundary layer type flows.

The boundary condition for $\tilde{Re}_{\theta t}$ at a wall is zero flux. The boundary condition for $\tilde{Re}_{\theta t}$ at and inlet should be calculated from an empirical correlation based on the inlet turbulence

intensity. The empirical correlation is defined as follows:

$$Re_{\theta t} = \left[1173.51 - 589.428Tu + \frac{0.2196}{Tu^2}\right] F(\lambda_\theta),\ Tu \leq 1.3, \tag{2-32}$$

$$Re_{\theta t} = 331.5[Tu - 0.5658]^{-0.671} F(\lambda_\theta),\ Tu > 1.3, \tag{2-33}$$

$$F(\lambda_\theta) = 1 - [-12.986\lambda_\theta - 123.66\lambda_\theta^2 - 405.689\lambda_\theta^3]e^{-\left(\frac{Tu}{1.5}\right)^{1.5}},\ \lambda \leq 0, \tag{2-34}$$

$$F(\lambda_\theta) = 1 + 0.275[1 - e^{[-35\lambda_\theta]}]e^{-\left(\frac{Tu}{0.5}\right)},\ \lambda > 0, \tag{2-35}$$

where,

$$\lambda_\theta = \frac{\rho\theta^2}{\mu}\frac{dU}{ds}, \tag{2-36}$$

$$Tu = 100\frac{\sqrt{2k/3}}{U}. \tag{2-37}$$

The derivative dU/ds corresponds to the acceleration along the streamwise direction and can be computed by taking the derivative of the velocity U in the x, y and z directions and the summing the contribution of these derivatives along the streamwise direction. The following constraints are introduced for numerical robustness:

$$-0.1 \leq \lambda_\theta \leq 0.1,\quad Tu \geq 0.027,\quad Re_{\theta t} \geq 20. \tag{2-38}$$

The transition model is coupled to the $k-\omega$ SST model through the use of the effective intermittency from Eq. (2-31) by modifying the production and dissipation terms in the k equation as follows:

$$\tilde{P}_k = \gamma_{eff} P_k,\quad \tilde{D}_k = \min(\max(\gamma_{eff}, 0.1), 1) D_k, \tag{2-39}$$

where P_k and D_k are the production and destruction terms in the turbulent kinetic energy of the original SST equation respectively. The final modification to the SST model is a change in the blending function F_1 which is responsible for the switching between the $k-\omega$ and $k-\epsilon$ models. The reason is that the original blending function could potentially switch from 1 to 0 in the center of the boundary layer, which is undesirable since the $k-\omega$ model should be active in the laminar and transitional boundary layers. The modified blending function is defined by

$$F_1 = \max(f_{1,orig}, F_3),\quad F_3 = e^{-\left(\frac{R_y}{120}\right)^8},\quad R_y = \frac{\rho y\sqrt{k}}{\mu}, \tag{2-40}$$

where $F_{1,orig}$ is the original blending function of the SST model.
In the following sections the physical effects of curvature are discussed and the curvature correction term proposed by Spalart and Shur [12] will be described in detail.

2-5 Curvature Effects on Turbulent Flow

The purpose of this section is to provide the physical explanation of curvature effects in turbulent flows. Surface curvature can suppress or amplify turbulence depending on whether it is convex or concave curvature. The turbulence in a boundary layer entering a convex curve is diminished by centrifugal acceleration, while the turbulence entering a concave curve is amplified. The shear is toward the center of curvature in the destabilizing case and outward

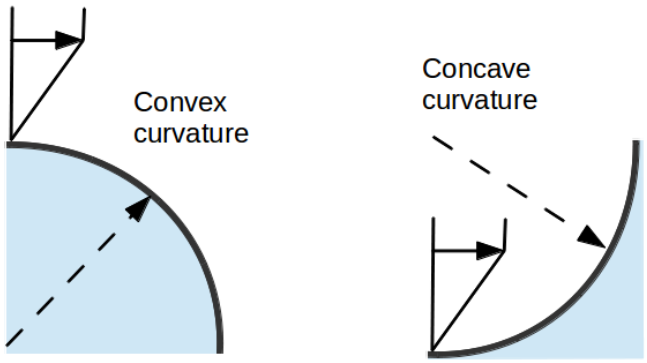

Figure 2-3: Schematic of boundary layers on curved surfaces. Convex curvature is stabilizing and concave is destabilizing. (Adapted from Dubrin and Reif [2].)

from it in the stabilizing. A schematic representation of this effect is shown in Fig. 2-3. The origin of curvature effects can be understood by an examination of the Reynolds stress transport equation, particularly the production term. The transport equation for the Reynolds stress tensor $\overline{u_i u_j}$ is given by

$$\begin{aligned}\frac{\partial \overline{u_i u_j}}{\partial t} + U_k \frac{\partial \overline{u_i u_j}}{\partial x_k} &= -\frac{1}{\rho}\left(\overline{u_j \frac{\partial p}{\partial x_i}} - \overline{u_i \frac{\partial p}{\partial x_j}}\right) - 2\nu \overline{\frac{\partial u_i}{\partial x_k}\frac{\partial u_j}{\partial x_k}} \\ &\quad - \frac{\partial \overline{u_k u_i u_j}}{\partial x_k} - \overline{u_j u_k}\frac{\partial U_i}{\partial x_k} - \overline{u_i u_k}\frac{\partial U_j}{\partial x_k} + \nu \nabla^2 \overline{u_i u_j},\end{aligned} \tag{2-41}$$

where $-\overline{u_j u_k}(\partial U_i/\partial x_k) - \overline{u_i u_k}(\partial U_j/\partial x_k)$ corresponds to the production term [2].
If we consider cylindrical coordinates, $x_1 = R\theta$ and $x_2 = r$, the shear flow in Fig. 2-3 is in x_1 direction $U = U(r)e_1$, where $e_1 = (-\sin\theta, \cos\theta)$ is the unit vector in the circumferential direction. The vector on the radial direction is $e_2 = (\cos\theta, \sin\theta)$. Then the velocity gradient has the following non-zero components:

$$\begin{aligned} e_1 \frac{\partial}{x_1} U(r) e_1 &= e_1 U(r) \frac{\partial e_1}{\partial x_1} = -e_1 e_1 \frac{U(r)}{R}, \\ e_2 \frac{\partial}{x_2} U(r) e_1 &= e_2 e_1 \frac{\partial U(r)}{\partial r}, \end{aligned} \tag{2-42}$$

and

$$\frac{\partial U_j}{\partial x_i} = \begin{Bmatrix} 0 & -\frac{U(r)}{R} & 0 \\ \frac{\partial U(r)}{\partial r} & 0 & 0 \\ 0 & 0 & 0 \end{Bmatrix} \tag{2-43}$$

By considering the previous velocity gradient, the non-zero components of the production term in the Reynolds stress transport equation (Eq. (2-41)) become

$$\begin{aligned} P_{11} &= -2\overline{u_1 u_2}\frac{\partial U_1}{\partial x_2} = -2\overline{uv}\frac{\partial U}{\partial r}, \\ P_{22} &= -2\overline{u_2 u_1}\frac{\partial U_2}{\partial x_1} = 2\overline{uv}\frac{U}{R}, \\ P_{12} &= -\overline{u_2 u_2}\frac{\partial U_1}{\partial x_2} - \overline{u_1 u_1}\frac{\partial U_2}{\partial x_1} = -\overline{v^2}\frac{\partial U}{\partial r} + \overline{u^2}\frac{U}{R}, \end{aligned} \tag{2-44}$$

and the turbulent kinetik energy production corresponds to

$$P = \frac{1}{2}(P_{11} + P_{22}) = -\overline{uv}\left(\frac{\partial U}{\partial r} - \frac{U}{R}\right). \tag{2-45}$$

On a convex wall the velocity increases in the radial direction; hence $\partial_r U > 0$. The two terms of P are opposite in sign and the curvature acts to diminish the production of turbulent kinetic energy by the mean shear. On the other hand, for the case of a concave wall $\partial_r U < 0$. The two terms of the right hand side of Eqs. (2-44) that contribute to P_{12} and P have the same sign. In this case curvature supplements the production by mean shear. From the previous analysis it becomes clear that concave curvature is destabilizing and amplifies the turbulence. In the following section, a correction term proposed by Spalart and Shur [12] in order to account for the effects of curvature in turbulence models will be presented.

2-6 Curvature Correction

It was previously shown that curvature affects the production terms of the Reynolds stress transport equation. The explicit appearance of these effects in the turbulent equations is cited as a fundamental advantage of the full Reynolds stress turbulence models, which intend to solve Eq. (2-41). However, these models are stiff and difficult to converge compared to the simple eddy viscosity models for complex engineering applications. For this reason, a more robust approach to account for curvature effects is to properly modify the simpler eddy viscosity models. The measure proposed by Spalart and Shur in [12] is based on intuitive arguments developed in thin shear layers, it is Galilean-invariant and fully defined in three dimensions which makes is possible to implement in any RANS solver.

Consider a thin shear flow with a velocity profile $U(y) = y$ and assume that $U_y > 0$ so that the spanwise vorticity $\Omega_z < 0$. For this type of flow it holds that $\overline{u^2} > \overline{v^2}$ which is equivalent to stating that the principal axes of the strain tensor are not aligned with those of the strain tensor, but rotated counterclockwise [12]. The curvature correction term proposed by Spalart and Shur relies on a central hypothesis, which states that under weak rotation or curvature turbulence is enhanced if the Reynolds stress principal axes are leading the strain axes or vice versa. In this context they propose to track the direction of the principal axes of the strain tensor. In a weakly curved thin shear flow, the flow direction, the direction of the strain principal axes, and that of the Reynolds stress axes all evolve at the same rate U/R. The strain axes are invariant and therefore usable in a simple turbulence model which leads to the quantity

$$e \equiv \frac{D\alpha}{Dt}, \tag{2-46}$$

where the angle α gives the direction of the strain tensor principal axes with respect to an inertial reference frame. The strain axes are invariant and the Lagrangian derivative of a quantity which is defined with respect to an inertial frame, $D\alpha/Dt$ is also Galilean invariant.

The direction of the strain tensor axes α is susceptible to system rotation. In a homogeneous rotating flow with system rotation rate Ω^{rot} and time independent deformation, $D\alpha/Dt = \Omega^{rot}$. If an inhomogeneous incompressible flow is considered, the Lagrangian derivative of α can be calculated for a two dimensional case by differentiating analytically the strain tensor eigensystem, which results in

$$\frac{D\alpha}{Dt} = \Omega^{rot} + \frac{1}{2(S_{11}^2 + S_{12}^2)} \left[S_{11} \frac{DS_{12}}{Dt} - S_{12} \frac{DS_{11}}{Dt} \right]. \tag{2-47}$$

The strain rate tensor S_{ij} and the Lagrangian derivative on the right hand side of Eq. (2-47) are defined with respect to the reference frame of the system, which is rotating at a rate Ω^{rot}. The sign of e is only relevant compared with that of the vorticity. The stress-strain misalignment is in the direction of the vorticity and the non dimensional quantity $\tilde{r} = e/\Omega_z$ is then suggested as a prime candidate. Small positive values of $\tilde{r}$ suppress turbulence activity; while small negative values enhance it. For the case of solid body rotation, the measure $\tilde{r}$ reduces to $e = \omega/2$, so that $\tilde{r} = 1/2$. In a pure azimuthal flow $U_\theta(r)$, $e = U_\theta/r$ sign $d[rU_\theta]/dr$. Therefore the streamline curvature is recovered per se, U_θ/r. The extension of Eq. (2-47) to three-dimensional flows is given by Eq. (2-52). The empirical function proposed by Spalart and Shur in Ref. [12] to account for effects of streamline curvature and system rotation is defined by

$$f_{rotation} = (1 + c_{r1}) \frac{2r^\star}{1 + r^\star} [1 - c_{r3} \tan^{-1}(c_{r2}\tilde{r})] - c_{r1}, \tag{2-48}$$

which was initially tested in the Spalart-Allarmas one-equation turbulence model. In order to incorporate the curvature correction to the $k - \omega$ SST turbulence model, equation (2-48) is replaced by Smirnov and Menter in Ref. [11] by f_{r1}, which is defined as

$$f_{r1} = \max[\min(f_{rotation}, 1.25), 0.0], \tag{2-49}$$

and it is used to control the production terms in the $k - \omega$ SST model equations as follows:

$$\frac{\partial(\rho k)}{\partial t} + \frac{\partial(\rho U_j k)}{\partial x_j} = P_k f_{r1} - \beta^\star \rho k \omega + \frac{\partial}{\partial x_j} \left[\mu_{ref} \frac{\partial k}{\partial x_j} \right]. \tag{2-50}$$

$$\frac{\partial(\rho \omega)}{\partial x_j} + \frac{\partial(\rho U_j \omega)}{\partial x_j} = \alpha \frac{\rho P_k}{\mu_t} f_{r1} - D_\omega + Cd_\omega + \frac{\partial}{\partial x_j} \left[\mu_{ef} \frac{\partial \omega}{\partial x_j} \right]. \tag{2-51}$$

The difference between Eqs. (2-48) and (2-49) is that the latter limits the function values from 0 which corresponds to a strong convex curvature (stabilized flow, no turbulence production) to 1.25 corresponding to strong concave curvature (enhanced turbulence production). The lower limit is proposed for numerical stability reasons whereas the upper limit is used to avoid overgeneration of eddy viscosity in flows with destabilizing curvature or rotation. The arguments in Eq. 2-48 are defined as follows:

$$\tilde{r} = 2\Omega_{ik} S_{jk} \left[\frac{DS_{ij}}{Dt} + (\varepsilon_{imn} S_{jn} + \varepsilon_{jmn} S_{in}) \Omega_m^{rot} \right] \frac{1}{\Omega D^3}, \tag{2-52}$$

$$r^\star = \frac{S}{\Omega}, \tag{2-53}$$

where Ω_m^{rot} are the components of the system rotation vector in three dimensions and ε_{ijk} is the tensor of Levi-Civita. The different terms in Eqs. (2-52) and (2-53) are given by

$$S_{ij} = \tfrac{1}{2}\left(\tfrac{\partial U_i}{\partial x_j} + \tfrac{\partial U_j}{\partial x_i}\right), \tag{2-54}$$

$$\Omega_{ij} = \tfrac{1}{2}\left(\left(\tfrac{\partial U_i}{\partial x_j} - \tfrac{\partial U_j}{\partial x_i}\right) + 2\varepsilon_{mji}\Omega_m^{rot}\right), \tag{2-55}$$

$$S^2 = 2S_{ij}S_{ij}, \tag{2-56}$$

$$\Omega^2 = 2\Omega_{ij}\Omega_{ij}, \tag{2-57}$$

$$D^2 = \max(S^2, 0.09\omega^2), \tag{2-58}$$

and DS_{ij}/Dt are the components of the Lagrangian derivative of the strain tensor. Smirnov and Menter [11] suggest a technique to calculate this term for a three-dimensional Navier-Stokes CFD solver based on the control volume method. This technique will be applied in the RANS solver and its implementation is discussed in Chapter 3. In order to apply the control volume method, the material derivative DS_{ij}/Dt is expressed using the integral (Eulerian) flow formulation, which states that the total derivative of each component of the strain tensor in an arbitrary volume τ can be written as

$$\int_\tau \frac{DS_{ij}}{Dt}\, d\tau = \frac{D}{Dt}\int_\tau S_{ij}\, d\tau = \frac{\partial}{\partial t}\int_\tau S_{ij}\, d\tau + \int_\sigma S_{ij}U_n\, d\sigma, \tag{2-59}$$

where the first term on the right hand side corresponds to the local derivative and the second term is the convective derivative. Here σ is the surface of the volume τ, $U_n = \vec{U}\cdot\hat{n}$, $\vec{U}$ and $\hat{n}$ are the velocity and normal vectors at the integration point.

For steady state flows the first term in the right hand side of Eq. (2-59) is zero in converged solutions so there is no need to compute it during iterations. Then

$$\frac{D}{Dt}\int_\tau S_{ij}\, d\tau = \int_\sigma S_{ij}U_n\, d\sigma. \tag{2-60}$$

The application of the control volume approach to discretize the right hand side of Eq. (2-60) results in

$$\int_\sigma S_{ij}U_n\, d\sigma \;\rightarrow\; \sum_{k=1}^{N} S_{ij}^{(k)}U_n^{(k)}\sigma^{(k)}, \tag{2-61}$$

where the summing is done over the N surfaces of the control volume. The superscript (k) refers to the centres of the faces, σ^k is the area of the k-th face while $S_{ij}^{(k)}$ and $U_n^{(k)}$ are computed at the face centres. The final discrete formula for DS_{ij}/Dt is computed from Eq. (2-61) by dividing through the cell volume

$$\frac{DS_{ij}}{Dt} = \left[\sum_{k=1}^{N} S_{ij}^{(k)}U_n^{(k)}\sigma^{(k)}\right]\frac{1}{\tau}, \tag{2-62}$$

where τ is the volume of the computational cell. Finally, the constants c_{r1}, c_{r2} and c_{r3} in Eq. (2-48) are 1.0, 2.0 and 1.0 respectively. In the next chapter the data structure of the RANS solver will be presented and the implementation of the curvature correction term in the code will be discussed.

Chapter 3

Numerical Method

The purpose of this chapter is to document the implementation of the Spalart and Shur [12] curvature correction term in the in-house Reynolds-Averaged Navier-Stokes (RANS) solver developed at Stanford University by Pecnik et al [18]. In section 3-1 a brief descriprion of the solver's data structures is provided. Based on this data structure, section 3-2 describes the algorithm to calculate the curvature correction factor.

3-1 Data Structure of the RANS Solver

The RANS solver is entirely written in C++ language and it solves the compressible Navier-Stokes equations on unstructured meshes with a discretization based on the finite volume formulation and implicit time integration scheme on arbitrary polihedral mesh elements [4]. The data structure of the solver employs the centers of the control volumes, the faces and the nodes of the mesh (as shown in Fig. 3-1) to manipulate information. The cell centers store the

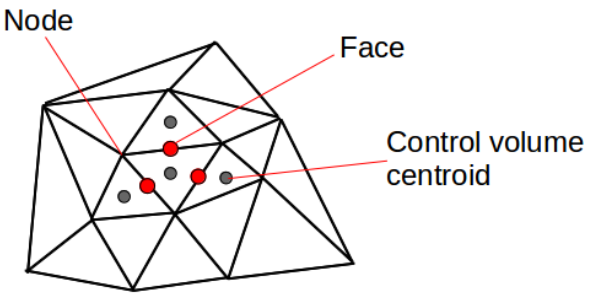

Figure 3-1: The data structure of the RANS solver requires the centers of the control volumes, the faces and the nodes to store information.

physical information of the flow (P, ρ, $\vec{V}$... etc.) and every face inside the mesh is associated

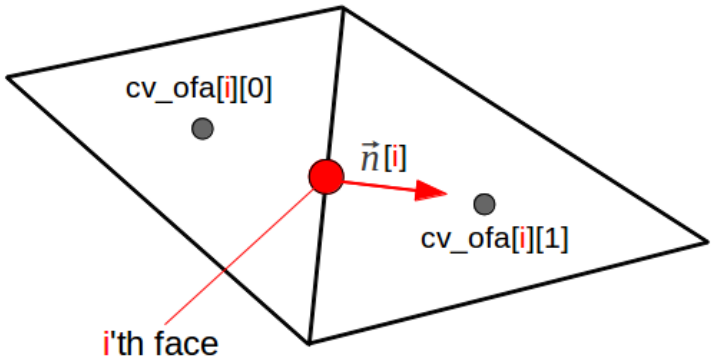

Figure 3-2: Every face in the mesh is associated with the two neighboring control volume centers, which are denoted as cv_ofa[i][0] and cv_ofa[i][1], where i is the index of the face and the second index denotes the left and right control volume of the face. In addition, every face is associated with a vector normal to it's surface which points in the opposite direction of node cv_ofa[i][0] and has the magnitude of the face area.

with two neighboring control volumes. These control volumes are denoted by cv_ofa[i][0] and cv_ofa[i][1] where i is the index of the face. In addition, every face is associated with a vector normal to its surface which points in the same direction as the vector connecting cv_ofa[i][0] to cv_ofa[i][1] and has the magnitude of the face area. This is schematically illustrated in Fig. 3-2. The following section describes the algorithm to calculate the curvature correction factor based on the data structure previously described.

3-2 Curvature Correction Algorithm

The algorithm presented in this section calculates the curvature correction factor in every cell center of the mesh at every time step. The correction factor f_{r1} is given by Eq. 2-49, where the $f_{rotation}$ term is calculated from Eq. 2-48, which reads

$$f_{rotation} = (1 + c_{r1})\frac{2r^\star}{1 + r^\star}[1 - c_{r3}\tan^{-1}(c_{r2}\tilde{r})] - c_{r1}.$$

The arguments in Eq. 2-48 are defined as follows:

$$\tilde{r} = 2\Omega_{ik}S_{jk}\left[\frac{DS_{ij}}{Dt} + (\epsilon_{imn}S_{jn} + \epsilon_{jmn}S_{in})\Omega_m^{rot}\right]\frac{1}{\Omega D^3},$$
$$r^\star = \frac{S}{\Omega}.$$

The physical properties in the previous equations such as S and Ω are defined in every cell center. However, the total derivative of the strain tensor DS_{ij}/Dt is not defined. For this reason, before evaluating Eq. 2-48, it is necesary to compute DS_{ij}/Dt over each cell center of the grid. This can be achieved by making use of the descrete formula (Eq. 2-62) provided

by Smirnov and Menter [11]:

$$\frac{DS_{ij}}{Dt} = \left[\sum_{k=1}^{N} S_{ij}^{(k)} V_n^{(k)} \sigma^{(k)}\right] \frac{1}{\sigma},$$

where the summing is done over the N faces of the control volume. The superscript (k) refers to the centres of the face, σ^k is the area of the k-th face while $S_{ij}^{(k)}$ and $V_n^{(k)}$ are computed at the face centres. The τ factor corresponds to the volume of the computational cell.

In order to evaluate Eq. (2-62) at every cell center of the mesh a first subroutine is created. This subroutine performs a cycle over the faces of the complete computational mesh and adds the contribution of each face to its neighboring control volume centers. The algorithm is repeated for every time step of the solver and can be summarized as follows:

1 For every face k in the mesh calculate the distances d_0 and d_1 from face center to the neighboring control volumes cv_ofa[i][0] and cv_ofa[i][1].

2 Using the velocity gradient of each cell center calculate the velocity at the i-th face:

$$\vec{V}_{0,face} = \vec{V}_0 + \nabla\vec{V}_0 \cdot \vec{dx}_{0,face},$$
$$\vec{V}_{1,face} = \vec{V}_1 + \nabla\vec{V}_1 \cdot \vec{dx}_{1,face},$$

where $\vec{V}_0$ and $\vec{V}_1$ are the velocity vectors, and $\nabla\vec{V}_0$ and $\nabla\vec{V}_1$ are the velocity gradients at the nodes [0] and [1] respectively. The vectors $\vec{dx}_{0,face}$ and $\vec{dx}_{1,face}$ represent the relative position between the cell centers and the k-th face.

3 Calculate the average velocity at the k-th face using

$$\vec{V}_k = \frac{\vec{V}_{1,face} * d_0 + \vec{V}_{0,face} * d_1}{d_0 + d_1}.$$

4 Using the same type of averaging calculate the strain tensor value S_{ij} over the i-th face.

5 Calculate the $V_n^{(k)}\sigma^{(k)}$ factor from Eq. 2-62: In order to achieve this, the dot product between the normal vector (recall that the magnitude of the normal vector equals the area of the face $\sigma^{(k)}$) and the average velocity vector in the k-th face is performed:

$$V_n^{(k)}\sigma^{(k)} = \vec{n} \cdot \vec{V}_k.$$

6 Calculate the contribution of the k-th face to the $\frac{DS_{ij}}{Dt}$ value of each one of the neighboring control volume centers:

$$\frac{DS_{ij}}{Dt}[0] = \frac{DS_{ij}}{Dt}[0] + (S_{ij}^{(k)} V_n^{(k)} \cdot VA) * \frac{1}{\tau_0},$$
$$\frac{DS_{ij}}{Dt}[0] = \frac{DS_{ij}}{Dt}[1] - (S_{ij}^{(k)} V_n^{(k)} \cdot VA) * \frac{1}{\tau_1}.$$

The contribution is added or substracted by considering the correct sign for the summation of the fluxes based on the Green-Gauss theorem. The normal vector is always pointing from index [0] to [1] of the control volumes. Then, at the boundary the normal vector is always pointing outside the domain.

Once the total derivative of the strain tensor DS_{ij}/Dt has been computed on every cell center of the mesh, a second subroutine is used to evaluate Eqs. (2-48) and (2-49) in order to provide the correction factor at every cell center. Once evaluated, the correction factor interacts with the $k-\omega$ SST turbulence model through the production terms of the k and ω equations as described in section 2-6. The C++ subroutines that calculate DS_{ij}/Dt and f_{r1} are included in Appendix A. In the following chapter the curvature correction term is implemented in a series of test cases and a detailed discussion of the results is provided.

Chapter 4

Results

In the present chapter the implementation of the algebraic curvature correction term is validated for four different 2D test cases and a discussion of the results is provided. The first two cases correspond to a flow over an adiabatic flat plate [22] and the fully turbulent flow inside a U-duct channel [11, 23]. These tests are performed to ensure the correct implementation of the curvature correction term in the RANS solver. Then, in order to assess the improvement in the predictive capability of the solver, the correction term is tested on two well documented turbomachinery test cases. The first one being the prediction of the heat transfer coefficient over a Von Karman Institute (VKI) transonic turbine guide vane [3], and the second the prediction of the pressure coefficient over a high lift T106 low pressure turbine blade [21].

In order to test the performance of the curvature correction term, four different model configurations are used along this chapter. The $k-\omega$ SST turbulence model of Menter [19] is used in its original form or combined with the $\gamma - Re_{\theta T}$ transition model of Langtry and Menter [8], the modified curvature correction term of Smirnov and Menter [11] or both. The different configurations are shown in Tab. 4-1, where the first column indicates the abbreviations which are used hereafter.

Table 4-1: Four different numerical schemes used to assess the performance of the curvature correction term. Each scheme is a combination of the $k-\omega$ SST turbulence model with the $\gamma - Re_{\theta T}$ transition model, the curvature correction term or both.

Abbreviation	**Turbulence model (SST)**	**Transition model (ReT)**	**Curvature correction (CC)**
SST	✓	-	-
SST-CC	✓	-	✓
SST-ReT	✓	✓	-
SST-ReT-CC	✓	✓	✓

4-1 Flat Plate

The purpose of the present test case is to compare the predictions of the turbulence model combined with the transition model with and without curvature correction (SST-ReT and SST-ReT-CC models) for a subsonic flow over a flat plate. Since a flat surface has no curvature, the Spalart and Shur correction term must not affect the solution and the results of both calculations should be identical. The flow conditions correspond to the test case T3A, with zero pressure gradient boundary layer documented by Savill [22]. The boundary conditions of the problem are presented in Appendix B.

The computational domain was provided by Dr. Rene Pecnik and it consists of 5120 control volumes divided by an H-type grid which provides a resolution of $y^+ < 0.3$ at the walls. Figure 4-1 shows the skin friction coefficient c_f over the plate as a function of the Reynolds number Re_x, which is calculated based on the distance between the leading edge of the plate and a generic location x over its surface. The skin friction coefficient is defined by

$$c_f = \frac{\tau_w}{\frac{1}{2}\rho_\infty U_\infty^2}, \tag{4-1}$$

where $\tau_w = \mu(\partial U/\partial y)$ is the local wall shear stress, ρ_∞ and U_∞ are the freestream density and velocity, respectively. From Fig. 4-1 it is possible to distinguish the transition process by the sudden increase of the skin friction coefficient from the laminar flow region at $Re_x = 15000$ to the turbulent one $Re_x = 27000$. In addition, the comparison between the curvature corrected solution (SST-ReT-CC) with the non-corrected one (SST-ReT) shows that the curvature correction has no effect on the flow over a flat plate.

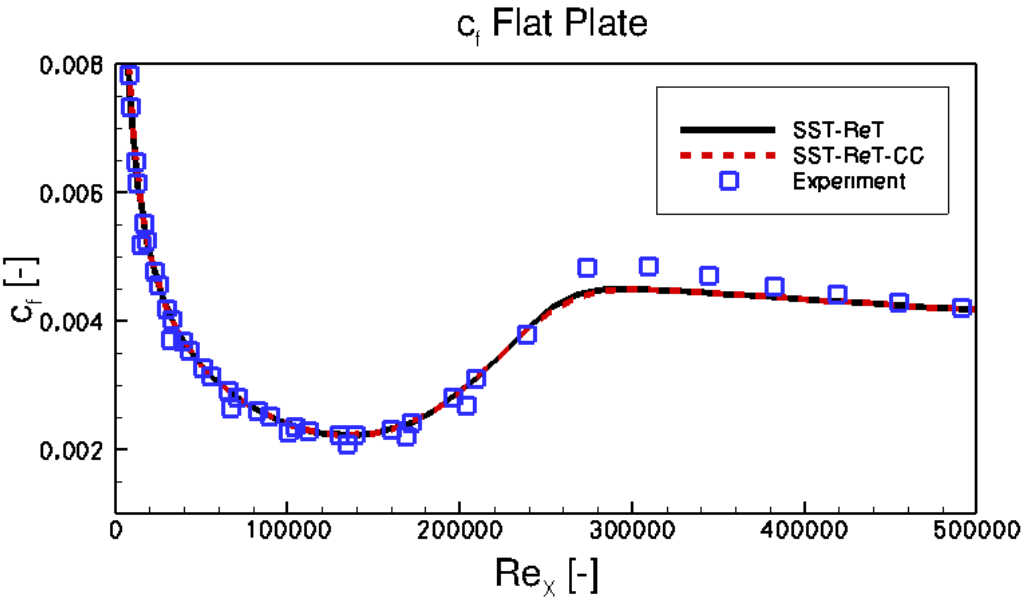

Figure 4-1: Skin friction coefficient as a function of the Reynolds number Re_x over an adiabatic flat plate. The Reynolds number Re_x is calculated based on the distance between the leading edge of the plate and the particular point x over the surface of the plate.

4-2 Two-Dimensional Flow in a U-Duct Channel

In the present section the results of a two-dimensional flow in a U-duct channel are presented. The objective of this test is to compare the results of the numerical method against experimental data provided by Monson and Seegmiller [23] and the simulations carried out by Smirnov and Menter [11] in order to ensure the correct implementation of the curvature correction term.

The fluid motion through a U-duct channel is a well known case which is characterized by a strong streamline curvature and it contains flow separation and reattachment on the inner (convex) wall of the duct. In addition, the flow upstream the U-bend is turbulent and fully developed. These features represent a challenge for the different RANS solvers and a thorough test for turbulence models.

The mesh of the computational domain is shown in Fig. 4-2 and it consists of 26307 elements clustered at the walls to ensure y^+ values of nearly 0.1. The computational grid of the U-duct test case was generated in the course of this work by a mesh generating program developed in-house at the TU Delft by Ir. Enrico Rinaldi. The Reynolds number of the flow, based on the channel width H and the mean flow velocity U_m is set equal to $Re = 10^6$ as specified in Refs. [23] and [11]. Additionally, the reference Mach number is set to $M = 0.1$ at the inlet in order to avoid compressibility effects. In order to guarantee a fully developed turbulent flow and the specified value of Reynolds number Re at the inlet of the computational domain, the boundary conditions of the problem are set as follows. In accordance with Ref. [11], fully developed profiles of velocity, density and turbulence properties are calculated for a straight channel in a pre-processing step and then specified as the inlet boundary condition for the U-tube. At the outlet of the domain a constant value of static pressure is fixed. The sides of the channel are considered symmetrical and a no slip condition is specified on the walls. For sake of completeness, the specific values of the boundary conditions used for the U-duct and the straight channel computations are included in Appendix B. In order to provide a comparison with the numerical results of Smirnov and Menter [11], the fully turbulent numerical solutions (SST and SST-CC) are used.

Figures 4-3 and 4-4 show the skin friction coefficient defined by Eq. (4-1) over the inner and outer walls of the U-duct channel. The skin friction coefficient is calculated over the walls by considering the position coordinate along the central line of the U-duct. From Fig. 4-3 it is possible to observe that the flow accelerates when entering the curve ($s = 0$) which translates in an increase of c_f, and separation occurs on the inner wall near the position $s = 2.5$ which is reflected by the negative sign of c_f. Later on, at $s = 5$ flow reattaches and the skin friction coefficient becomes positive. On the other hand, no separation is observed on the outer wall of the channel since c_f remains positive all the time. Figures 4-7 (d)-(f) show the turbulent kinetic energy in the normal direction of the wall at different positions of the channel. At the angles of 0 and 90 degrees of the U-turn (Figs. 4-7 (d)-(e)), it can be clearly seen that the curvature correction term reduces the turbulence levels over the inner wall, which translates in lower values of the skin friction coefficient of the SST-CC model compared to the non-corrected SST. Additionally, the curvature correction enhances the turbulence levels over the concave region of the outer wall, resulting in higher values of the skin friction coefficient of the SST-CC model.
Figures 4-5 and 4-6 show the pressure coefficient over the inner and outer walls of the U-duct.

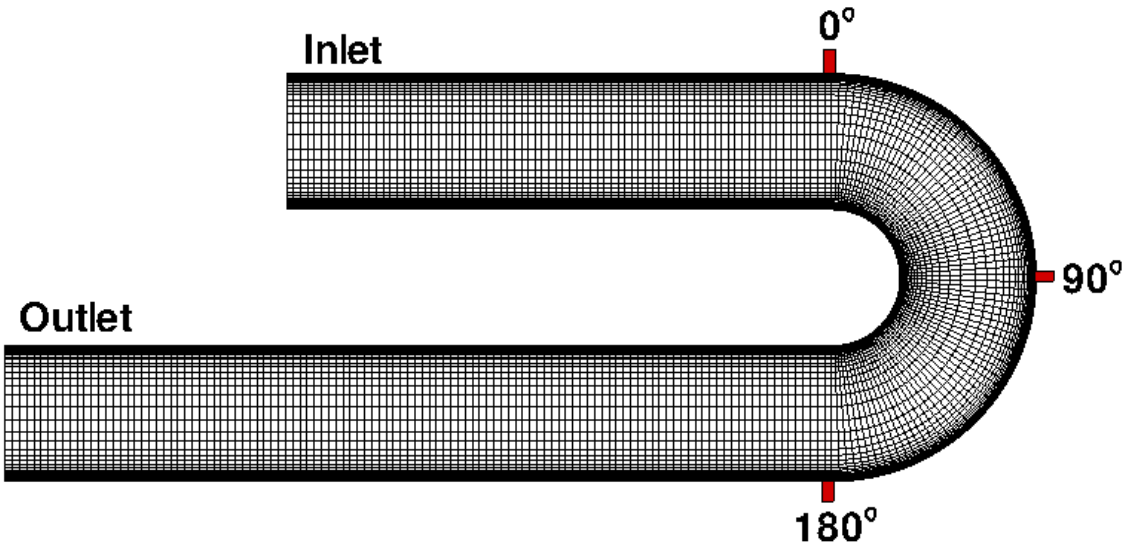

Figure 4-2: Computational domain and grid used for the U-duct channel. The width of the channel is 3.81 cm and the inner radius of the U-bend is 1.91 cm as specified by Monson and Seegmiller [23].

The pressure coefficient is defined as

$$c_p = \frac{P - P_\infty}{\frac{1}{2}\rho_\infty U_\infty^2}, \tag{4-2}$$

where p is the static pressure over the surface, p_∞ is the reference pressure, ρ_∞ and U_∞ are the freestream density and average velocity specified at the inlet of the channel. Figures 4-7 (a)-(c) show the velocity profiles at different sections of the U-duct. From figures (a) and (b) there is no visible effect of the curvature correction on the velocity profile. However, from figure (c) (angle of 180^o) it is possible to observe that the non-corrected SST model predicts early flow reattachment as the velocity value near to the inner wall is close to zero. The curvature correction reduces the turbulence levels over the inner (concave) surface of the wall, which delays the reattachment point (see also Fig. 4-3) and translates in a higher velocity value near the wall.

The calculations performed in this section are in good agreement with the experimental results and show a positive effect of the curvature correction on the SST turbulence model. Moreover, the results correspond to the numerical calculations of Smirnov and Menter [11]. From these results, in combination to the ones obtained in the previous section, it is possible to conclude that the curvature correction is correctly implemented in the RANS solver.

4-3 Von-Karman Institute (VKI) Transonic Turbine Guide Vane

In the present section the curvature correction is tested for the flow computation around a VKI transonic turbine guide vane. The VKI profile was experimentally investigated by Arts et al. in Ref. [3]. The experiments were performed in a compression tube facility in order

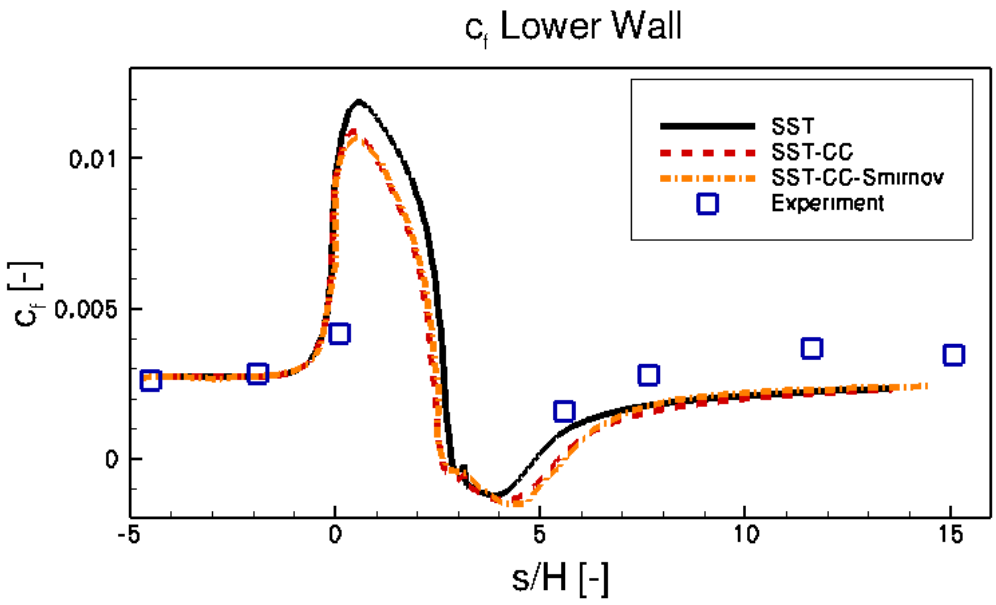

Figure 4-3: Skin friction coefficient c_f along the inner wall of the U-duct. The x axis represents the distance along the central line of the U-duct normalized with respect to the width H.

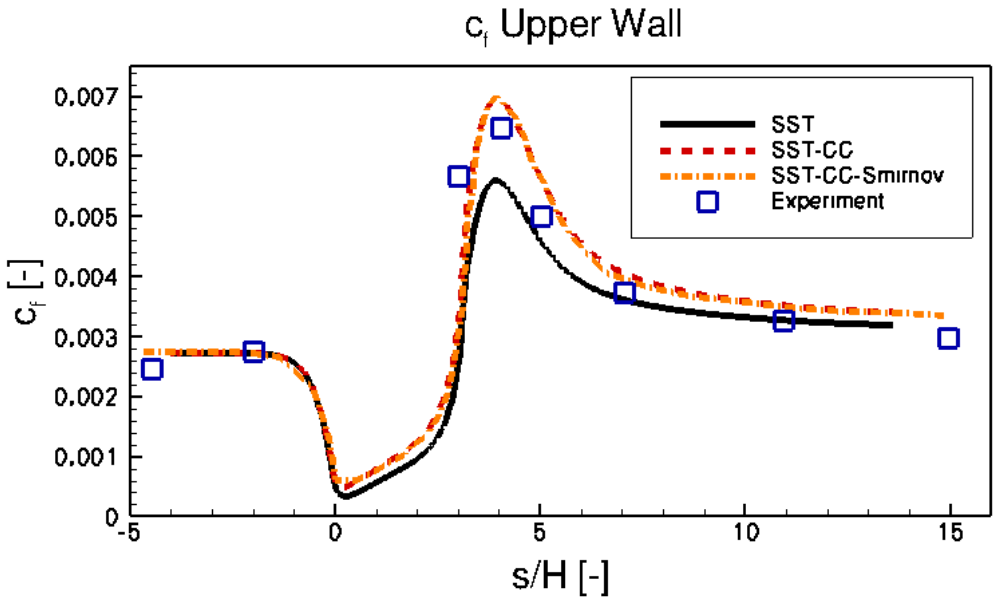

Figure 4-4: Skin friction coefficient c_f along the upper wall of the U-duct. The x axis represents the distance along the central line of the U-duct normalized with respect to the width H.

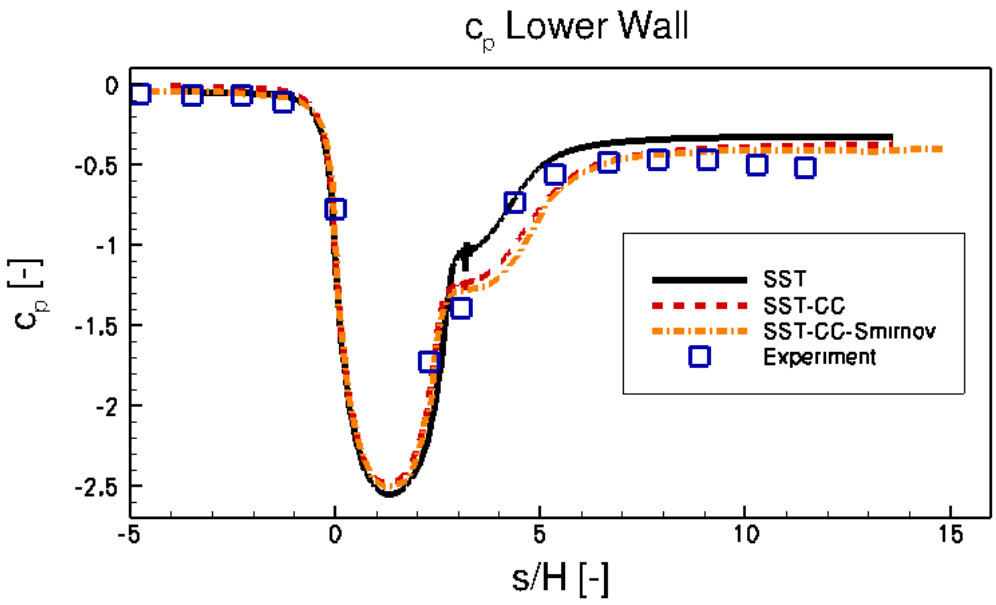

Figure 4-5: Pressure coefficient c_p along the inner wall of the U-duct. The x axis represents the distance along the central line of the U-duct normalized with respect to the width H.

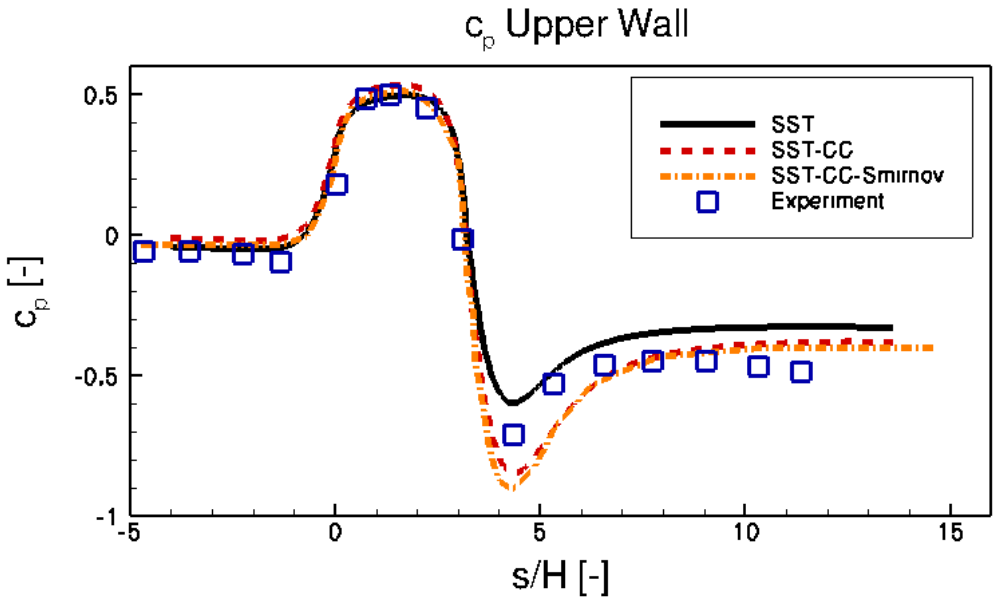

Figure 4-6: Pressure coefficient c_p along the upper wall of the U-duct. The x axis represents the distance along the central line of the U-duct normalized with respect to the width H.

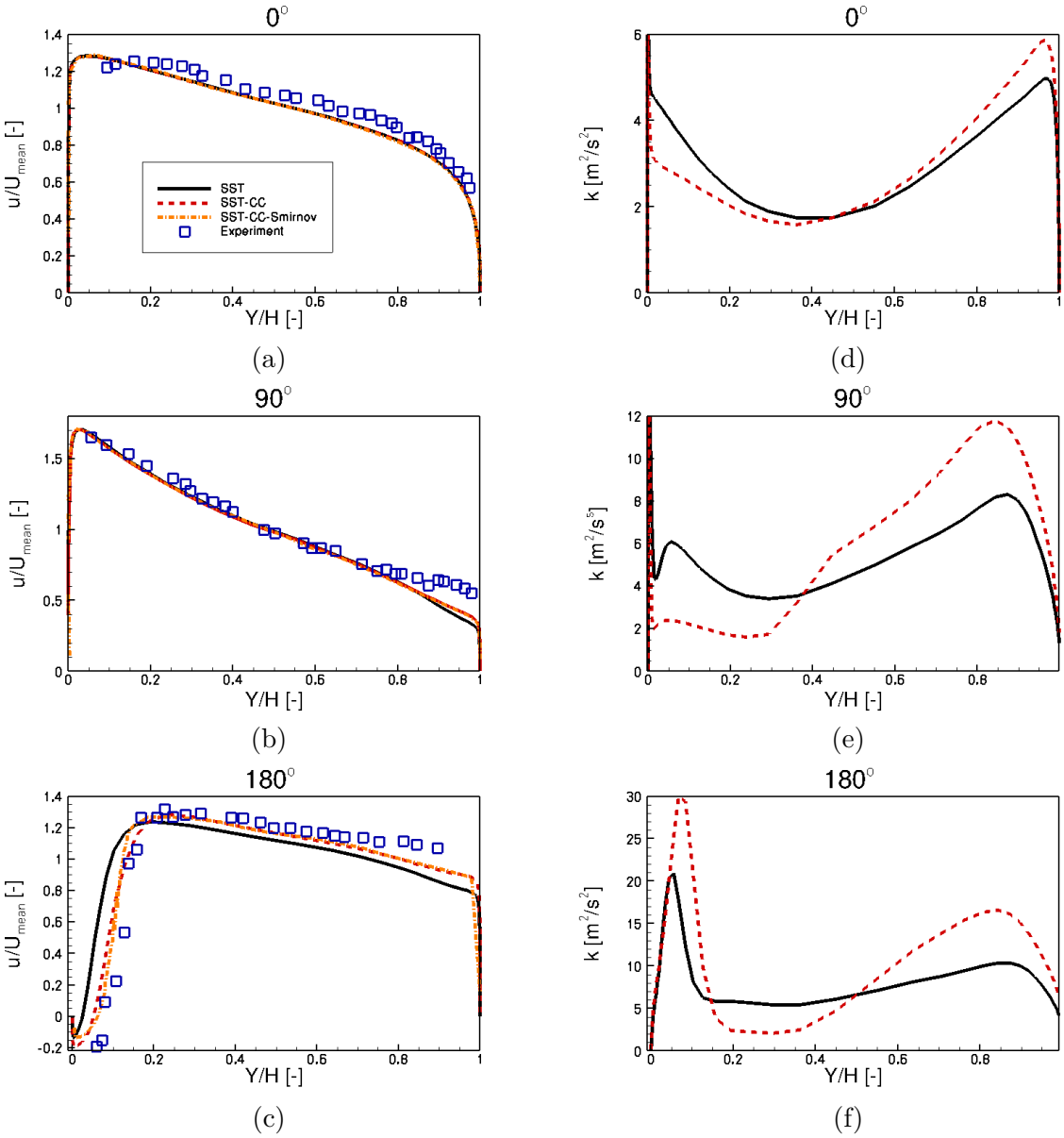

Figure 4-7: Turbulent kinetic energy (right side) and streamwise velocity (left side) profiles at different locations of the U-duct. The velocities are normalized with respect to the mean velocity at the inlet of the channel. The x-axis shows the position coordinate perpendicular to the wall normalized by the channel width.

Table 4-2: Geometrical characteristics of the VKI turbine guide vane.

Parameter	Value	
Chord	67.647	[mm]
Pitch to chord	0.85	[-]
Stagger angle	55^o	[-]
Throat to chord	0.2207	[-]

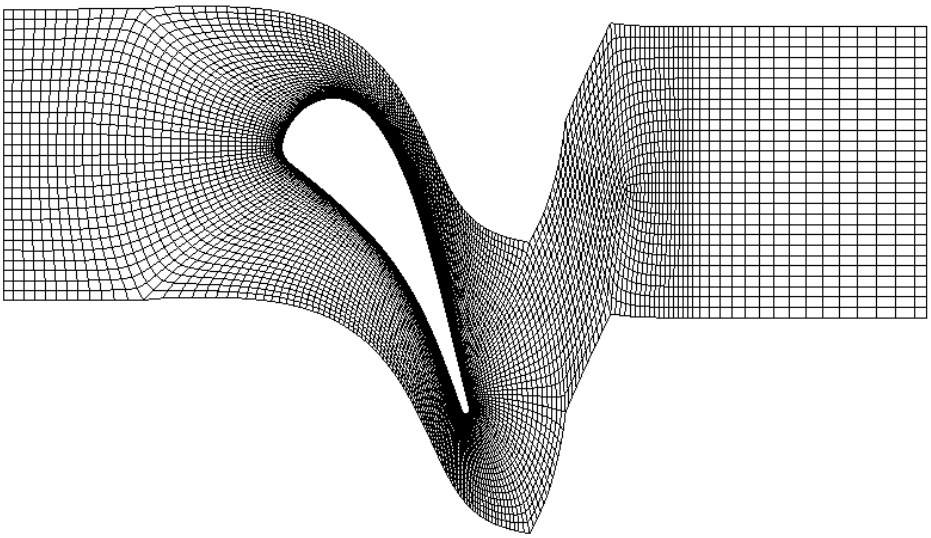

Figure 4-8: Computational domain of the VKI transonic guide vane. The grid consists of 25000 control volumes providing a resolution of $y^+ < 1$ at the first cell-row at the blade surface.

to study the influence of Mach number, turbulence intensity, and Reynolds number on the transitional heat transfer distribution. The most important blade characteristics are given in Tab. 4-2. The computational domain used for the present calculations (Fig. 4-8) was provided by Dr. Rene Pecnik and it consists of 25000 control volumes with a grid resolution of $y^+ < 1$ at the first cell-row at the blade surface. The reference temperature T_∞ is prescribed to be 416 K, while the temperature of the blade T_w is kept constant at 300 K. The heat transfer coefficient h is calculated based on the predicted heat flux q_w and the difference between the total and the wall temperatures:

$$h = \frac{q_w}{T_\infty - T_w}.$$

The numerical calculations are performed for the two different flow conditions (cases MUR235 and MUR241), which are summarized in Tab. 4-3. For each test case, the four different numerical schemes shown in Tab. 4-1 are used in order to assess the influence of the transition model and the curvature correction on the solution. The specific values of the boundary conditions used for the the MUR235 and MUR241 test cases can be found in Appendix B.

Figures 4-9 and 4-10 show the heat transfer coefficient as a function of the curvilinear coordinate along the blade s/c normalized by the chord for the MUR235 and the MUR241 test cases. Positive values of s/c indicate the suction side, while negative values of s/c correspond to the pressure side of the blade. From the experimental data it is possible to observe laminar to turbulent transition on the suction side due to a sharp increase in the heat

Table 4-3: Data of the VKI turbine guide vane test cases, where $M_{is,out}$ and $Re_{c,out}$ are the isentropic Mach number and the Reynolds number based on the chord length, both calculated at the outlet region. Re_M is the Reynolds number based on the velocity and mesh spacing of the turbulence grid in the experimental setup, used to calculate the specific dissipation rate ω [4].

	$Tu\%$	$M_{is,out}$	$Re_{c,out}$	Re_M
MUR235	6.0	0.927	1.15×10^6	61700
MUR241	6.0	1.089	2.11×10^6	61700

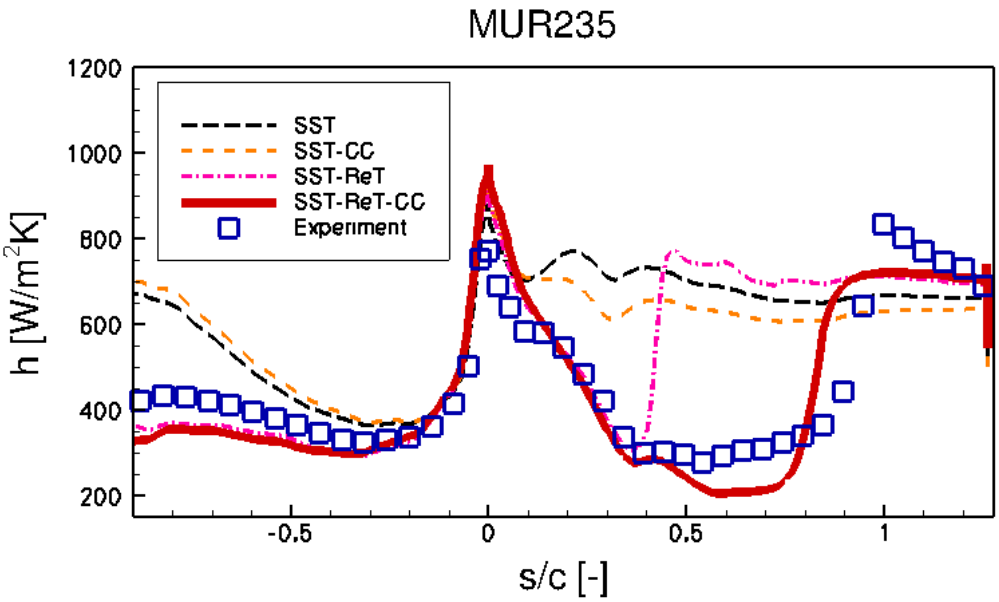

Figure 4-9: Heat transfer coefficient over the VKI blade profile for the MUR235 test case. The different lines represent numerical calculations while the squares represent the experimental results of Arts et al. [3]. Positive values of s/c indicate the suction side, while negative values of s/c correspond to the pressure side of the blade.

transfer coefficient; at $s/c = 0.8$ for the MUR235 and at $s/c = 0.6$ for the MUR241 case. On the other hand, none of the test cases exhibits transition on the pressure side as the variations of the heat transfer coefficients are smooth. From the numerical calculations it is possible to observe that the SST and the SST-CC schemes in general overestimate the heat transfer coefficient along the surface. Both solutions present smooth oscillations in the heat transfer coefficient over the suction side, for this reason no transition point can be distinguished. This is an expected result as the SST model was developed for a fully turbulent boundary layer and does not take transition into account. On the other hand, by comparing these two models some trends in the qualitative behaviour of the curvature corrected solution can be provided. In both test cases, the MUR235 and MUR241 it is possible to observe that the curvature correction term mitigates the turbulence levels on the suction side (concave surface) which translates in a lower heat transfer coefficient of the SST-CC model compared to the fully turbulent SST. Furthermore, the turbulence levels are enhanced by the curvature correction over the pressure side (concave surface), which translates in a higher heat transfer coefficient.

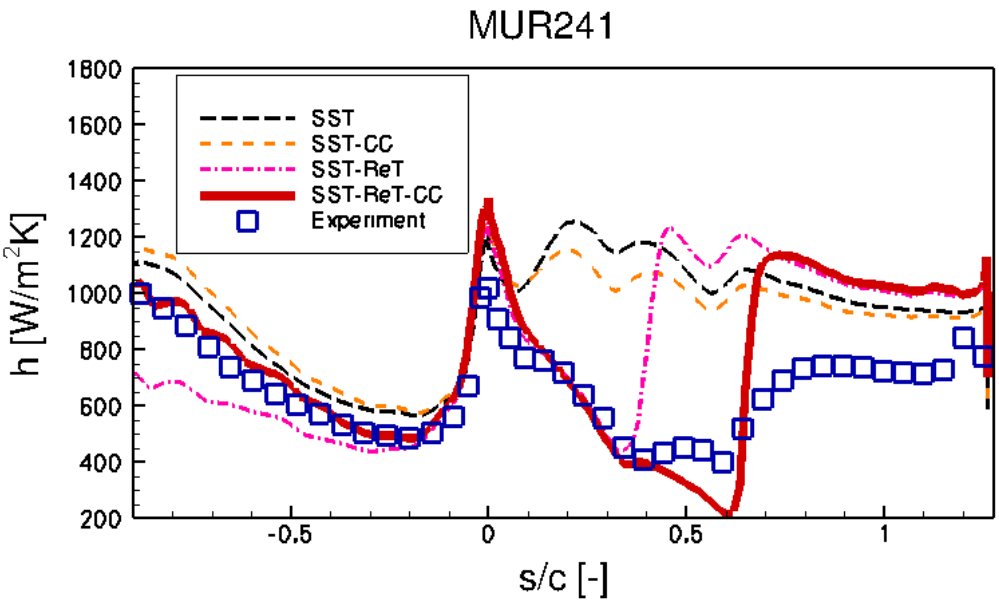

Figure 4-10: Heat transfer coefficient over the VKI blade profile for the MUR241 test case. The different lines represent numerical calculations while the squares represent the experimental results of Arts et al. [3]. Positive values of s/c indicate the suction side, while negative values of s/c correspond to the pressure side of the blade.

From the results of the SST-ReT calculations it is possible to distinguish laminar to turbulent transition over the suction side for both, MUR235 and MUR241 test cases. Nevertheless, despite the ability of the $\gamma - Re_{\theta t}$ model to predict transition there is a large deviation between the calculated transition point and the experimental data. It is necessary to notice that the transition model is based on empirical correlations derived from incompressible flat plate experiments that control the onset and extent of the transition. The critical Reynolds number $Re_{\theta c}$ determines where the intermittency first starts to grow and F_{lenght} controls the extent of transition. Therefore, these deviations from the experimental data can be expected as the complexity of the flow geometry increases.

On the other hand, the results from the turbulence model with transition and curvature correction (SST-ReT-CC) show for both test cases a delay in the transition point which improves the agreement with the experimental data. This effect is the consequence of the curvature correction factor, which decreases the turbulence levels in the boundary layer over a concave surface (suction side). The reduction of the turbulence levels in the boundary layer cause the transition model to trigger the onset further downstream. This can be seen from Fig. 4-12, which shows the turbulent kinetic energy and velocity distributions in the normal direction of the blade for the MUR241 test case at different positions over the surface. These locations are schematically indicated in Fig. 4-11.

Figures 4-12 (a)-(c) show that the turbulent kinetic energy predicted by the curvature corrected model SST-ReT-CC is lower over the suction side than the one predicted by the non-corrected model SST-ReT. In particular, at the position $s/c = 0.6$ the non corrected model predicts a fully turbulent boundary layer which is reflected by the high values of k.

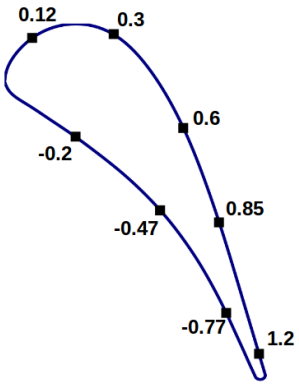

Figure 4-11: Schematic representation of the VKI profile and the different points where the turbulent kinetic energy is calculated.

At positions $s/c = 0.85$ and $s/c = 1.2$ the flow predicted by both models is fully turbulent, however, the turbulent kinetic energy predicted by the corrected solution decays more rapidly. For the pressure side (Figs. 4-12 (f)-(h)), the turbulent kinetic energy predicted by the corrected solution is higher than then the non-corrected one. The pressure side of the profile is a concave surface which translates in a higher value of the correction factor which enhances turbulent kinetic energy production. The same situation occurs for the MUR235 case resulting in similar graphs which are not included here. Figure 4-13 shows the skin friction coefficient c_f for both test cases calculated with the SST-ReT-CC method. As before, it is possible to distinguish the transition point over the suction side of the airfoil which corresponds to a sharp increase in c_f. In addition, the skin friction coefficient always stays positive which indicates that no flow separation occurs over the surface.

4-4 T106 Low-Pressure Turbine Blade

In the present section the curvature correction term is applied to a 2D steady state flow computation around a high-lift low-pressure turbine blade, named T106 in the literature. This test case is of high interest as of today there is a trend to increase the lift coefficients of low pressure (LP) turbine blades in order to reduce engine weight and cost. The Reynolds numbers of LP turbine blades range from about 0.5×10^5 in the final stage at high altitude in small business jet applications to about 5×10^5 at sea level takeoff in the first stage of the largest turbofans [21]. Given these Reynolds numbers and the lift coefficients of modern LP turbines, boundary layer transition and separation play an important role in determining engine performance at different operating conditions.

The T106 profile was experimentally investigated by Opoka et al. in Ref. [21]. The geometrical characteristics of the T106A case are summarized in Tab. 4-4. The inlet conditions correspond to a total temperature T_{in} of 606.5 K and a total pressure P_{in} of 1 bar. The numerical calculations were performed for the two different flow conditions which are summarized in Tab. 4-5. According to Opoka et al. [21], the turbulence intensity values in the second column of Tab. 4-5 are measured in the absence of the blade, at a location corresponding to the leading edge of the profile. In order to guarantee these turbulence levels in the T106

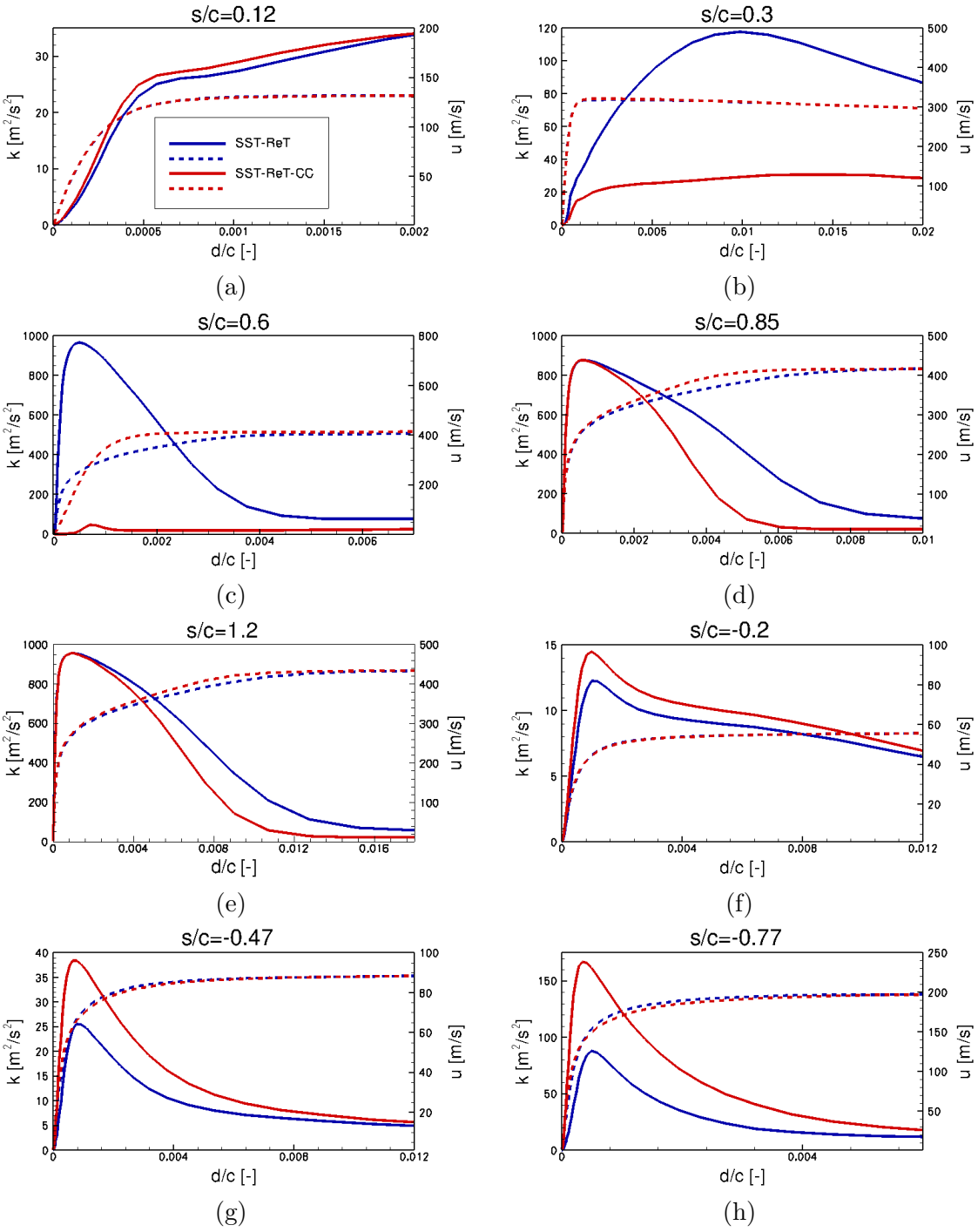

Figure 4-12: Turbulent kinetic energy (solid lines) and velocity distributions (dashed lines) in the normal direction of the surface at different positions over the VKI profile. The distance is normalized by the chord length of the profile.

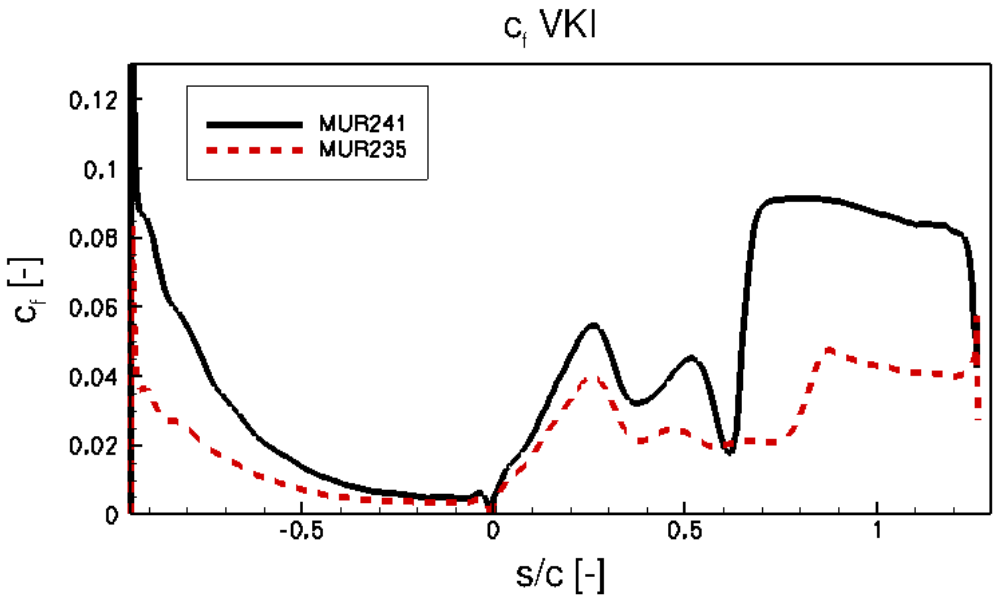

Figure 4-13: Skin friction coefficient over the VKI blade profile for the MUR241 and MUR235 test cases calculated with the SST-ReT-CC method.

Table 4-4: Geometrical characteristics of the T106 low pressure turbine blade.

Parameter	Value	
Chord	99	[mm]
Pitch to chord	0.799	[-]
Stagger angle	59.3^o	[-]
Inlet flow angle	37.7^o	[-]

computational domain, the inlet values of k and ω are first calculated for a straight channel in a pre-processing step. The specific values of the boundary conditions for the T106 test cases are given in Appendix B.

From the previous section it was found that the fully turbulent solution (SST or SST-CC) is not capable of capturing the transition process. For this reason, the present test case is performed only with the numerical models that incorporate the $\gamma - Re_{\theta t}$ transition model (SST-ReT and SST-ReT-CC). The computational domain used for the T106 case (Fig. 4-14) was provided by Dr. Rene Pecnik and it consists of 320 points around the blade surface and 88 points in the normal direction. The maximum value of y^+ at the first cell-row at the blade surface is less than 0.4.

Figures 4-15 and 4-16 show the isentropic pressure coefficient $c_{p,is}$ as a function of the normalized curvilinear coordinate along the blade[1] s/l for the $Tu = 0.5\%$ and the $Tu = 4\%$

[1]This normalization is different to the one used in the VKI test case. The normalization is performed by dividing the position at the suction side and the pressure side by the length of the suction side and the length of the pressure side respectively. This is necessary in order to compare the solutions with the experimental data of Opoka et al. [21]

Table 4-5: Data of the T106A low pressure turbine test cases, where $M_{is,out}$ and $Re_{c,out}$ are the isentropic Mach number and the Reynolds number based on the chord length, both calculated at the outlet region.

	$Tu\%$	$M_{is,out}$	$Re_{c,out}$
Case 1	4.0	0.2986	1.6×10^5
Case 2	0.5	0.2986	1.6×10^5

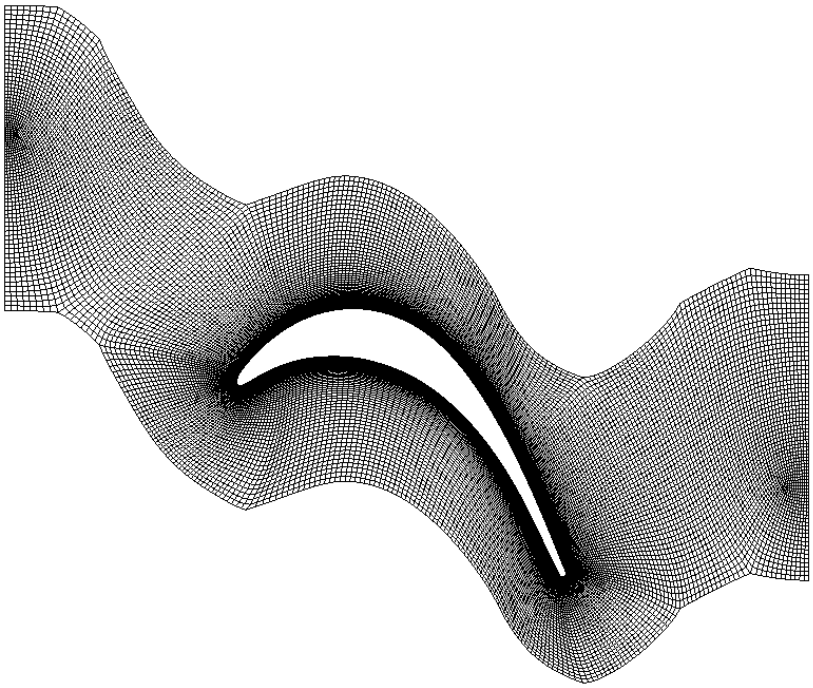

Figure 4-14: Computational domain of the T106 low pressure turbine blade. The computational domain consists of 320 points around the blade surface and 88 points in the normal direction providing a resolution of $y^+ < 0.4$ at the first cell-row over the surface.

test cases. The isentropic pressure coefficient is defined by

$$c_{p,is} = \frac{P_\infty - P}{P_\infty - P_{s2}}, \tag{4-3}$$

where P is the static pressure over the surface, P_∞ is the reference pressure and P_{s2} is the static pressure at the outlet.

From the experimental results it is possible to observe boundary layer separation at $s/l = 0.6$ for the lower turbulence intensity ($Tu = 0.5\%$) case. From this point a pressure *plateau* extends up to a distance $s/l = 0.8$. The end of the pressure plateau indicates the onset of the transition process which manifests through the pressure recovery region. Downstream of $s/l = 0.9$ the boundary layer reattaches. In the higher turbulence intensity ($Tu = 4\%$) case, the distribution of pressure coefficient does not develop a plateau between $s/l = 0.6$ and $s/l = 0.8$, which suggests the absence of a separation bubble.

In general, the numerical results are in good agreement with the experimental data. Moreover, it is possible to observe that the results obtained from the curvature corrected calcula-

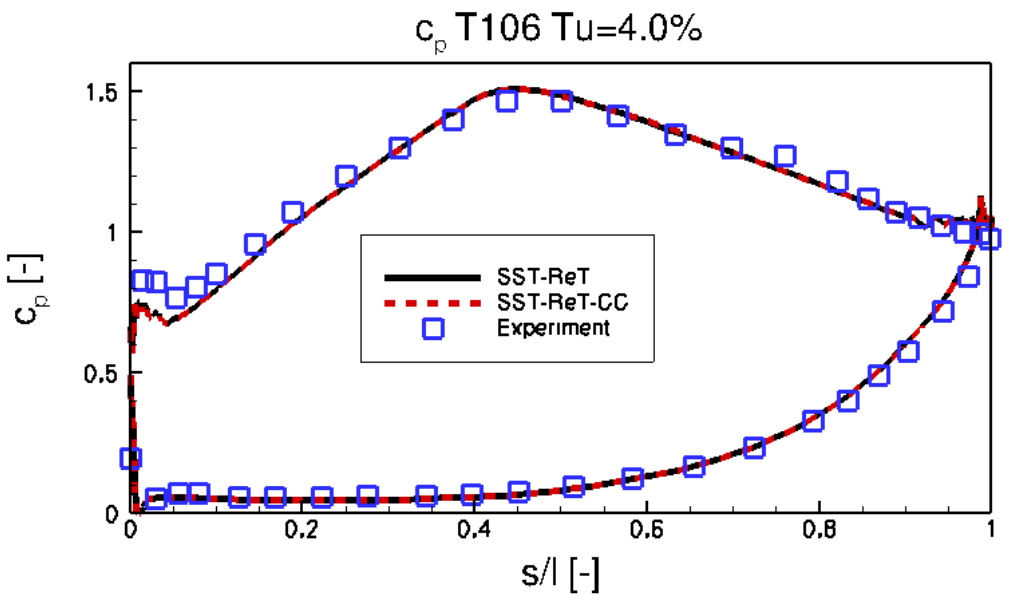

Figure 4-15: Pressure coefficient over the T106 blade profile for the $Tu = 4\%$ test case. The lines represent numerical calculations while the squares represent the experimental results of Opoka et al. The curve on the bottom of the figure corresponds to the pressure side, while the upper one lies on the suction side of the blade.

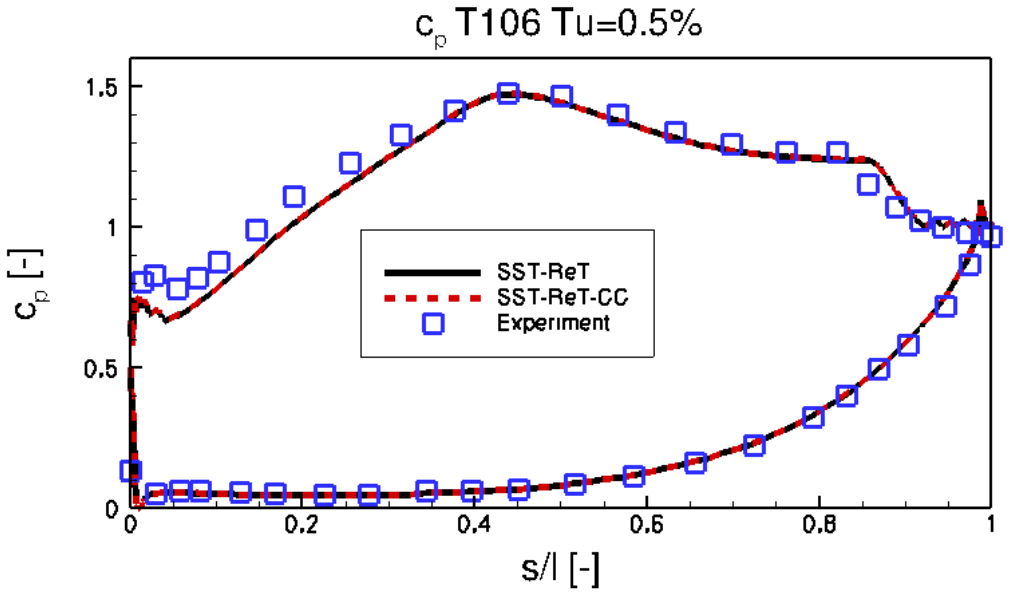

Figure 4-16: Pressure coefficient over the T106 blade profile for the $Tu = 0.5\%$. The lines represent numerical calculations while the squares represent the experimental results of Opoka et al. The curve on the bottom of the figure corresponds to the pressure side, while the upper one lies on the suction side of the blade.

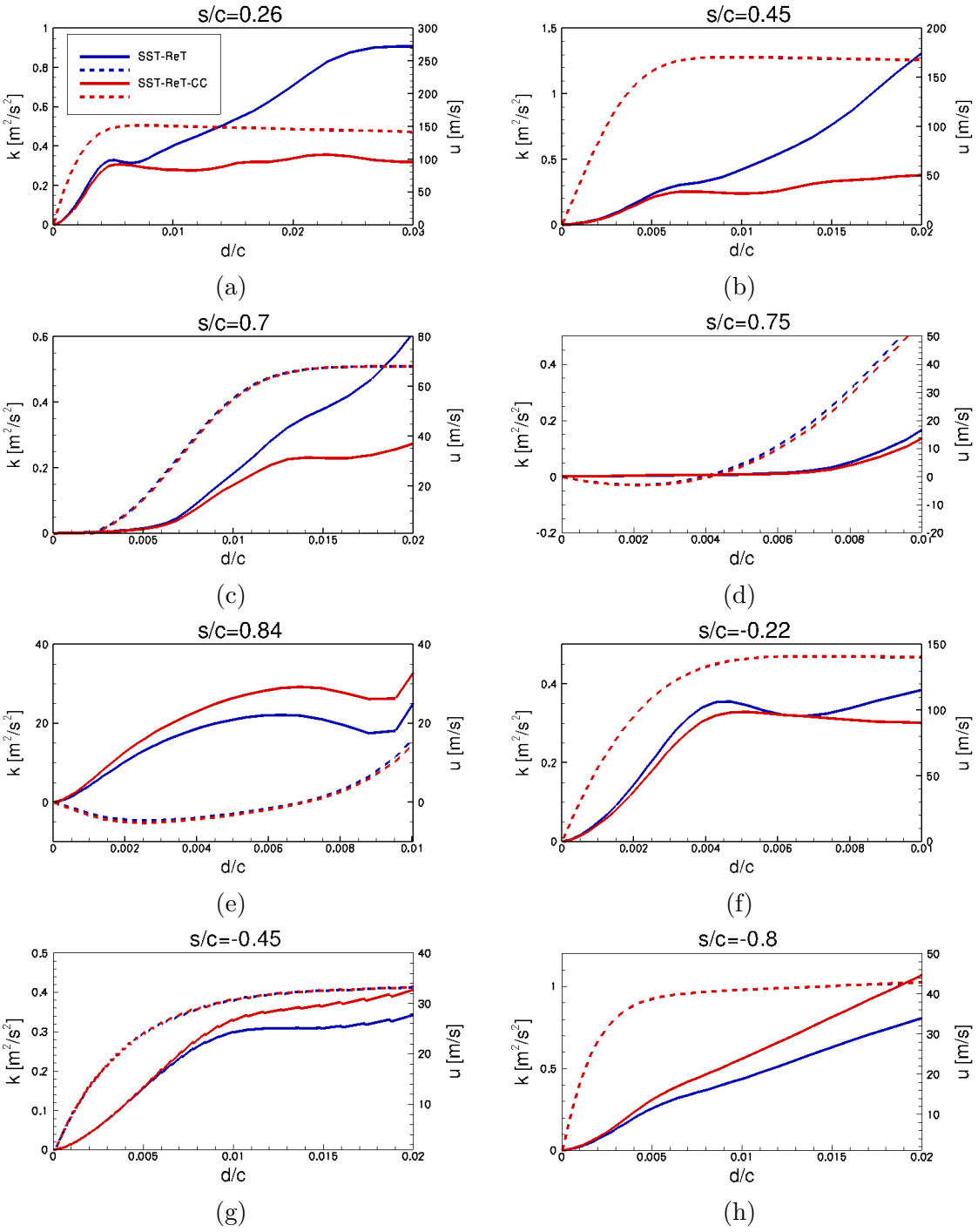

Figure 4-17: Turbulent kinetic energy (solid lines) and velocity distributions (dashed lines) in the normal direction of the surface at different positions over the T106 profile. The distance is normalized by the chord length of the profile.

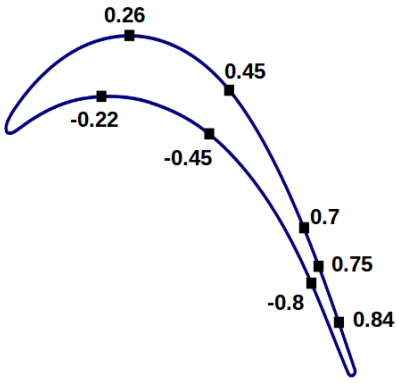

Figure 4-18: Schematic representation of the T106A profile and the different points where the turbulent kinetic energy is calculated.

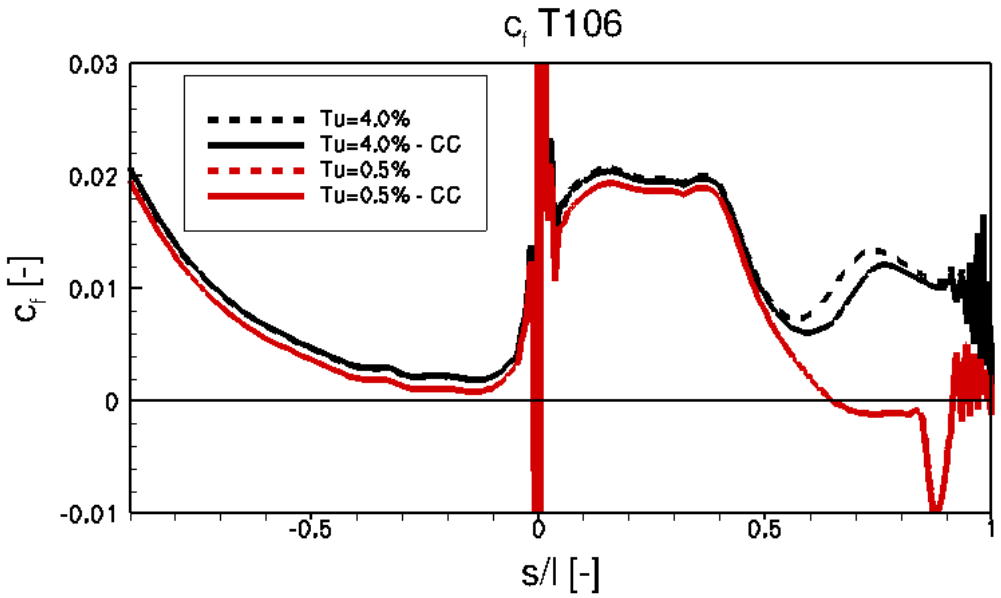

Figure 4-19: Skin friction coefficient over the T106A blade profile for the $Tu = 4.0\%$ and $Tu = 0.5\%$ test cases as a function of the curvilinear coordinate along the blade s/c normalized by the chord. The solid lines represent calculations performed with the SST-ReT-CC model, while the dashed lines are obtained with the SST-ReT scheme. Positive values of s/l indicate the suction side, while negative values of s/l correspond to the pressure side of the blade.

tions (SST-ReT-CC) are the same as from the non-corrected model (SST-ReT). The reason is that, although the boundary layer might separate ($Tu = 0.5\%$), the laminar to turbulent transition occurs in the shear layer above the separation bubble. The increase on turbulent kinetic energy in the boundary layer can be appreciated after the flow reattaches at the very end of the suction side ($s/l = 0.9$). In the case of higher turbulence intensity ($Tu = 4\%$), no transition can be observed over the suction side as the skin friction coefficient changes along the surface are smooth.

Figure 4-17 shows the turbulent kinetic energy and velocity distributions in the normal direction of the surface for the $Tu = 0.5\%$ test case at different positions over the blade, which are schematically indicated in Fig. 4-18. As in the previous VKI test case, it is possible to observe the effect of the curvature correction term within the boundary layer as it increases the turbulent kinetic energy over the pressure side and decreases it over the suction side as compared to the non-corrected solution. Moreover, figures (d)-(e) show the turbulent kinetic energy within the separation bubble. The low values of the turbulent kinetic energy at these positions indicate that no transition occurs across the bubble at this streamwise location.

Figure 4-19 shows the skin friction coefficient for both T106A test cases ($Tu = 4\%$ and $Tu = 0.5\%$) as a function of the curvilinear coordinate s/l. The skin friction coefficient for the low turbulence case becomes negative near the point $s/c = 0.6$ confirming the presence of a separation bubble. For the higher turbulence test case, transition occurs over the suction side of the profile which can be distinguished as a sharp increase of the skin friction coefficient at $s/l = 0.6$. In addition, it can be seen that the curvature corrected solution (CC) shifts the transition onset towards the trailing edge (s/l=1). This effect is the consequence of the curvature correction factor, which decreases the turbulence levels in the boundary layer over a concave surface (suction side). This reduction of the turbulence levels in the boundary layer causes the transition model to trigger the onset further downstream.

Chapter 5

Summary and Conclusions

This thesis presents a thorough analysis of the curvature effects on turbulent flows for turbomachinery applications and documents the steady state simulation of a series of two dimensional test cases characterized by a strong streamline curvature. For this purpose, the Reynolds-Averaged Navier-Stokes (RANS) solver developed by Pecnik et al. [18] is upgraded with two new subroutines which use the local flow field properties, namely the velocity U, the strain tensor S_{ij}, vorticity tensor Ω_{ij} and specific turbulence dissipation rate ω, to calculate the Spalart and Shur [12] curvature correction (CC) term. The correction factor is then implemented in the $k-\omega$ shear stress transport (SST) model of Menter [19] and in the $\gamma - Re_{\theta t}$ (ReT) transition model of Langtry and Menter [8].

The new subroutines are first validated on two well known test cases, namely a subsonic flow over an adiabatic flat plate [22] and the fully turbulent flow inside a U-duct channel [23, 11]. As expected, the results show that the curvature correction term has no effect on the solution of the flat plate test case. For the U-duct channel case, the numerical calculations show that the curvature corrected SST-CC turbulence model agrees better with the experimental data than the original model.
Next, the curvature correction is tested on two well documented turbomachinery test cases. The first one being the prediction of the heat transfer coefficient over a Von Karman Institute (VKI) transonic turbine guide vane [3], and the second the prediction of the pressure coefficient over the high lift T106 low pressure turbine blade [21]. For the VKI test case, two flow configurations (MUR235 and MUR241) are considered, both characterized by the presence of a transition spot over the suction side of the profile. The results show that the SST-CC and the original SST turbulence models overestimate the heat transfer coefficient over the surface of the blade and they are not able to capture the transition process. On the other hand, the results obtained from using the ReT transition model exhibit laminar to turbulent transition over the suction side of the blade and have a better agreement with the experimental data. However, the transition point is still located too far upstream when compared to the experimental values. The results obtained by the curvature corrected ReT model present a significant improvement with respect to the original ReT model as the curvature correction term reduces the turbulence levels over the suction side which cause the transition model to

trigger the onset further downstream.
Finally, the high lift T106 low pressure turbine blade is considered for two different turbulence intensities: $Tu = 4\%$ and $Tu = 0.5\%$. In the case of high freestream turbulence, transition occurs before the boundary layer separates. However, for the lower freestream turbulence case the boundary layer separates and transition occurs in the shear layer above the laminar separation bubble. Here, the transition model is essential for the predictive capability of the simulation and the results are in good agreement with experimental data. For the two different flow configurations no significant improvements are observed when using the curvature correction term.

In this work it has been shown that turbulence in a boundary layer entering a convex curve is diminished by the centrifugal acceleration, while the turbulence of a flow entering a concave surface is amplified. The curvature correction term interacts with the SST turbulence model by modulating the turbulent kinetic energy production. This is particularly beneficial for the ReT transition model performance, which is based on empirical correlations obtained from flat plate experimental data. For a convex surface it has been found that the original SST turbulence model overpredicts the value of the turbulent kinetic energy which leads to an early prediction of the transition point by the ReT model. The effect of the curvature correction term is to reduce the turbulent kinetic energy within the boundary layer delaying the transition point further downstream. On the other hand, the original SST model underpredicts the turbulent kinetic energy over a concave surface. For this reason, although none of the test cases in the present thesis exhibits transition over a concave surface, a delayed transition onset can be expected from the ReT transition model if the curvature correction is not used.

In general, the results obtained in this work show a positive effect of the curvature correction on the flow solutions. Furthermore, the additional computational cost of calculating the correction term is not significant as compared to the operations required by the solver, as the complexity of the algorithm is linear (i.e. the amount of operations is proportional to the number of cells in the computational domain). It is necessary to notice that the curvature correction proposed by Spalart and Shur [12] has been originally developed for weak rotation or curvature. As none of the present test cases exhibit system rotation it becomes necessary to further assess the predictive capability of the correction term by including this effect. In addition, the upper and lower limits of the curvature correction are based on the tests performed by Smirnov and Menter [11]. For this reason, a recalibration of these limits must be considered when applying the curvature correction for turbomachinery test cases .

Appendix A

Subroutines to calculate the Spalart and Shur Correction Term

In the present chapter the subroutines to calculate the Spalart and Shur correction term implemented in the RANS solver are presented. The first subroutine is used to calculate the $\frac{DS_{ij}}{Dt}$ (Equation 2-62) over each cell center of the grid:

```
1
2       virtual void shearstressface()
3       {
4
5         int oo,ii;
6         double d1,d2,VA1,VA2;
7
8          for (int i=0; i<ncv; i++)
9          for (int j=0; j<3; j++)          //Set dsdt to 0 for each time
               step
10         for (int k=0; k<3; k++)
11           {
12          dsdt[i][j][k]=0;
13           }
14
15      //INTERNAL FACES
16      for (int i=nfa_b; i<nfa; i++)           //Recalculate dsdt for the
            new time step
17      {
18
19       oo=cvofa[i][0];
20       ii=cvofa[i][1];
21       d1=sqrt(pow(x_cv[oo][0]-x_fa[i][0],2.0)+pow(x_cv[oo][1]-x_fa[i
             ][1],2.0)+pow(x_cv[oo][2]-x_fa[i][2],2.0));
22       d2=sqrt(pow(x_cv[ii][0]-x_fa[i][0],2.0)+pow(x_cv[ii][1]-x_fa[i
             ][1],2.0)+pow(x_cv[ii][2]-x_fa[i][2],2.0));
23
```

```
24
25      double vel_fa[3];         //VELOCITY AVERAGE
26      double vel_fa0[3];
27      double vel_fa1[3];
28      for (int j=0; j<3; j++){
29      vel_fa0[j]=vel[oo][j]+grad_u[oo][j][0]*(x_fa[i][0]-x_cv[oo][0])+
            grad_u[oo][j][1]*(x_fa[i][1]-x_cv[oo][1])+grad_u[oo][j][2]*(x_fa[
            i][2]-x_cv[oo][2]);
30      vel_fa1[j]=vel[ii][j]+grad_u[ii][j][0]*(x_fa[i][0]-x_cv[ii][0])+
            grad_u[ii][j][1]*(x_fa[i][1]-x_cv[ii][1])+grad_u[ii][j][2]*(x_fa[
            i][2]-x_cv[ii][2]);
31      }
32
33
34
35      for (int j=0; j<3; j++){
36      vel_fa[j]= (vel_fa0[j]*d2+vel_fa1[j]*d1)/(d2+d1);
37      }
38
39      VA1 =  (vel_fa[0]*fa_normal[i][0]+vel_fa[1]*fa_normal[i][1]+vel_fa
            [2]*fa_normal[i][2])/cv_volume[oo];
40      VA2 =  (vel_fa[0]*fa_normal[i][0]+vel_fa[1]*fa_normal[i][1]+vel_fa
            [2]*fa_normal[i][2])/cv_volume[ii];
41
42          for (int j=0; j<3; j++)
43          for (int k=0; k<3; k++)
44            {
45              dsdt[oo][j][k]+= (0.5*(grad_u[oo][j][k]+grad_u[oo][k][j])*d2
                    +0.5*(grad_u[ii][j][k]+grad_u[ii][k][j])*d1)*VA1/(d2+d1);
                      //dsdt_node=dsdt_node-Sij*VA/vol_node
46              dsdt[ii][j][k]-= (0.5*(grad_u[oo][j][k]+grad_u[oo][k][j])*d2
                    +0.5*(grad_u[ii][j][k]+grad_u[ii][k][j])*d1)*VA2/(d2+d1);
47            }
48
49      }
50
51    //BOUNDARY FACES
52     for (int i=0; i<nfa_b; i++)
53      {
54      oo=cvofa[i][0];
55      VA1 =  (vel_bfa[i][0]*fa_normal[i][0]+vel_bfa[i][1]*fa_normal[i][1]+
            vel_bfa[i][2]*fa_normal[i][2])/cv_volume[oo];
56              for (int j=0; j<3; j++)
57              for (int k=0; k<3; k++)
58                   {
59                   dsdt[oo][j][k]=dsdt[oo][j][k] + (0.5*(grad_u[oo][j][k]+
                        grad_u[oo][k][j]))*VA1;
60                   }
61      }
62
63  }
```

Once the total derivative of the strain tensor $\frac{DS_{ij}}{Dt}$ has been computed over every cell center of the mesh, the following subroutine is used to evaluate the curvature correction term f_r (equations 2-48 and 2-49) at every cell center of the grid.

```
1     virtual void CurvatureCorrection(int icv)
2     {
3         double f_rotation,norm_s,norm_om,r_tilde,r_star,D;
4         double c1=1,c2=2,c3=1;
5
6           norm_s  = 0;
7           norm_om = 0;
8
9                for (int j=0; j<3; j++)          //Set dsdt to 0 for each
                     time step
10               for (int k=0; k<3; k++)
11                 {
12                Aux1[icv][j][k]=0;
13                 }
14
15
16          r_tilde = 0;
17
18            for (int f=0;f<3;f++){                    //Here compute S
                  and Omega
19            for (int g=0;g<3;g++){
20              s[icv][f][g]  = 0.5*(grad_u[icv][f][g]+grad_u[icv][g][f]);
21              om[icv][f][g] = 0.5*(grad_u[icv][f][g]-grad_u[icv][g][f]);
22            }  }
23
24            for (int f=0;f<3;f++){                    //Here compute S
                  and Omega norm
25            for (int g=0;g<3;g++){
26              norm_om = norm_om + om[icv][f][g]*om[icv][f][g];
27              norm_s  = norm_s  + s[icv][f][g]*s[icv][f][g];
28            }}
29              norm_om = sqrt(2*norm_om);
30            norm_s  = sqrt(2*norm_s);
31              D       = sqrt(max(norm_s*norm_s,0.09*omega[icv]*omega[icv
                    ]));
32              r_star  = norm_s/norm_om;
33
34            for (int i=0;i<3;i++){                    //Here compute
                  omega_ik*S_jk=omega_ik*S_kj=Aux_ij
35            for (int j=0;j<3;j++){
36              for (int k=0;k<3;k++){
37               Aux1[icv][i][j]=Aux1[icv][i][j]+om[icv][i][k]*s[icv][j][k
                    ];
38            }}}
39
40            for (int f=0;f<3;f++){                    //Here compute
                  Aux1_ij*dsdt_ij=f
41            for (int g=0;g<3;g++){
42              r_tilde  = r_tilde  + 2*Aux1[icv][f][g]*dsdt[icv][f][g];
```

```
43              }  }
44              r_tilde = r_tilde/(norm_om*pow(D,3));
45
46                f_rotation = (1+c1)*(2*r_star/(1+r_star))*(1-c3*atan(c2*
                    r_tilde))-c1;
47                f_r1[icv] = max(min(f_rotation,1.25),0.0);
48
49      }
```

Appendix B

Additional Test Case Data

For the sake of completeness, the particular values of the boundary conditions used for the different test cases of this thesis are presented in this appendix. Tables B-1 to B-3 show the values of the boundary conditions used for the flat plate, the U-duct channel and the straight channel. The turbomachinery test cases, namely the VKI transonic turbine guide vane and the T106 low pressure turbine blade are summarized in table B-4.

Table B-1: Boundary conditions used for the T3A flat plate test case.

Boundary	**Parameter**	**Value**
Reference Values	ρ_∞ [kg/m^3]	1.2
	P_∞ [Pa]	101634
	T_∞ [K]	293.1
	μ_∞ [Pa·s]	6.743e-05
Inlet	P_{in} [Pa]	101634
	T_{in} [K]	293.1
	k_{in} [m^2/s^2]	30
	ω_{in} [1/s]	40000
Outlet	P_{out} [Pa]	0.953e5
Wall	Type	Adiabatic
	U_{wall} [m/s]	0
	k_{wall} [m^2/s^2]	0

Table B-2: Boundary conditions used for the straight channel.

Boundary	Parameter	Value
Reference Values	ρ_∞ [kg/m^3]	15.1
	P_∞ [Pa]	12e5
	T_∞ [K]	277.1
	μ_∞ [Pa·s]	1.841e-5
Inlet/Outlet	ΔP [Pa]	1113
Wall	Type	Adiabatic
	U_{wall} [m/s]	0
	k_{wall} [m^2/s^2]	0

Table B-3: Boundary conditions used for the U-duct channel test case. At the inlet section, fully developed profiles of velocity, density and turbulence properties were calculated for a straight channel in a pre-processing step and then specified as the boundary condition.

Boundary	Parameter	Value
Reference Values	ρ_∞ [kg/m^3]	15.08
	P_∞ [Pa]	12e5
	T_∞ [K]	277.1
	μ_∞ [Pa·s]	1.841e-5
Inlet	U_{in} [m/s]	Straight channel
	ρ_{in} [kg/m^3]	Straight channel
	k_{in} [m^2/s^2]	Straight channel
	ω_{in} [1/s]	Straight channel
Outlet	P_{out} [Pa]	12e5
Wall	Type	Adiabatic
	U_{wall} [m/s]	0
	k_{wall} [m^2/s^2]	0

Table B-4: Boundary conditions used for the turbomachinery test cases, namely the VKI transonic turbine guide vane (MUR235 and MUR241) and the T106 low pressure turbine blade (Tu=0.5% and Tu=4.0%).

Boundary	Parameter	MUR235	MUR241	T106 (Tu=0.5%)	T106 (Tu=4.0%)
Reference Values	ρ_∞ [kg/m^3]	1.54	2.72	0.574	0.574
	P_∞ [Pa]	1.828e5	3.257e5	1e5	1e5
	T_∞ [K]	416.3	416.3	606.5	606.5
	μ_∞ [Pa·s]	1.716e-5	1.716e-5	4.971e-5	4.971e-5
Inlet	P_{in} [Pa]	1.828e5	3.257e5	1e5	1e5
	T_{in} [K]	416.3	416.4	606.5	606.5
	k_{in} [m^2/s^2]	20.55	20.55	0.18	15
	ω_{in} [1/s]	5e4	1.1e5	170	170
Outlet	P_{out} [Pa]	1.049e5	1.547e5	0.94e5	0.94e5
Wall	T_{wall} [K]	300.0	300	606.5	606.5
	U_{wall} [m/s]	0	0	0	0
	k_{wall} [m^2/s^2]	0	0	0	0

Bibliography

[1] M. Finnis and A. Brown, "Stability of a laminar boundary layer flowing along a concave surface," *Journal of Turbomachinery*, vol. 111, pp. 376–386, 1989.

[2] P. Dubrin and B. P. Reif, *Statistical Theory and Modeling for Turbulent Flows*. John Wiley and Sons, 2010.

[3] T. Arts and M. L. de Reuvroit, "Aero-thermal performance of a two-dimensional highly loaded transonic turbine nozzle guide vane: A test case for inviscid and viscous flow computations," *Journal of Turbomachinery*, vol. 114, pp. 147–154, 1992.

[4] R. Pecnik, J. A. Witteveen, and G. Iaccarino, "Assessment of uncertainities in modeling of laminar to turbulent transition for transonic flows," *Flow Turbulence and Combustion*, vol. 91, pp. 41–61, 2013.

[5] G. Nowak and W. Wroblewski, "Optimization of blade cooling system with use of conjugate heat transfer approach," *International Journal of Thermal Sciences*, vol. 50, pp. 1770–1781, 2011.

[6] R. Langtry and F. Menter, "Transition modeling for general cfd applications in aeronautics," *American Institute of Aeronautics and Astronautics*, vol. 522, pp. 1–14, 2005.

[7] R. B. Langtry, *A Correlation-Based Transition Model using Local Variables for Unstructured Parallelized CFD codes*. PhD thesis, Universitat Stuttgart, 2006.

[8] R. B. Langtry and F. R. Menter, "Correlation-based transition modeling for unstructured parallelized computational fluid dynamics codes," *American Institute of Aeronautics and Astronautics Journal*, vol. 47 No. 12, p. 2894, 2009.

[9] W. Elsner, "Transition modelling in turbomachinery," *Journal of theoretical and applied mechanics*, vol. 45, pp. 539–556, 2007.

[10] M. Shur, M. Strelets, A. Travin, and P. Spalart, "Turbulence modelling in rotating and curved channels: Assessing the spalart-shur correction," *American Institute of Aeronautics and Astronautics*, vol. 38 No.5, pp. 784–792, 2000.

[11] P. E. Smirnov and F. R. Menter, "Sensitization of the sst turbulence model to rotation and curvature by applying the spalart-shur correction term," *Journal of Turbomachinery*, vol. 131, pp. 041010–1, 2009.

[12] P. Spalart and M. Shur, "On the sensitization of turbulence models to rotation and curvature," *Aerospace Science and Technology*, vol. 5, p. 297, 1997.

[13] M. Clauser and F. Clauser, "The effect of curvature on transition from laminar to turbulent boundary layer.," tech. rep., NACA TN 613, 1937.

[14] H. Gortler, "On the three dimensional instability of laminar boundary layers on cancave walls," tech. rep., NACA TM 1375, 1940.

[15] L. Han and W. Cox, "A visual study of turbine blade pressure-side boundary layers," *Journal of Engineering for Power*, vol. 105, pp. 47–52, 1983.

[16] J. Howard, S. Patankar, and R. Bordynuik, "Flow prediction in rotating ducts using coriolis-modified turbulence models," *Journal of Fluids Engineering*, vol. 102, pp. 456–461, 1980.

[17] B. Launder, C. Priddin, and B. Sharma, "The calculation of turbulent boundary layers on spinning and curved surfaces," *Journal of Fluids Engineering*, vol. 99 No. 1, pp. 231–239, 1977.

[18] R. Pecnik, V. E. Terrapon, F. Ham, G. Iaccarino, and H. Pitsch, "Reynolds-averaged navier-stokes simulations of the hyshot ii scramjet," *American Institute of Aeronautics and Astronautics*, vol. 50 no. 8, p. 1717âĂŞ1732, 2012.

[19] F. R. Menter, "Two-equation eddy-viscosity turbulence models for engineering applications," *American Institute of Aeronautics and Astronautics Journal*, vol. 32 No 8, p. 1298, 1994.

[20] R. E. Mayle, "The role of laminar-turbulent transition in gas turbine engines," *Journal of Turbomachinery*, vol. 113, pp. 509–536, 1991.

[21] M. Opoka, R. Thomas, and H. Hodson, "Boundary layer transition on the high lift t106a low pressure turbine blade with an oscillating downstream pressure field," *Journal of Turbomachinery*, vol. 130, pp. 1–10, 2008.

[22] A. Savill, *Numerical Simulation of Unsteady Flows and Transition to Turbulence*, ch. A Synthesis of t3 Test Case Predictions, pp. 404–442. Cambridge University Press, 1992.

[23] D. Monson, H. Seegmiller, P. M. Connaughey, and Y. Chen, "Comparison of experiment with calculations using curvature corrected zero and two equation turbulence models for a two-dimensional u-duct," *American Institute of Aeronautics and Astronautics*, vol. 90-1484, pp. 1–19, 1990.

Modeling curvature effects on turbulence for turbomachinery flows

Master of Science Thesis

For the degree of Master of Science in Mechanical Engineering: Sustainable Process and Energy Technology at Delft University of Technology

Roberto Suarez Raspopov

July 11, 2013

Faculty of Mechanical, Maritime and Materials Engineering (3mE) · Delft University of Technology

Delft University of Technology
Department of
Energy Technology

The undersigned hereby certify that they have read and recommend to the Faculty of Mechanical, Maritime and Materials Engineering (3mE) for acceptance a thesis entitled

Modeling curvature effects on turbulence for turbomachinery flows

by

Roberto Suarez Raspopov

in partial fulfillment of the requirements for the degree of

Master of Science Mechanical Engineering: Sustainable Process and Energy Technology

Dated: July 11, 2013

Supervisor(s):

Dr.Ir. Rene Pecnik

Ir. Enrico Rinaldi

Reader(s):

Prof.Dr.Ir. Bendiks Jan Boersma

Dr.Ir. Arvind Gangoli Rao

Abstract

Turbulent flows that are subject to streamline curvature and rotation experience additional forces that can enhance or suppress turbulence. A particular case where streamline curvature and rotation play an important role is in flows over aircraft engine components; such as: flows over compressor and turbine blades, flows around the spinning discs carrying the blades in axial turbines, flows in cooling channels of rotating blades, and flows over curved diffuser passages between compressor and turbine stages. The turbulence in a boundary layer entering a convex curve is diminished by the centrifugal acceleration while the turbulence of a flow entering a concave surface is amplified. These changes in the turbulence levels can significantly affect the nature of the flow, and in particular, the laminar-to-turbulent transition process. The boundary layer transition typically occurs around compressor and turbine blades, which consist of a concave surface (pressure side) and a convex surface (suction side). The transition phenomena can significantly affect the frictional losses, efficiency, and heat transfer over the component. Therefore, further improvements in the engine performance require a thorough understanding of the curvature effects in the boundary layer development.

This thesis presents an analysis of the curvature effects on turbulent flows for turbomachinery applications and it documents the improvement in their prediction capability by standard turbulence and transition models coupled with a curvature correction term on a series of two dimensional flows. For this purpose, an in-house Reynolds-Averaged Navier-Stokes (RANS) solver [18] is used, and the curvature correction proposed by Spalart and Shur [12] is implemented in the $k-\omega$ shear stress transport (SST) model of Menter [19] and the $\gamma - Re_{\theta t}$ (ReT) transition model of Langtry and Menter [8].

The curvature correction is first validated on two well known test cases, namely a subsonic flow over an adiabatic flat plate [22], and the fully turbulent flow inside a U-duct channel [23, 11]. As expected, the results for the flat plate indicate that the curvature correction term has no effect on the solution. For the U-duct test case, the solution obtained from the curvature corrected SST model is closer to the experimental data than the original SST.

Next, the performance of the curvature correction is analyzed for two well documented turbomachinery test cases. The first one being the prediction of the heat transfer coefficient over a Von Karman Institute (VKI) transonic turbine guide vane [3], and the second the prediction of the pressure coefficient over the high lift T106 low pressure turbine blade [21]. For the VKI

test case, two different flow configurations are considered, both characterized by the presence of boundary layer transition over the suction side of the profile. The results obtained from the curvature corrected SST and the original SST models overestimate the heat transfer coefficient over the surface of the blade, and, in general, are not able to capture the transition. On the other hand, the ReT transition model is able to predict laminar-to-turbulent transition over the suction side. Moreover, when combined with curvature correction, the ReT model predicts the transition onset closer to the experimental data, providing a much more accurate calculation of the heat transfer coefficient.
Finally, for the T106 turbine blade two flow configurations with different turbulence intensities are considered. In the case of high freestream turbulence, transition occurs before the boundary layer separates. However, for the lower freestream turbulence case the boundary layer separates and transition occurs in the shear layer above the laminar separation bubble. Here, the transition model is essential for the predictive capability of the simulation and the results are in good agreement with experimental data. For the two different flow configurations no significant improvements are observed when using the curvature correction term.

Table of Contents

List of Figures

List of Tables

Acknowledgements

First, I want to thank my father and friend, Dr. Raúl Suárez Parra for providing me with the necessary education and support to pursue my dreams.
I have to thank my supervisor, Dr.Ir. Rene Pecnik for giving me the chance of working with him and providing me with the necessary guidance and support in order to finish this project. This thesis has been an important learning experience for me and has fulfilled my expectations.
I want to thank my daily supervisor, Ir. Enrico Rinaldi for his valuable assistance during the development of my thesis.
I am also grateful to Dr.Ir. Piero Colonna for his advice and support during the last year of my Master studies.
I want to thank the close friends I have made during my stay in the Netherlands, and in particular, Horacio Jimenez, Eduardo Allison and Hugo Cruz for sharing with me their experience, and showing me life from a different perspective.
Finally, I have to acknowledge the "Consejo Nacional de Ciencia y Tecnología" (CONACyT), for providing me with the financial support necessary to perform my Master studies in the Netherlands.

Delft, University of Technology — Roberto Suarez Raspopov
July 11, 2013

Chapter 1

Introduction

1-1 Motivation

In aircraft engines, especially in turbomachinery components, the Reynolds numbers that determine the evolution of the boundary layers are relatively low, hence a large part of the flow along the blades surface is laminar or transitional. The boundary layer development, losses, efficiency, and heat transfer are greatly affected by the location and extent of the laminar-to-turbulent transition. The ability to accurately predict the transition process is therefore crucial for the design of efficient and reliable machines [4].

The main goal of gas turbine development is to increase its thermodynamic performance which depends on several factors such as the turbine inlet temperature, the selection of the optimal compression ratio and system configuration (intercasing cooling, regeneration, etc). However, nowadays the most substantial source of improvement comes from increasing the turbine inlet temperature, which affects both the specific power and thermal efficiency of the cycle [5]. The development in this area has been possible due to the progress in material engineering, however, the temperatures are so high nowadays that the improvement of material performance and specific design of new materials is not sufficient and the application of cooling systems for the hot components is necessary. The cooling of gas turbine vanes demands for accurate estimates of the cooling system location within the components and the amount of cooling needed in order to achieve an economical use of the available cooling air supply. In addition, there is a trend towards achieving a higher power output per stage, necessitating larger turning angles in cascades. For these reasons, designers have to understand the development of the boundary layers on turbine airfoils to obtain as much information as possible to mitigate the frictional losses and heat transfer. Despite the technical maturity of gas turbines, the research, optimization and development concerning this technology still continues, as increasing the engine's performance by a small amount or improving the cooling system provides substantial economic benefits.

1-2 Laminar to Turbulent Transition

The heat transfer and boundary layer separation strongly depend on the condition of the boundary layer. In a turbulent boundary layer, heat transfer and friction losses can be about five times higher than in a corresponding laminar boundary layer. In general, boundary layers always change from a laminar to a turbulent state, whereby this process is called laminar to turbulent transition. The location and extent of the transition process depend on the Reynolds number, the freestream turbulence intensity, the pressure gradient and geometry of the walls.

In practice, there are three important modes of laminar to turbulent transition. The first mode is called *natural transition*, which starts with a weak instability in the laminar boundary layer and continues through various stages of amplified instability until the flow is fully turbulent. The second mode is called *separated flow transition* which occurs in a separated laminar boundary layer. The third mechanism is called *bypass transition* and is caused by large disturbances in the external flow such as freestream turbulence. This is the most common mode of transition in gas turbine engines.

At present, there are mainly three concepts used to model transition in industry [6]. The first one is the application of low Reynolds number turbulent models, which are relatively easy to implement and in some cases are capable of predicting transition in three dimensional flows. Low Reynolds number turbulence models employ damping functions that are designed to predict the viscous sublayer behaviour. These models do not require wall functions. In order to predict transition they rely on the diffusion of turbulence from the freestream into the boundary layer and the interaction of this freestream turbulence with the model source terms [7]. On the other hand, a few of these models were found to predict transition at reasonable Reynolds numbers when the freestream turbulence level was sufficiently high. The ability of these models to predict transition seems to be coincidental and is due to the similarities between the viscous sublayer and the developing laminar boundary layer where the production of turbulence is damped.

The second approach is the so called e^N method, which is based on the local, linear stability theory and the parallel flow assumption in order to calculate the growth of the disturbance amplitude from the boundary layer neutral point to the transition location. It requires three successive steps: the first step consists of the calculation of the laminar velocity and temperature profiles along the body of interest. In the second step the local growth rates of the unstable waves are computed for each of these profiles. This can be accomplished by solving either the local stability equations or the Parabolized Stability Equations (PSE). In the third step, the local growth rates are integrated along each stream line in order to determine the N factor. Once the disturbance amplitude ratio (e^N) exceeds the limiting N factor transition is assumed to start. One issue with the e^N method is that the N factor does not represent the amplitude of a disturbance in the boundary layer, but rather the amplification factor from an initial unknown amplitude. This initial amplitude of the disturbance is related to external disturbance environment through an unknown receptivity process. For this reason, the limiting factor N must be determined by calibration to wind tunnel or flight tests making from the e^N approach a semi-empirical method. However, there are several drawbacks in applying the e^N method in general aerospace applications. The first is that since it is based on the linear stability theory, it cannot predict transition due to non-linear effects such as bypass transition or surface roughness induced transition. In addition, the need to track the

growth of the disturbance amplitude ratio along the streamline results in a significant issue for 3D flows where the streamline direction is not aligned with the grid [7].

The third approach for predicting transition, which is favoured by the gas turbine industry, is the use of experimental correlations. The empirical correlations usually relate the freestream turbulence intensity Tu to the transition Reynolds number based on the momentum thickness Reynolds number $Re_{\theta t}$. These correlations are attractive because they have been successfully used for several years and provide consistent results even when used in 3D structured Navier-Stokes codes. In order to employ an empirical correlation for a transition onset, the laminar solution around the body of interest must be first calculated. In a second step the boundary layer quantities are integrated to obtain the momentum thickness Reynolds number Re_θ along the whole body. The transition onset is then assumed to occur at the position where the local value of $Re_{\theta t}$ exceeds the one predicted by the correlation. Once the starting location of the transition is determined, a turbulence model is turned on and the subsequent flow development is calculated.

While empirical correlation methods prove to be sufficiently accurate, they present numerical and programming drawbacks in Navier-Stokes codes. As mentioned before, for correlation based transition models it is necessary to compare the actual momentum thickness Reynolds number Re_θ to the transition value from the correlation $Re_{\theta t}$. This represents a difficult task in a Navier-Stokes environment since the boundary layer edge is not well defined and the integration will therefore depend on the implementation of a search algorithm. In addition, there are serious difficulties regarding the implementation of non-local formulations in modern CFD codes based on unstructured grids and massive parallel execution. Unstructured grids do not easily provide the infrastructure needed to integrate global boundary layer parameters because the grid lines normal to the surface cannot be easily identified. In the case of a general parallelized code, the boundary layer can be divided between different CPU domains making the integration very complex to perform in parallel. Despite the implementation difficulties, empirical correlation methods are very attractive, as they allow for the inclusion of experimental data and additional parameters that are believed to affect transition. As a consequence, the accuracy of the empirical correlations can be improved as better experimental data on transition becomes available, and for this reason empirical correlations remain as an attractive method for predicting transition [7].

In this work, the recent $\gamma - Re_{\theta t}$ transition model proposed by Langtry and Menter in Ref. [8] will be used. The central mechanism by which this model operates is the intermittency parameter γ, which is the fraction of time for which the flow is turbulent at a certain location in space. The formulation proposed by Langtry and Menter is based on two transport equations. The first is an equation of the intermittency used to trigger the transition process by controlling the production term of kinetic energy in the boundary layer. The second transport is formulated in terms of the transition onset Reynolds number $Re_{\theta t}$. Outside the boundary layer, the transported variable is forced to follow the value of $Re_{\theta t}$ provided by the experimental correlation which is then diffused into the boundary layer. By this mechanism, the strong variations of turbulence intensity and pressure gradient in the freestream can be taken into account. At every location of the flow the local vorticity Reynolds number is compared to the transition Reynolds number to determine if the transition criterion is satisfied. If the vorticity Reynolds number exceeds the local transition Reynolds number, a source term in the intermittency equation is activated and turbulence is produced. In chapter 2 a detailed description of this method is provided.

1-3 The Role of Computational Fluid Dynamics

The understanding of the laminar to turbulent transition is important to incorporate new modeling methods into Computational Fluid Dynamics (CFD) codes, which are an effective and powerful tool in the design of turbomachinery components and other aerospace devices where wall shear stress or wall heat transfer are of interest. Currently, the transition modeling largely limits the quality of CFD codes, and the error in the estimation of the onset and extent of the transition can affect the calculated machine efficiency by several percent and the component life by more than an order of magnitude [9]. An important feature of thin shear flows around turbomachinery components is the presence of significant streamline curvature and rotation. For example the flow over compressor and turbine blades, the flow around the spinning discs carrying the blades in axial turbines, and the flow over curved diffuser passages between the compressor and turbine. For these type of flows streamline curvature and rotation exert additional forces which can change the turbulence levels in a boundary layer. These changes in the turbulence levels can affect the process of laminar to turbulent transition, the heat transfer and frictional losses over a surface.

Despite a fast growth of computer power and more and more intensive use, the Reynolds averaged Navier-Stokes equations still remain as the most widely used modeling approach in industrial applications. At the present, it is widely thought that linear eddy-viscosity turbulence models fail to accurately predict (or even fail to predict them at all) the effects of surface curvature and rotation [10]. Further progress in this area is often associated with Reynolds stress models (RSMs) [11]. The explicit appearance of rotation and curvature terms in the turbulence equations is cited as the fundamental advantage of RSMs over the simpler eddy viscosity models (EVMs). However, these models are not robust enough for practical applications in complex geometries [12]. Therefore, an effective alteration of the simple EVMs to incorporate curvature effects represents the most practical solution to the problem.

1-4 Curvature Effects

The surface curvature can suppress or amplify turbulence, depending on whether is convex or concave. The turbulence level in a boundary layer entering a convex curve (like the suction side of a turbine guide vane) is diminished by the centrifugal acceleration, while the turbulence of a flow entering a concave surface (pressure side) is amplified [2].

In 1937, Clauser and Clauser [13] recognized by means of experiments that laminar flows in a concave surface become turbulent at lower Reynolds numbers than on flat or convex surfaces. In his work, Görtler [14] determined that the laminar boundary layer on a concave surface becomes unstable as a result of centrifugal forces. The instability results in a secondary flow in the form of counter-rotating vortices (see Fig. 1-1) with axes parallel to the direction of the mean flow [1]. Görtler vortices have been observed by Han and Cox [15] in cascade flows. Their experiments suggested that the presence of the vortices could account for the increased heat transfer experienced on the turbine pressure surfaces. At the present, many rotation and/or streamline curvature (RC) corrections have been suggested in the literature. Howard et al. [16] performed a numerical analysis to predict the flow in a straight, radial rotating channel or rectangular cross section. The two equation $k - \varepsilon$ model was employed, with alternative modifications to include the influence of Coriolis force on the turbulent kinetic energy. The

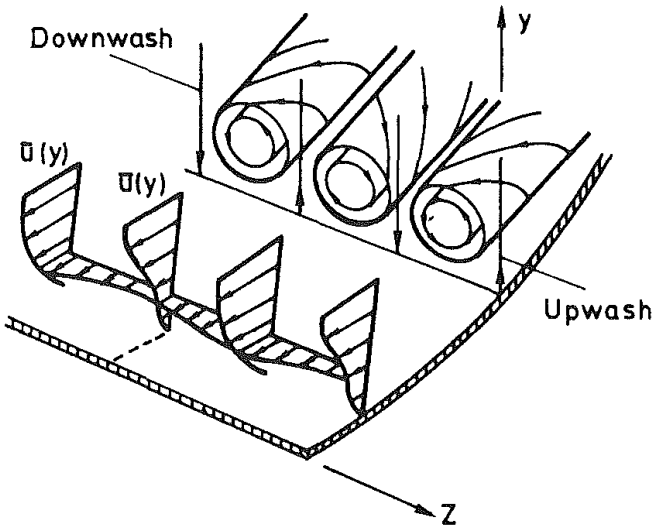

Figure 1-1: Görtler vortices in the boundary layer of a concave wall. (Adapted from Finnis and Brown [1].)

results shown moderate agreement with experimental data, confirming nevertheless the need for inclusion of Coriolis effects in the turbulence model.

Launder et al. [17] proposed an empirical coefficient to account for curvature effects which is directly proportional to the Richardson number Ri based on the eddy time scale (k/ϵ). The curvature correction term was implemented on the $k-\epsilon$ model by modifying the transport equation for the turbulent energy dissipation ϵ. The modified turbulence model was validated on a series of turbulent shear flows like the fully developed turbulent flow in a curved channel; and the boundary layer over a convex and concave surfaces. The results shown a moderate improvement over the results obtainable with the conventional $k-\varepsilon$ model.

Though the above mentioned corrections are moderately successful in the specific flows for which they were designed, they are still not universal, as they treat curvature and rotation differently, and, in addition, often suffer from Galilean non-invariance. In this work, the empirical function proposed by Spalart and Shur [12] to account for the effects of streamline curvature and rotation will be used. This correction term is based on intuitive arguments developed in thin shear layers, it is Galilean-invariant and fully defined in three dimensions.

1-5 Thesis Outline

The present work is concerned with curvature effects on the transition modeling over turbomachinery components. The curvature of a gas turbine guide vane can affect the extent an location of the laminar to turbulent transition over its surface. The purpose of this work is to improve the reliability of CFD calculations by incorporating the effect of surface curvature into the transition modeling. For this purpose, the Stanford University in-house Reynolds-Averaged Navier-Stokes (RANS) solver, developed by Pecnik et al. [18] is used. The curvature correction proposed by Spalart and Shur in Ref. [12] is implemented in the $k-\omega$ SST turbulence model coupled with the $\gamma - Re_{\theta t}$ transition model and the results of several test cases

are discussed.

The structure of this thesis is the following: in Chapter 2, a survey on turbulence modeling, transition and curvature effects is given. In chapter 3 the implementation of the curvature correction term in the RANS solver is discussed. Chapter 4 presents the results of implementing the curvature correction on four different test cases: a flat plate, a U-duct channel, the VKI turbine guide vane and the low pressure T106 blade profile. Finally, in Chapter 5 a brief summary and the conclusions of this thesis are given.

Chapter 2

Theoretical Framework

In the present chapter, a brief discussion of turbulence modeling, laminar to turbulent transition and curvature effects is provided. The $k-\omega$ SST turbulence model of Menter [19] and the $\gamma - Re_{\theta t}$ transition model proposed by Langtry and Menter [8] are presented. In addition, the modified Spalart and Shur correction term proposed by Smirnov and Menter [11] to account for curvature effects in turbulent flows is discussed.

2-1 Turbulence Modeling

The motion of a fluid is governed by the Navier Stokes equations. In the turbulent regime, the solution to these equations is a chaotic, three dimensional and unsteady. Such solutions are not easily obtained, even on massively parallel supercomputers. A much simpler level of description is required: this calls for a statistical approach. As it will be seen in the following, there are no closed equations for the statistics of turbulent flow, which means that there is a larger number of unknowns than equations. In the present survey only incompressible, constant density flow will be considered.

The equations governing incompressible flow, whether laminar or turbulent, are

$$\begin{aligned} \frac{\partial \tilde{u}_i}{\partial t} + \tilde{u}_j \frac{\partial \tilde{u}_i}{\partial x_j} &= -\frac{1}{\rho}\frac{\partial p}{\partial x_i} + \nu \nabla^2 \tilde{u}_i, \\ \frac{\partial \tilde{u}_i}{\partial x_i} &= 0. \end{aligned} \tag{2-1}$$

The first equation expresses the conservation of momentum. The second expresses the incompressibility of fluid volumes, which is equivalent to mass conservation in the present case. The total instantaneous velocity is denoted by $\tilde{u}$ and it can be decomposed in a mean velocity component U and a fluctuating component u, in other words $\tilde{u} = U + u$. The fluctuation u is usually referred to as the turbulence and U as the mean flow. If the previous decomposition

is substituted into Eqs. (2-1) they become

$$\begin{aligned} \frac{\partial}{\partial t}(U_i + u_i) + (U_j + u_j)\frac{\partial}{\partial x_j}(U_i + u_i) &= -\frac{1}{\rho}\frac{\partial}{\partial x_i}(P + p) + \nu\nabla^2(U_i + u_i), \\ \frac{\partial}{\partial x_i}(U_i + u_i) &= 0. \end{aligned} \tag{2-2}$$

The average of this equations is obtained by drawing a bar over each term, and considering that $\bar{U} = U$ and $\bar{u} = 0$:

$$\begin{aligned} \frac{\partial U_i}{\partial t} + U_j\frac{\partial U_i}{\partial x_j} &= -\frac{1}{\rho}\frac{\partial P}{\partial x_i} + \nu\nabla^2 U_i - \underbrace{\frac{\partial}{\partial x_j}\overline{u_j u_i}}, \\ \frac{\partial U_i}{\partial x_i} &= 0. \end{aligned} \tag{2-3}$$

These are the Reynolds-Averaged Navier-Stokes (RANS) equations. Equations (2-3) for the mean flow are the same as Eqs. (2-1), except for the last term of the momentum equation. This term is highlighted with an underbrace and corresponds to the derivative of the Reynolds stress tensor $\overline{u_i u_j}$.

The set of equations for the mean flow (2-3) define an unclosed mathematical problem because they are a set of four equations ($i = 1, 2, 3$) with ten unknowns (P; $U_i,\ i = 1, 2, 3$; and $\overline{u_j u_i},\ i = 1, 2, 3,\ j \leq i$). The extra six unknowns are the components of the Reynolds stress tensor. It is necessary to point out that the statistical problem (2-3) for the mean, or first moment requires knowledge of the covariance or second moment. This is because the Navier-Stokes equations have a quadratic non-linearity [2]. Any non-linearity causes moment equations to be unclosed; here the first moment equation contains second moments, the second moment equation will contain third moments.

The formulation of additional equations to obtain a solvable set of the Navier-Stokes equations (2-3) is called *closure modeling*. When the purpose is to predict non-homogeneous flow, possibly in complex engineering geometries, semi-empirical formulations to predict $\overline{u_i u_j}$ are required. In this work, an eddy viscosity model will be implemented. In this approach, the Reynolds stress tensor is explicitly related to the mean flow by a Newtonian constitutive equation with an eddy viscosity: $\overline{u_i u_j} = -2\nu_T S_{ij} + \frac{2}{3}\delta_{ij}k$. The term semi-empirical means that the model is obtained from a combination of theoretical analysis of simplified models, fluid mechanics, and experimental data. The semi-empirical model used here to calculate the eddy viscosity is the $k - \omega$ SST model and it will be described in detail in the following section.

2-2 The $k - \omega$ SST Model

The $k - \omega$ Shear Stress Transport model (SST) proposed by Menter in Ref. [19] utilizes the original $k - \omega$ model of Wilcox in the inner region of the boundary layer and switches to the standard $k - \epsilon$ model in the outer region and the free shear flow. In addition, it incorporates a modification of the definition of the eddy viscosity which accounts for the effect of the transport of the principal turbulent shear stress.

The $k-\omega$ model is chosen in the sublayer and the logarithmic part of the boundary layer since it has better performance than the $k-\epsilon$ model in equilibrium adverse pressure gradient flows and in compressible flows. On the other hand, the $k-\epsilon$ model is adopted in the wake region of the boundary layer and in free shear layers away from any surface. The reason is the high sensitivity of the $k-\omega$ model to the freestream values ω_f specified for ω outside the boundary layer.

In order to achieve the desired behaviour of the model in the different regions, the $k-\epsilon$ model is transformed into the $k-\omega$ formulation. It is then multiplied by the blending function $(1-F_1)$ and added to the original $k-\omega$ model times F_1. The blending function F_1 is designed to be zero in the wake region and to be one in the sublayer and the logarithmic region of the boundary layer. The original $k-\omega$ model is given by:

$$\frac{D\rho k}{Dt} = \tau_{ij}\frac{\partial U_i}{\partial x_j} - \beta^\star \rho\omega k + \frac{\partial}{\partial x_j}\left[(\mu+\sigma_{k1}\mu_t)\frac{\partial k}{\partial x_j}\right], \tag{2-4}$$

$$\frac{D\rho\omega}{Dt} = \frac{\gamma_1}{\nu_t}\tau_{ij}\frac{\partial U_i}{\partial x_j} - \beta_1\rho\omega^2 + \frac{\partial}{\partial x_j}\left[(\mu+\sigma_{\omega1}\mu_t)\frac{\partial \omega}{\partial x_j}\right]. \tag{2-5}$$

Next, the $k-\epsilon$ model is transformed into a $k-\omega$ formulation, where an additional cross-diffusion term appears in the ω equation. The transformed $k-\epsilon$ is given by

$$\frac{D\rho k}{Dt} = \tau_{ij}\frac{\partial U_i}{\partial x_j} - \beta^\star \rho\omega k + \frac{\partial}{\partial x_j}\left[(\mu+\sigma_{k2}\mu_t)\frac{\partial k}{\partial x_j}\right], \tag{2-6}$$

$$\frac{D\rho\omega}{Dt} = \frac{\gamma_2}{\nu_t}\tau_{ij}\frac{\partial U_i}{\partial x_j} - \beta_2\rho\omega^2 + \frac{\partial}{\partial x_j}\left[(\mu+\sigma_{\omega2}\mu_t)\frac{\partial \omega}{\partial x_j}\right] + 2\rho\sigma_{\omega2}\frac{1}{\omega}\frac{\partial k}{\partial x_j}\frac{\partial \omega}{\partial x_j}. \tag{2-7}$$

Now, Eqs. (2-4) and (2-5) are multiplied by F_1 while Eqs. (2-6) and (2-7) are multiplied by $(1-F_1)$ and the corresponding equations of each set are added to obtain the new model:

$$\frac{D\rho k}{Dt} = \tau_{ij}\frac{\partial U_i}{\partial x_j} - \beta^\star \rho\omega k + \frac{\partial}{\partial x_j}\left[(\mu+\sigma_{k}\mu_t)\frac{\partial k}{\partial x_j}\right], \tag{2-8}$$

$$\frac{D\rho\omega}{Dt} = \frac{\gamma}{\nu_t}\tau_{ij}\frac{\partial U_i}{\partial x_j} - \beta\rho\omega^2 + \frac{\partial}{\partial x_j}\left[(\mu+\sigma_{\omega}\mu_t)\frac{\partial \omega}{\partial x_j}\right] + 2*\rho(1-F_1)\sigma_{\omega2}\frac{1}{\omega}\frac{\partial k}{\partial x_j}\frac{\partial \omega}{\partial x_j}, \tag{2-9}$$

where any constant $\alpha \in (\sigma_{k1}, ...)$ is given by $\alpha = F_1\alpha_1 + (1-F_1)\alpha_2$, being α_1 and α_2 the constants of the original $k-\omega$ model and the transformed $k-\epsilon$ model respectively.

In order to account for the effect of the transport of the principal turbulent shear stress the eddy viscosity is redefined as

$$\nu_t = \frac{a_1 k}{\max(a_1\omega; \Omega F_2)}, \tag{2-10}$$

where a_1 is a constant, Ω is the absolute value of the vorticity and F_2 is a function that is one for boundary layer flows and zero for free shear layers.

2-3 Transition Prediction

The process by which a laminar flow turns into a turbulent one is called transition. The transition process and the important role played by the Reynolds number $Re = Ud/\nu$ in this transition was first pointed out by Reynolds in 1883. Reynolds was concerned with the water flow along a straight smooth pipe, where a filament of coloured fluid was introduced at the inlet (see Fig. 2-1). When the speed of the water was low, the filament remained distinct through the entire length of the tube. When the speed was increased, the filament broke up at a given point and diffused throughout the cross-section. In his paper, Reynolds distinguished these two flow regimes (laminar and turbulent) and he argued that the parameter that controlled the transition from wan regime to another had to be $Re = Ud/\nu$. He also noted that the critical value of Re at which turbulence first appears is very sensitive to disturbances at the entrance of the pipe.

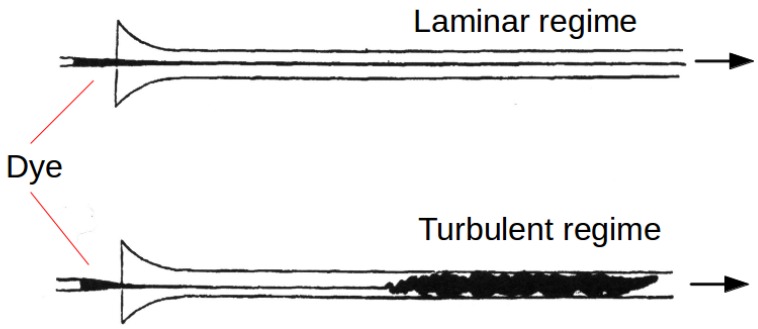

Figure 2-1: Schematic representation of Reynolds' observations in 1883. Reynolds distinguished two flow regime, laminar and turbulent, and he argued that the parameter that controlled the transition from wan regime to another had to be $Re = Ud/\nu$. (Adapted from Dubrin and Pettersson Reif [2].)

In general, there are three important modes of transition, natural, bypass and separated flow transition. Each one of these modes depends on the flow conditions such as the intensity of fluctuations in the freestream, roughness and geometry of the walls.

For the case of *natural transition*, it is presently known that it envolves several stages [20]. First, at a critical value of momentum thickness Reynolds number the boundary layer becomes susceptible to small disturbances and develops an instability in the form of a two dimensional Tollmien-Schlichting wave. Second, the instability amplifies in the layer to a point where three-dimensional instabilities grow and develop into loop vortices with large fluctuations. Finally, the highly fluctuating portions of the flow develop into turbulent spots, which then grow and convect downstream within the boundary layer to eventually merge into a fully developed turbulent boundary layer. In the case of *bypass transition*, at high freestream turbulence levels, the first and possibly the second stages of the natural transition are omitted (or bypassed) such that the turbulent spots are directly produced within the boundary layer by the influence of freestream disturbances. For this case, no Tollmien-Schlichting waves are

found.

Finally, when a laminar boundary layer separates, transition may occur in the free-shear-layer-like flow near the surface, this is called *separated flow transition*. In this case, the flow may reattach as turbulent forming a laminar separation/turbulent reattachment bubble on the surface. In gas turbines separated flow transition is common and may occur in an over-speed region near an airfoil's leading edge on either the suction side, the pressure side or both. Long bubbles can produce large losses and deviations in exit flow angles, for this reason they should be avoided. On the other hand, short bubbles are an effective way to force the flow to become turbulent and this can be considered as a means to control performance [20]. One of the difficulties in transition modelling is to predict whether the bubble will be large or short.

In order to predict the transition process one could rely directly on the turbulence model such as the $k-\omega$ SST which was described in the previous section. It is necessary to mention that most of the transport equation models such as $k-\epsilon$ and $k-\omega$ do converge to a laminar solution at low Reynolds numbers and to a turbulent solution at sufficiently high Reynolds number exhibiting a transition in between (see Fig. 2-2). However, turbulence models are in

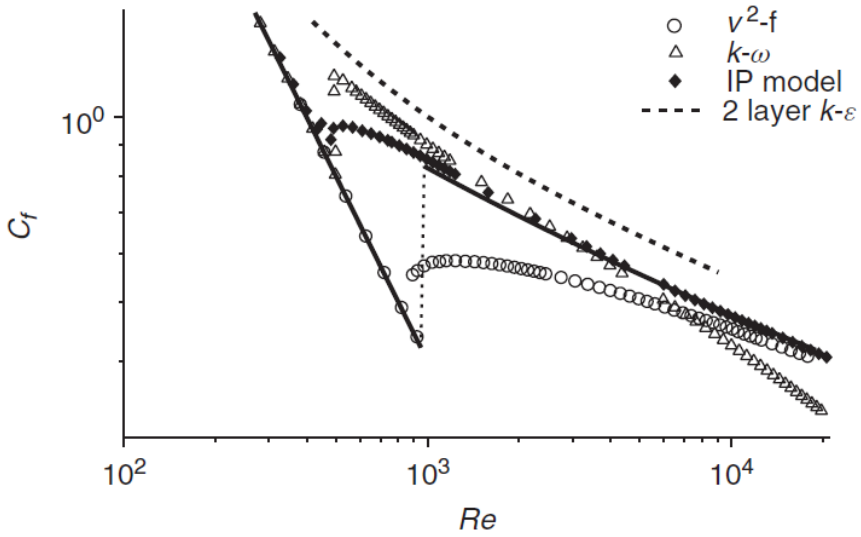

Figure 2-2: Skin friction coefficient in a plane channel versus Reynolds number based on the centerline velocity and channel half width. Many turbulence models display laminar to turbulent transition as the Reynolds number increases. (From Dubrin and Pettersson Reif [2].)

general developed for fully turbulent conditions and calibrated with turbulence data. Their ability to capture accurately the transition mechanism is a property of the model equations, not of the fluid dynamical mechanisms. For this reason, the prediction of laminar to turbulent transition provided by turbulence models is seriously limited and therefore a different approach is required. In this work, the recent $\gamma - Re_{\theta t}$ transition model proposed by Langtry and Menter [8] will be used. The central idea behind this model is to use an intermittency parameter γ to modulate the production of turbulent kinetic energy in the turbulence model. The intermittency γ takes values from 0 to 1 and represents the probability that a given point is located inside a turbulent region. A detailed description of the $\gamma - Re_{\theta t}$ transition model is provided in the next section.

2-4 The $\gamma - Re_{\theta t}$ Transition Model

In the present section the $\gamma - Re_{\theta t}$ correlation based transition model proposed by Langtry and Menter in [8] is described. This model is built strictly on local variables making it compatible with modern CFD techniques such as unstructured grids and parallel computation.

The $\gamma - Re_{\theta t}$ transition model is based on the transport equation for intermittency, which is used to trigger the transition locally. In addition, a second transport equation is solved for the transition onset momentum thickness Reynolds number $Re_{\theta t}$. This is required to capture the non-local influence of turbulence intensity, which changes due to the decay of the turbulence kinetic energy in the freestream, as well as to changes in the freestream velocity outside the boundary layer. This second transport equation ties the empirical correlation to the onset criteria in the intermittency equation.

The transport equation for intermittency is given by

$$\frac{\partial \rho\gamma}{\partial t} + \frac{\partial}{\partial x_j}(\rho U_j \gamma) = P_\gamma + E_\gamma + \frac{\partial}{\partial x_j}\left[\left(\mu + \frac{\mu_t}{\sigma_f}\right)\frac{\partial \gamma}{\partial x_j}\right]. \tag{2-11}$$

The transition source is defined as

$$P_{\gamma 1} = F_{lenght} C_{a1} \rho S \sqrt{\gamma F_{onset}}(1 - c_{e1}\gamma), \tag{2-12}$$

where S is the strain rate magnitude and F_{lenght} is an empirical correlation that controls the length of the transition region. This function is based on a series of flat plate test cases and is defined as

$$F_{lenght} = \begin{cases} 398.189 \cdot 10^{-1} + (-119.270 \cdot 10^{-4})\tilde{Re}_{\theta t} + (-132.567 \cdot 10^{-6})\tilde{Re}_{\theta t}^2, & \tilde{Re}_{\theta t} < 400 \\ 263.404 + (-123.939 \cdot 10^{-2})\tilde{Re}_{\theta t} + (194.548 \cdot 10^{-5})\tilde{Re}_{\theta t}^2 + (-101.695 \cdot 10^{-8})\tilde{Re}_{\theta t}^3 & 400 \leq \tilde{Re}_{\theta t} \leq 596 \\ 0.5 - (\tilde{Re}_{\theta t} - 596.0) \cdot 3.0 \cdot 10^4 & 596 \leq \tilde{Re}_{\theta t} < 1200 \\ 0.3188 & 1200 \leq \tilde{Re}_{\theta t} \end{cases}$$

The function F_{onset} is used to trigger the intermittency production (i.e. activate Eq. (2-12)). It is designed to switch rapidly from a value of zero in a laminar boundary layer to a value of one at every location in the flow field where the local vorticity Reynolds number exceeds the local transition onset criteria. The transition onset is controlled by the following equations:

$$Re_v = \frac{\rho y^2 S}{\mu} \; ; \; R_T = \frac{\rho k}{\mu \omega}, \tag{2-13}$$

$$F_{onset1} = \frac{Re_v}{2.193 \cdot Re_{\theta c}}, \tag{2-14}$$

$$F_{onset2} = \min(\max(F_{onset1, F_{onset1}^4}), 2.0), \tag{2-15}$$

$$F_{onset3} = \max\left(1 - \left(\frac{R_T}{2.5}\right)^3, 0\right), \tag{2-16}$$

$$F_{onset} = \max(F_{onset2} - F_{onset3}, 0). \tag{2-17}$$

$Re_{\theta c}$ in Eq. (2-14) is the critical Reynolds number where the intermittency first starts to increase in the boundary layer. This occurs upstream of the transition Reynolds number $\tilde{Re}_{\theta t}$ because there is a delay due to the fact that turbulence must first build up to appreciable levels in the boundary layer before any change in the laminar profile can occur. For this reason, $Re_{\theta c}$ can be thought of as the location where turbulence starts to grow while $\tilde{Re}_{\theta t}$ is

the location where the velocity profile first starts to deviate from the purely laminar profile. The connection between the two must be obtained from an empirical correlation were

$$Re_{\theta c} = \begin{cases} \tilde{Re}_{\theta t} - 396.035 \cdot 10^{-2} + (-120.656 \cdot 10^{-4})\tilde{Re}_{\theta t} + (868.23 \cdot 10^{-6})\tilde{Re}_{\theta t}^2 \\ +(-696.596 \cdot 10^{-9})\tilde{Re}_{\theta t}^3 . (174.105 \cdot 10^{-12})\tilde{Re}_{\theta t}^4 & \tilde{Re}_{\theta t} \leq 1870 \\ \tilde{Re}_{\theta t} - (593.11 + (\tilde{Re}_{\theta t} - 1870) \cdot 0.482) & \tilde{Re}_{\theta t} > 1870 \end{cases} \tag{2-18}$$

and $\tilde{Re}_{\theta t}$ from the transport Eq. (2-22). This correlation is determined based on a series of numerical experiments on a flat plate where the critical Reynolds number was varied along with the freestream turbulence intensity and the subsequent transition Reynolds number was measured based on the most upstream location where the skin friction started to increase. The destruction or relaminarization source is defined as

$$E_\gamma = c_{a2}\rho\Omega\gamma F_{turb}(c_{es}\gamma - 1), \tag{2-19}$$

where Ω is the vorticity magnitude. This term acts like a sink term and ensures that the intermittency remains close to zero in the laminar boundary layer. It also enables the model to predict relaminarisation because it provides a means for the intermittency to return to zero once the transition criteria in the F_{onset} function is no longer satisfied. F_{turb} is used to disable the destruction/relaminarization source outside of a laminar boundary layer and is defined as follows:

$$F_{turb} = e^{-\left(\frac{R_T}{4}\right)^4}. \tag{2-20}$$

The boundary condition for γ at a wall is zero normal flux while at an inlet the value of γ is equal to 1. In order to capture the laminar and transitional boundary layers correctly, the grid must have a y^+ of approximately 1 [8].

The experimental transition correlations relate the Reynolds number of transition onset, $Re_{\theta t}$ to the turbulence intensity, Tu, and other quantities in the freestream where

$$Re_{\theta t} = f(Tu, ..)_{freestream}. \tag{2-21}$$

This is a non-local operation since the value of $Re_{\theta t}$ is required by the intermittency equation inside the boundary layer, and not only in the freestream. On the other hand, the turbulence intensity can change strongly inside the domain and one global value over the entire flowfield is not acceptable. In order to use only local quantities, a different way for passing information from the freestream to the boundary layer is required. The solution to this problem is provided by a second transport equation which treats the transition momentum thickness Reynolds number $Re_{\theta t}$ as a transported scalar quantity. An empirical correlation is used to calculate $Re_{\theta t}$ in the freestream and then its value is merged by the transport equation into the boundary layer. This transport equation essentially takes a non-local empirical correlation (i.e. Eq. (2-32)) and transforms it into a local quantity, which then can be used to compute the transition length F_{lenght} and the critical Reynolds number $Re_{\theta c}$ at every location of the flow field.

The transport equation for the transition onset momentum thickness Reynolds number is given by

$$\frac{\partial(\rho\tilde{Re}_{\theta t})}{\partial t} - \frac{\partial(\rho U_j\tilde{Re}_{\theta t})}{\partial x_j} = P_{\theta t} + \frac{\partial}{\partial x_j}\left[\sigma_{\theta t}(\mu + \mu_t)\frac{\partial\tilde{Re}_{\theta t}}{\partial x_j}\right]. \tag{2-22}$$

Outside the boundary layer, the source term $P_{\theta t}$ is designed to force the transported scalar $\tilde{Re}_{\theta t}$ to match the local value of $Re_{\theta t}$ calculated from an empirical correlation. The production term can be computed from the relations below:

$$P_{\theta t} = c_{\theta t}\frac{\rho}{t}(Re_{\theta t} - \tilde{Re}_{\theta t})(1 - F_{\theta t}), \tag{2-23}$$

$$t = \frac{500\mu}{\rho U^2} \tag{2-24}$$

$$F_{\theta t} = \min\left(\max\left(F_{wake}e^{-\left(\frac{y}{\delta}\right)^4}, 1 - \left(\frac{\gamma - 1/c_{e2}}{1 - 1/C_{e2}}\right)^2\right), 1\right), \tag{2-25}$$

$$\theta_{BL} = \frac{\tilde{Re}_{\theta t}\mu}{\rho U}\ ;\ \delta_{BL} = \frac{15}{2}\theta_{BL}\ ;\ \delta = \frac{50\Omega y}{U}\delta_{BL}, \tag{2-26}$$

$$Re_\omega = \frac{\rho\omega y^2}{\mu}\ ;\ F_{wake} = e^{\left(\frac{Re_\omega}{1\times10^5}\right)^2}, \tag{2-27}$$

were t is a time scale defined for dimensional reasons. The blending function $F_{\theta t}$ is used to turn off the source term in the boundary layer and allow the transported scalar $\tilde{Re}_{\theta t}$ to diffuse in from the freestream. $F_{\theta t}$ is equal to zero in the freestream and 1 in the boundary layer.

The following constants are used in the model:

$$c_{a1} = 1,\ c_{a2} = 0.03,\ c_{e2} = 50,\ \sigma_f = 1,\ c_{\theta t} = 0.03,\ \sigma_{\theta t} = 2. \tag{2-28}$$

During the development of the $\gamma - Re_{\theta t}$ model it was observed that whenever a laminar boundary layer separation occurred, the model predicted the turbulent reattachment location too far downstream. By comparison with experimental results it was found that the accuracy of the model tended to decrease as the freestream turbulence was lowered. The reason for this is that the turbulent kinetic energy k in the separating shear layer is smaller at lower freestream turbulence levels. As a consequence, it takes longer for k to become large enough to make the boundary layer to reattach. In order to solve this problem, the following modification to handle separation induced transition was implemented:

$$\gamma_{sep} = \min\left(s_1 \max\left[0, \left(\frac{Re_v}{3.235Re_{\theta c}}\right) - 1\right]F_{reattach}, 2\right)F_{\theta t}, \tag{2-29}$$

where,

$$F_{reattach} = e^{-\left(\frac{R_T}{20}\right)^4},\ s_1 = 2, \tag{2-30}$$

$$\gamma_{eff} = \max(\gamma, \gamma_{sep}). \tag{2-31}$$

This modification allows k to grow rapidly once the laminar boundary layer separates and has a negligible effect for attached transition. The main idea behind this correction is to allow the local intermittency to exceed 1 whenever the laminar boundary layer separates. This will result in a large production of k, which in turn will cause earlier reattachment. The size of the separation bubble is controlled with the constant s_1. The $F_{reattach}$ term disables the modification once the viscosity ratio is large enough to cause reattachment and $F_{\theta t}$ is the blending function that confines the modification to boundary layer type flows.

The boundary condition for $\tilde{Re}_{\theta t}$ at a wall is zero flux. The boundary condition for $\tilde{Re}_{\theta t}$ at and inlet should be calculated from an empirical correlation based on the inlet turbulence

intensity. The empirical correlation is defined as follows:

$$Re_{\theta t} = \left[1173.51 - 589.428Tu + \frac{0.2196}{Tu^2}\right] F(\lambda_\theta),\ Tu \leq 1.3, \tag{2-32}$$

$$Re_{\theta t} = 331.5[Tu - 0.5658]^{-0.671} F(\lambda_\theta),\ Tu > 1.3, \tag{2-33}$$

$$F(\lambda_\theta) = 1 - [-12.986\lambda_\theta - 123.66\lambda_\theta^2 - 405.689\lambda_\theta^3]e^{-\left(\frac{Tu}{1.5}\right)^{1.5}},\ \lambda \leq 0, \tag{2-34}$$

$$F(\lambda_\theta) = 1 + 0.275[1 - e^{[-35\lambda_\theta]}]e^{-\left(\frac{Tu}{0.5}\right)},\ \lambda > 0, \tag{2-35}$$

where,

$$\lambda_\theta = \frac{\rho\theta^2}{\mu}\frac{dU}{ds}, \tag{2-36}$$

$$Tu = 100\frac{\sqrt{2k/3}}{U}. \tag{2-37}$$

The derivative dU/ds corresponds to the acceleration along the streamwise direction and can be computed by taking the derivative of the velocity U in the x, y and z directions and the summing the contribution of these derivatives along the streamwise direction. The following constraints are introduced for numerical robustness:

$$-0.1 \leq \lambda_\theta \leq 0.1,\quad Tu \geq 0.027,\quad Re_{\theta t} \geq 20. \tag{2-38}$$

The transition model is coupled to the $k-\omega$ SST model through the use of the effective intermittency from Eq. (2-31) by modifying the production and dissipation terms in the k equation as follows:

$$\tilde{P}_k = \gamma_{eff} P_k,\quad \tilde{D}_k = \min(\max(\gamma_{eff}, 0.1), 1) D_k, \tag{2-39}$$

where P_k and D_k are the production and destruction terms in the turbulent kinetic energy of the original SST equation respectively. The final modification to the SST model is a change in the blending function F_1 which is responsible for the switching between the $k-\omega$ and $k-\epsilon$ models. The reason is that the original blending function could potentially switch from 1 to 0 in the center of the boundary layer, which is undesirable since the $k-\omega$ model should be active in the laminar and transitional boundary layers. The modified blending function is defined by

$$F_1 = \max(f_{1,orig}, F_3),\quad F_3 = e^{-\left(\frac{R_y}{120}\right)^8},\quad R_y = \frac{\rho y\sqrt{k}}{\mu}, \tag{2-40}$$

where $F_{1,orig}$ is the original blending function of the SST model.
In the following sections the physical effects of curvature are discussed and the curvature correction term proposed by Spalart and Shur [12] will be described in detail.

2-5 Curvature Effects on Turbulent Flow

The purpose of this section is to provide the physical explanation of curvature effects in turbulent flows. Surface curvature can suppress or amplify turbulence depending on whether it is convex or concave curvature. The turbulence in a boundary layer entering a convex curve is diminished by centrifugal acceleration, while the turbulence entering a concave curve is amplified. The shear is toward the center of curvature in the destabilizing case and outward

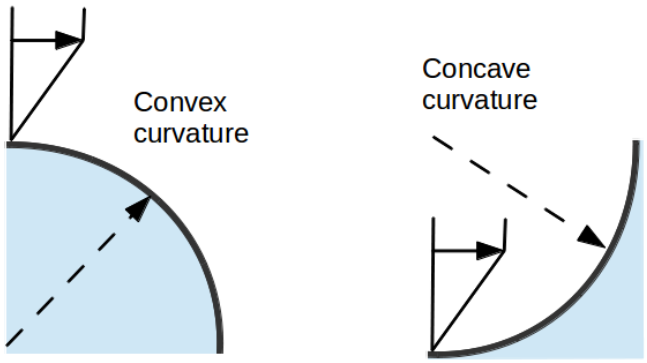

Figure 2-3: Schematic of boundary layers on curved surfaces. Convex curvature is stabilizing and concave is destabilizing. (Adapted from Dubrin and Reif [2].)

from it in the stabilizing. A schematic representation of this effect is shown in Fig. 2-3. The origin of curvature effects can be understood by an examination of the Reynolds stress transport equation, particularly the production term. The transport equation for the Reynolds stress tensor $\overline{u_i u_j}$ is given by

$$\begin{aligned}\frac{\partial \overline{u_i u_j}}{\partial t} + U_k \frac{\partial \overline{u_i u_j}}{\partial x_k} &= -\frac{1}{\rho}\left(\overline{u_j \frac{\partial p}{\partial x_i}} - \overline{u_i \frac{\partial p}{\partial x_j}}\right) - 2\nu \overline{\frac{\partial u_i}{\partial x_k}\frac{\partial u_j}{\partial x_k}} \\ &\quad - \frac{\partial \overline{u_k u_i u_j}}{\partial x_k} - \overline{u_j u_k}\frac{\partial U_i}{\partial x_k} - \overline{u_i u_k}\frac{\partial U_j}{\partial x_k} + \nu \nabla^2 \overline{u_i u_j},\end{aligned} \tag{2-41}$$

where $-\overline{u_j u_k}(\partial U_i/\partial x_k) - \overline{u_i u_k}(\partial U_j/\partial x_k)$ corresponds to the production term [2].
If we consider cylindrical coordinates, $x_1 = R\theta$ and $x_2 = r$, the shear flow in Fig. 2-3 is in x_1 direction $U = U(r)e_1$, where $e_1 = (-\sin\theta, \cos\theta)$ is the unit vector in the circumferential direction. The vector on the radial direction is $e_2 = (\cos\theta, \sin\theta)$. Then the velocity gradient has the following non-zero components:

$$\begin{aligned} e_1 \frac{\partial}{x_1} U(r) e_1 &= e_1 U(r) \frac{\partial e_1}{\partial x_1} = -e_1 e_1 \frac{U(r)}{R}, \\ e_2 \frac{\partial}{x_2} U(r) e_1 &= e_2 e_1 \frac{\partial U(r)}{\partial r}, \end{aligned} \tag{2-42}$$

and

$$\frac{\partial U_j}{\partial x_i} = \begin{Bmatrix} 0 & -\frac{U(r)}{R} & 0 \\ \frac{\partial U(r)}{\partial r} & 0 & 0 \\ 0 & 0 & 0 \end{Bmatrix} \tag{2-43}$$

By considering the previous velocity gradient, the non-zero components of the production term in the Reynolds stress transport equation (Eq. (2-41)) become

$$\begin{aligned} P_{11} &= -2\overline{u_1 u_2}\frac{\partial U_1}{\partial x_2} = -2\overline{uv}\frac{\partial U}{\partial r}, \\ P_{22} &= -2\overline{u_2 u_1}\frac{\partial U_2}{\partial x_1} = 2\overline{uv}\frac{U}{R}, \\ P_{12} &= -\overline{u_2 u_2}\frac{\partial U_1}{\partial x_2} - \overline{u_1 u_1}\frac{\partial U_2}{\partial x_1} = -\overline{v^2}\frac{\partial U}{\partial r} + \overline{u^2}\frac{U}{R}, \end{aligned} \tag{2-44}$$

and the turbulent kinetik energy production corresponds to

$$P = \frac{1}{2}(P_{11} + P_{22}) = -\overline{uv}\left(\frac{\partial U}{\partial r} - \frac{U}{R}\right). \tag{2-45}$$

On a convex wall the velocity increases in the radial direction; hence $\partial_r U > 0$. The two terms of P are opposite in sign and the curvature acts to diminish the production of turbulent kinetic energy by the mean shear. On the other hand, for the case of a concave wall $\partial_r U < 0$. The two terms of the right hand side of Eqs. (2-44) that contribute to P_{12} and P have the same sign. In this case curvature supplements the production by mean shear. From the previous analysis it becomes clear that concave curvature is destabilizing and amplifies the turbulence. In the following section, a correction term proposed by Spalart and Shur [12] in order to account for the effects of curvature in turbulence models will be presented.

2-6 Curvature Correction

It was previously shown that curvature affects the production terms of the Reynolds stress transport equation. The explicit appearance of these effects in the turbulent equations is cited as a fundamental advantage of the full Reynolds stress turbulence models, which intend to solve Eq. (2-41). However, these models are stiff and difficult to converge compared to the simple eddy viscosity models for complex engineering applications. For this reason, a more robust approach to account for curvature effects is to properly modify the simpler eddy viscosity models. The measure proposed by Spalart and Shur in [12] is based on intuitive arguments developed in thin shear layers, it is Galilean-invariant and fully defined in three dimensions which makes is possible to implement in any RANS solver.

Consider a thin shear flow with a velocity profile $U(y) = y$ and assume that $U_y > 0$ so that the spanwise vorticity $\Omega_z < 0$. For this type of flow it holds that $\overline{u^2} > \overline{v^2}$ which is equivalent to stating that the principal axes of the strain tensor are not aligned with those of the strain tensor, but rotated counterclockwise [12]. The curvature correction term proposed by Spalart and Shur relies on a central hypothesis, which states that under weak rotation or curvature turbulence is enhanced if the Reynolds stress principal axes are leading the strain axes or vice versa. In this context they propose to track the direction of the principal axes of the strain tensor. In a weakly curved thin shear flow, the flow direction, the direction of the strain principal axes, and that of the Reynolds stress axes all evolve at the same rate U/R. The strain axes are invariant and therefore usable in a simple turbulence model which leads to the quantity

$$e \equiv \frac{D\alpha}{Dt}, \tag{2-46}$$

where the angle α gives the direction of the strain tensor principal axes with respect to an inertial reference frame. The strain axes are invariant and the Lagrangian derivative of a quantity which is defined with respect to an inertial frame, $D\alpha/Dt$ is also Galilean invariant.

The direction of the strain tensor axes α is susceptible to system rotation. In a homogeneous rotating flow with system rotation rate Ω^{rot} and time independent deformation, $D\alpha/Dt = \Omega^{rot}$. If an inhomogeneous incompressible flow is considered, the Lagrangian derivative of α can be calculated for a two dimensional case by differentiating analytically the strain tensor eigensystem, which results in

$$\frac{D\alpha}{Dt} = \Omega^{rot} + \frac{1}{2(S_{11}^2 + S_{12}^2)} \left[S_{11} \frac{DS_{12}}{Dt} - S_{12} \frac{DS_{11}}{Dt} \right]. \tag{2-47}$$

The strain rate tensor S_{ij} and the Lagrangian derivative on the right hand side of Eq. (2-47) are defined with respect to the reference frame of the system, which is rotating at a rate Ω^{rot}. The sign of e is only relevant compared with that of the vorticity. The stress-strain misalignment is in the direction of the vorticity and the non dimensional quantity $\tilde{r} = e/\Omega_z$ is then suggested as a prime candidate. Small positive values of $\tilde{r}$ suppress turbulence activity; while small negative values enhance it. For the case of solid body rotation, the measure $\tilde{r}$ reduces to $e = \omega/2$, so that $\tilde{r} = 1/2$. In a pure azimuthal flow $U_\theta(r)$, $e = U_\theta/r$ sign $d[rU_\theta]/dr$. Therefore the streamline curvature is recovered per se, U_θ/r. The extension of Eq. (2-47) to three-dimensional flows is given by Eq. (2-52). The empirical function proposed by Spalart and Shur in Ref. [12] to account for effects of streamline curvature and system rotation is defined by

$$f_{rotation} = (1 + c_{r1}) \frac{2r^\star}{1 + r^\star} [1 - c_{r3} \tan^{-1}(c_{r2}\tilde{r})] - c_{r1}, \tag{2-48}$$

which was initially tested in the Spalart-Allarmas one-equation turbulence model. In order to incorporate the curvature correction to the $k - \omega$ SST turbulence model, equation (2-48) is replaced by Smirnov and Menter in Ref. [11] by f_{r1}, which is defined as

$$f_{r1} = \max[\min(f_{rotation}, 1.25), 0.0], \tag{2-49}$$

and it is used to control the production terms in the $k - \omega$ SST model equations as follows:

$$\frac{\partial(\rho k)}{\partial t} + \frac{\partial(\rho U_j k)}{\partial x_j} = P_k f_{r1} - \beta^\star \rho k \omega + \frac{\partial}{\partial x_j} \left[\mu_{ref} \frac{\partial k}{\partial x_j} \right]. \tag{2-50}$$

$$\frac{\partial(\rho \omega)}{\partial x_j} + \frac{\partial(\rho U_j \omega)}{\partial x_j} = \alpha \frac{\rho P_k}{\mu_t} f_{r1} - D_\omega + Cd_\omega + \frac{\partial}{\partial x_j} \left[\mu_{ef} \frac{\partial \omega}{\partial x_j} \right]. \tag{2-51}$$

The difference between Eqs. (2-48) and (2-49) is that the latter limits the function values from 0 which corresponds to a strong convex curvature (stabilized flow, no turbulence production) to 1.25 corresponding to strong concave curvature (enhanced turbulence production). The lower limit is proposed for numerical stability reasons whereas the upper limit is used to avoid overgeneration of eddy viscosity in flows with destabilizing curvature or rotation. The arguments in Eq. 2-48 are defined as follows:

$$\tilde{r} = 2\Omega_{ik} S_{jk} \left[\frac{DS_{ij}}{Dt} + (\varepsilon_{imn} S_{jn} + \varepsilon_{jmn} S_{in}) \Omega_m^{rot} \right] \frac{1}{\Omega D^3}, \tag{2-52}$$

$$r^\star = \frac{S}{\Omega}, \tag{2-53}$$

where Ω_m^{rot} are the components of the system rotation vector in three dimensions and ε_{ijk} is the tensor of Levi-Civita. The different terms in Eqs. (2-52) and (2-53) are given by

$$S_{ij} = \tfrac{1}{2}\left(\tfrac{\partial U_i}{\partial x_j} + \tfrac{\partial U_j}{\partial x_i}\right), \tag{2-54}$$

$$\Omega_{ij} = \tfrac{1}{2}\left(\left(\tfrac{\partial U_i}{\partial x_j} - \tfrac{\partial U_j}{\partial x_i}\right) + 2\varepsilon_{mji}\Omega_m^{rot}\right), \tag{2-55}$$

$$S^2 = 2S_{ij}S_{ij}, \tag{2-56}$$

$$\Omega^2 = 2\Omega_{ij}\Omega_{ij}, \tag{2-57}$$

$$D^2 = \max(S^2, 0.09\omega^2), \tag{2-58}$$

and DS_{ij}/Dt are the components of the Lagrangian derivative of the strain tensor. Smirnov and Menter [11] suggest a technique to calculate this term for a three-dimensional Navier-Stokes CFD solver based on the control volume method. This technique will be applied in the RANS solver and its implementation is discussed in Chapter 3. In order to apply the control volume method, the material derivative DS_{ij}/Dt is expressed using the integral (Eulerian) flow formulation, which states that the total derivative of each component of the strain tensor in an arbitrary volume τ can be written as

$$\int_\tau \frac{DS_{ij}}{Dt}\, d\tau = \frac{D}{Dt}\int_\tau S_{ij}\, d\tau = \frac{\partial}{\partial t}\int_\tau S_{ij}\, d\tau + \int_\sigma S_{ij}U_n\, d\sigma, \tag{2-59}$$

where the first term on the right hand side corresponds to the local derivative and the second term is the convective derivative. Here σ is the surface of the volume τ, $U_n = \vec{U}\cdot\hat{n}$, $\vec{U}$ and $\hat{n}$ are the velocity and normal vectors at the integration point.

For steady state flows the first term in the right hand side of Eq. (2-59) is zero in converged solutions so there is no need to compute it during iterations. Then

$$\frac{D}{Dt}\int_\tau S_{ij}\, d\tau = \int_\sigma S_{ij}U_n\, d\sigma. \tag{2-60}$$

The application of the control volume approach to discretize the right hand side of Eq. (2-60) results in

$$\int_\sigma S_{ij}U_n\, d\sigma \;\rightarrow\; \sum_{k=1}^{N} S_{ij}^{(k)}U_n^{(k)}\sigma^{(k)}, \tag{2-61}$$

where the summing is done over the N surfaces of the control volume. The superscript (k) refers to the centres of the faces, σ^k is the area of the k-th face while $S_{ij}^{(k)}$ and $U_n^{(k)}$ are computed at the face centres. The final discrete formula for DS_{ij}/Dt is computed from Eq. (2-61) by dividing through the cell volume

$$\frac{DS_{ij}}{Dt} = \left[\sum_{k=1}^{N} S_{ij}^{(k)}U_n^{(k)}\sigma^{(k)}\right]\frac{1}{\tau}, \tag{2-62}$$

where τ is the volume of the computational cell. Finally, the constants c_{r1}, c_{r2} and c_{r3} in Eq. (2-48) are 1.0, 2.0 and 1.0 respectively. In the next chapter the data structure of the RANS solver will be presented and the implementation of the curvature correction term in the code will be discussed.

Chapter 3

Numerical Method

The purpose of this chapter is to document the implementation of the Spalart and Shur [12] curvature correction term in the in-house Reynolds-Averaged Navier-Stokes (RANS) solver developed at Stanford University by Pecnik et al [18]. In section 3-1 a brief descriprion of the solver's data structures is provided. Based on this data structure, section 3-2 describes the algorithm to calculate the curvature correction factor.

3-1 Data Structure of the RANS Solver

The RANS solver is entirely written in C++ language and it solves the compressible Navier-Stokes equations on unstructured meshes with a discretization based on the finite volume formulation and implicit time integration scheme on arbitrary polihedral mesh elements [4]. The data structure of the solver employs the centers of the control volumes, the faces and the nodes of the mesh (as shown in Fig. 3-1) to manipulate information. The cell centers store the

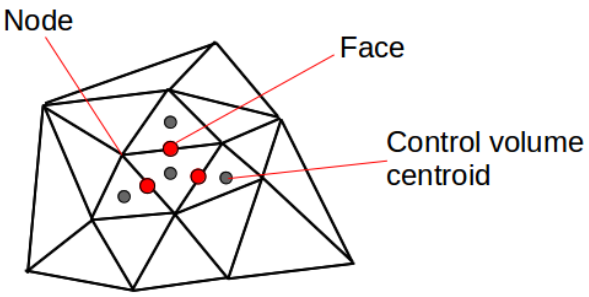

Figure 3-1: The data structure of the RANS solver requires the centers of the control volumes, the faces and the nodes to store information.

physical information of the flow (P, ρ, $\vec{V}$... etc.) and every face inside the mesh is associated

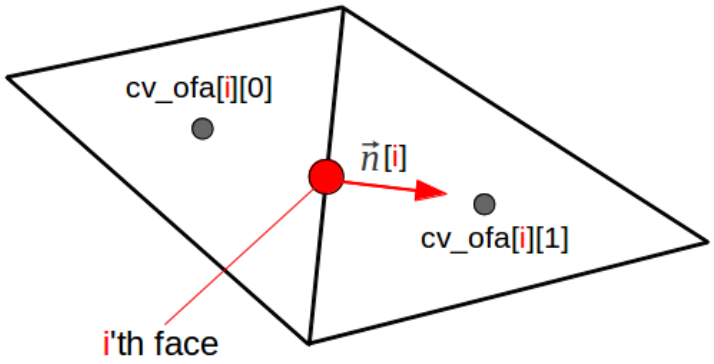

Figure 3-2: Every face in the mesh is associated with the two neighboring control volume centers, which are denoted as cv_ofa[i][0] and cv_ofa[i][1], where i is the index of the face and the second index denotes the left and right control volume of the face. In addition, every face is associated with a vector normal to it's surface which points in the opposite direction of node cv_ofa[i][0] and has the magnitude of the face area.

with two neighboring control volumes. These control volumes are denoted by cv_ofa[i][0] and cv_ofa[i][1] where i is the index of the face. In addition, every face is associated with a vector normal to its surface which points in the same direction as the vector connecting cv_ofa[i][0] to cv_ofa[i][1] and has the magnitude of the face area. This is schematically illustrated in Fig. 3-2. The following section describes the algorithm to calculate the curvature correction factor based on the data structure previously described.

3-2 Curvature Correction Algorithm

The algorithm presented in this section calculates the curvature correction factor in every cell center of the mesh at every time step. The correction factor f_{r1} is given by Eq. 2-49, where the $f_{rotation}$ term is calculated from Eq. 2-48, which reads

$$f_{rotation} = (1 + c_{r1})\frac{2r^\star}{1 + r^\star}[1 - c_{r3}\tan^{-1}(c_{r2}\tilde{r})] - c_{r1}.$$

The arguments in Eq. 2-48 are defined as follows:

$$\tilde{r} = 2\Omega_{ik}S_{jk}\left[\frac{DS_{ij}}{Dt} + (\epsilon_{imn}S_{jn} + \epsilon_{jmn}S_{in})\Omega_m^{rot}\right]\frac{1}{\Omega D^3},$$
$$r^\star = \frac{S}{\Omega}.$$

The physical properties in the previous equations such as S and Ω are defined in every cell center. However, the total derivative of the strain tensor DS_{ij}/Dt is not defined. For this reason, before evaluating Eq. 2-48, it is necesary to compute DS_{ij}/Dt over each cell center of the grid. This can be achieved by making use of the descrete formula (Eq. 2-62) provided

by Smirnov and Menter [11]:

$$\frac{DS_{ij}}{Dt} = \left[\sum_{k=1}^{N} S_{ij}^{(k)} V_n^{(k)} \sigma^{(k)}\right] \frac{1}{\sigma},$$

where the summing is done over the N faces of the control volume. The superscript (k) refers to the centres of the face, σ^k is the area of the k-th face while $S_{ij}^{(k)}$ and $V_n^{(k)}$ are computed at the face centres. The τ factor corresponds to the volume of the computational cell.

In order to evaluate Eq. (2-62) at every cell center of the mesh a first subroutine is created. This subroutine performs a cycle over the faces of the complete computational mesh and adds the contribution of each face to its neighboring control volume centers. The algorithm is repeated for every time step of the solver and can be summarized as follows:

1 For every face k in the mesh calculate the distances d_0 and d_1 from face center to the neighboring control volumes cv_ofa[i][0] and cv_ofa[i][1].

2 Using the velocity gradient of each cell center calculate the velocity at the i-th face:

$$\vec{V}_{0,face} = \vec{V}_0 + \nabla\vec{V}_0 \cdot \vec{dx}_{0,face},$$
$$\vec{V}_{1,face} = \vec{V}_1 + \nabla\vec{V}_1 \cdot \vec{dx}_{1,face},$$

where $\vec{V}_0$ and $\vec{V}_1$ are the velocity vectors, and $\nabla\vec{V}_0$ and $\nabla\vec{V}_1$ are the velocity gradients at the nodes [0] and [1] respectively. The vectors $\vec{dx}_{0,face}$ and $\vec{dx}_{1,face}$ represent the relative position between the cell centers and the k-th face.

3 Calculate the average velocity at the k-th face using

$$\vec{V}_k = \frac{\vec{V}_{1,face} * d_0 + \vec{V}_{0,face} * d_1}{d_0 + d_1}.$$

4 Using the same type of averaging calculate the strain tensor value S_{ij} over the i-th face.

5 Calculate the $V_n^{(k)}\sigma^{(k)}$ factor from Eq. 2-62: In order to achieve this, the dot product between the normal vector (recall that the magnitude of the normal vector equals the area of the face $\sigma^{(k)}$) and the average velocity vector in the k-th face is performed:

$$V_n^{(k)}\sigma^{(k)} = \vec{n} \cdot \vec{V}_k.$$

6 Calculate the contribution of the k-th face to the $\frac{DS_{ij}}{Dt}$ value of each one of the neighboring control volume centers:

$$\frac{DS_{ij}}{Dt}[0] = \frac{DS_{ij}}{Dt}[0] + (S_{ij}^{(k)} V_n^{(k)} \cdot VA) * \frac{1}{\tau_0},$$
$$\frac{DS_{ij}}{Dt}[0] = \frac{DS_{ij}}{Dt}[1] - (S_{ij}^{(k)} V_n^{(k)} \cdot VA) * \frac{1}{\tau_1}.$$

The contribution is added or substracted by considering the correct sign for the summation of the fluxes based on the Green-Gauss theorem. The normal vector is always pointing from index [0] to [1] of the control volumes. Then, at the boundary the normal vector is always pointing outside the domain.

Once the total derivative of the strain tensor DS_{ij}/Dt has been computed on every cell center of the mesh, a second subroutine is used to evaluate Eqs. (2-48) and (2-49) in order to provide the correction factor at every cell center. Once evaluated, the correction factor interacts with the $k-\omega$ SST turbulence model through the production terms of the k and ω equations as described in section 2-6. The C++ subroutines that calculate DS_{ij}/Dt and f_{r1} are included in Appendix A. In the following chapter the curvature correction term is implemented in a series of test cases and a detailed discussion of the results is provided.

Chapter 4

Results

In the present chapter the implementation of the algebraic curvature correction term is validated for four different 2D test cases and a discussion of the results is provided. The first two cases correspond to a flow over an adiabatic flat plate [22] and the fully turbulent flow inside a U-duct channel [11, 23]. These tests are performed to ensure the correct implementation of the curvature correction term in the RANS solver. Then, in order to assess the improvement in the predictive capability of the solver, the correction term is tested on two well documented turbomachinery test cases. The first one being the prediction of the heat transfer coefficient over a Von Karman Institute (VKI) transonic turbine guide vane [3], and the second the prediction of the pressure coefficient over a high lift T106 low pressure turbine blade [21].

In order to test the performance of the curvature correction term, four different model configurations are used along this chapter. The $k-\omega$ SST turbulence model of Menter [19] is used in its original form or combined with the $\gamma - Re_{\theta T}$ transition model of Langtry and Menter [8], the modified curvature correction term of Smirnov and Menter [11] or both. The different configurations are shown in Tab. 4-1, where the first column indicates the abbreviations which are used hereafter.

Table 4-1: Four different numerical schemes used to assess the performance of the curvature correction term. Each scheme is a combination of the $k-\omega$ SST turbulence model with the $\gamma - Re_{\theta T}$ transition model, the curvature correction term or both.

Abbreviation	**Turbulence model (SST)**	**Transition model (ReT)**	**Curvature correction (CC)**
SST	✓	-	-
SST-CC	✓	-	✓
SST-ReT	✓	✓	-
SST-ReT-CC	✓	✓	✓

4-1 Flat Plate

The purpose of the present test case is to compare the predictions of the turbulence model combined with the transition model with and without curvature correction (SST-ReT and SST-ReT-CC models) for a subsonic flow over a flat plate. Since a flat surface has no curvature, the Spalart and Shur correction term must not affect the solution and the results of both calculations should be identical. The flow conditions correspond to the test case T3A, with zero pressure gradient boundary layer documented by Savill [22]. The boundary conditions of the problem are presented in Appendix B.

The computational domain was provided by Dr. Rene Pecnik and it consists of 5120 control volumes divided by an H-type grid which provides a resolution of $y^+ < 0.3$ at the walls. Figure 4-1 shows the skin friction coefficient c_f over the plate as a function of the Reynolds number Re_x, which is calculated based on the distance between the leading edge of the plate and a generic location x over its surface. The skin friction coefficient is defined by

$$c_f = \frac{\tau_w}{\frac{1}{2}\rho_\infty U_\infty^2}, \tag{4-1}$$

where $\tau_w = \mu(\partial U/\partial y)$ is the local wall shear stress, ρ_∞ and U_∞ are the freestream density and velocity, respectively. From Fig. 4-1 it is possible to distinguish the transition process by the sudden increase of the skin friction coefficient from the laminar flow region at $Re_x = 15000$ to the turbulent one $Re_x = 27000$. In addition, the comparison between the curvature corrected solution (SST-ReT-CC) with the non-corrected one (SST-ReT) shows that the curvature correction has no effect on the flow over a flat plate.

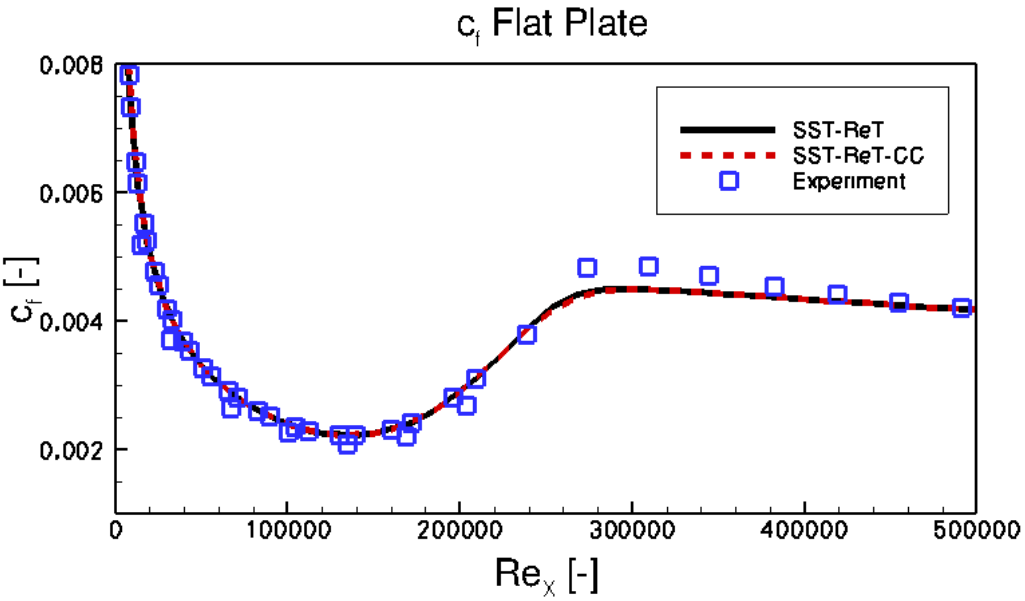

Figure 4-1: Skin friction coefficient as a function of the Reynolds number Re_x over an adiabatic flat plate. The Reynolds number Re_x is calculated based on the distance between the leading edge of the plate and the particular point x over the surface of the plate.

4-2 Two-Dimensional Flow in a U-Duct Channel

In the present section the results of a two-dimensional flow in a U-duct channel are presented. The objective of this test is to compare the results of the numerical method against experimental data provided by Monson and Seegmiller [23] and the simulations carried out by Smirnov and Menter [11] in order to ensure the correct implementation of the curvature correction term.

The fluid motion through a U-duct channel is a well known case which is characterized by a strong streamline curvature and it contains flow separation and reattachment on the inner (convex) wall of the duct. In addition, the flow upstream the U-bend is turbulent and fully developed. These features represent a challenge for the different RANS solvers and a thorough test for turbulence models.

The mesh of the computational domain is shown in Fig. 4-2 and it consists of 26307 elements clustered at the walls to ensure y^+ values of nearly 0.1. The computational grid of the U-duct test case was generated in the course of this work by a mesh generating program developed in-house at the TU Delft by Ir. Enrico Rinaldi. The Reynolds number of the flow, based on the channel width H and the mean flow velocity U_m is set equal to $Re = 10^6$ as specified in Refs. [23] and [11]. Additionally, the reference Mach number is set to $M = 0.1$ at the inlet in order to avoid compressibility effects. In order to guarantee a fully developed turbulent flow and the specified value of Reynolds number Re at the inlet of the computational domain, the boundary conditions of the problem are set as follows. In accordance with Ref. [11], fully developed profiles of velocity, density and turbulence properties are calculated for a straight channel in a pre-processing step and then specified as the inlet boundary condition for the U-tube. At the outlet of the domain a constant value of static pressure is fixed. The sides of the channel are considered symmetrical and a no slip condition is specified on the walls. For sake of completeness, the specific values of the boundary conditions used for the U-duct and the straight channel computations are included in Appendix B. In order to provide a comparison with the numerical results of Smirnov and Menter [11], the fully turbulent numerical solutions (SST and SST-CC) are used.

Figures 4-3 and 4-4 show the skin friction coefficient defined by Eq. (4-1) over the inner and outer walls of the U-duct channel. The skin friction coefficient is calculated over the walls by considering the position coordinate along the central line of the U-duct. From Fig. 4-3 it is possible to observe that the flow accelerates when entering the curve ($s = 0$) which translates in an increase of c_f, and separation occurs on the inner wall near the position $s = 2.5$ which is reflected by the negative sign of c_f. Later on, at $s = 5$ flow reattaches and the skin friction coefficient becomes positive. On the other hand, no separation is observed on the outer wall of the channel since c_f remains positive all the time. Figures 4-7 (d)-(f) show the turbulent kinetic energy in the normal direction of the wall at different positions of the channel. At the angles of 0 and 90 degrees of the U-turn (Figs. 4-7 (d)-(e)), it can be clearly seen that the curvature correction term reduces the turbulence levels over the inner wall, which translates in lower values of the skin friction coefficient of the SST-CC model compared to the non-corrected SST. Additionally, the curvature correction enhances the turbulence levels over the concave region of the outer wall, resulting in higher values of the skin friction coefficient of the SST-CC model.
Figures 4-5 and 4-6 show the pressure coefficient over the inner and outer walls of the U-duct.

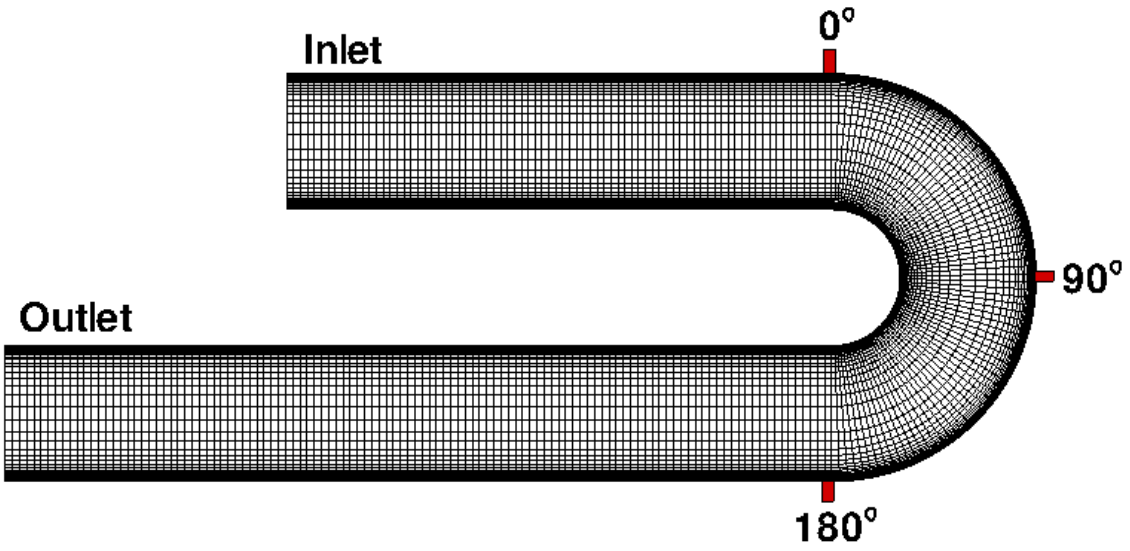

Figure 4-2: Computational domain and grid used for the U-duct channel. The width of the channel is 3.81 cm and the inner radius of the U-bend is 1.91 cm as specified by Monson and Seegmiller [23].

The pressure coefficient is defined as

$$c_p = \frac{P - P_\infty}{\frac{1}{2}\rho_\infty U_\infty^2}, \tag{4-2}$$

where p is the static pressure over the surface, p_∞ is the reference pressure, ρ_∞ and U_∞ are the freestream density and average velocity specified at the inlet of the channel. Figures 4-7 (a)-(c) show the velocity profiles at different sections of the U-duct. From figures (a) and (b) there is no visible effect of the curvature correction on the velocity profile. However, from figure (c) (angle of 180^o) it is possible to observe that the non-corrected SST model predicts early flow reattachment as the velocity value near to the inner wall is close to zero. The curvature correction reduces the turbulence levels over the inner (concave) surface of the wall, which delays the reattachment point (see also Fig. 4-3) and translates in a higher velocity value near the wall.

The calculations performed in this section are in good agreement with the experimental results and show a positive effect of the curvature correction on the SST turbulence model. Moreover, the results correspond to the numerical calculations of Smirnov and Menter [11]. From these results, in combination to the ones obtained in the previous section, it is possible to conclude that the curvature correction is correctly implemented in the RANS solver.

4-3 Von-Karman Institute (VKI) Transonic Turbine Guide Vane

In the present section the curvature correction is tested for the flow computation around a VKI transonic turbine guide vane. The VKI profile was experimentally investigated by Arts et al. in Ref. [3]. The experiments were performed in a compression tube facility in order

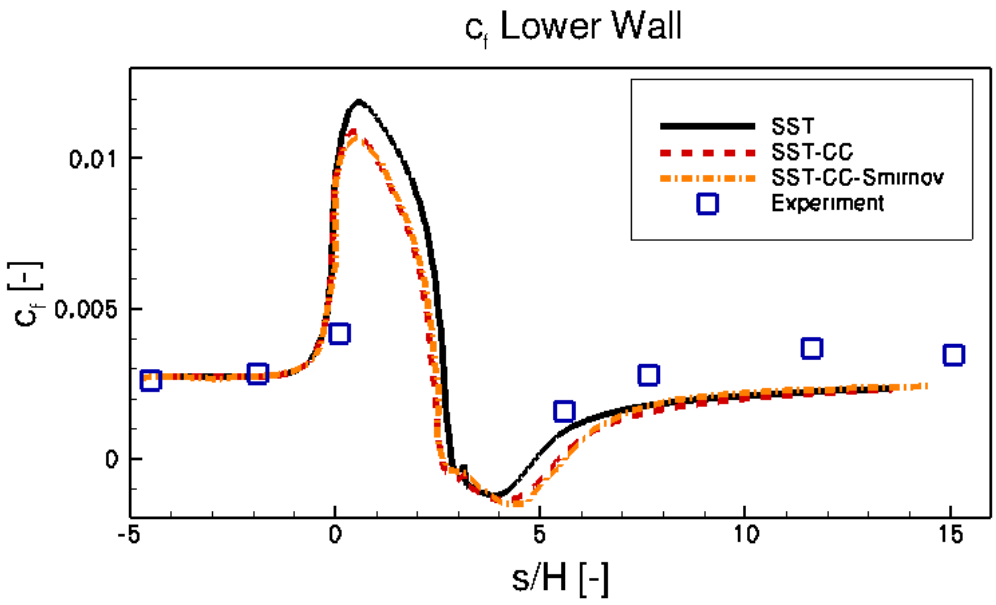

Figure 4-3: Skin friction coefficient c_f along the inner wall of the U-duct. The x axis represents the distance along the central line of the U-duct normalized with respect to the width H.

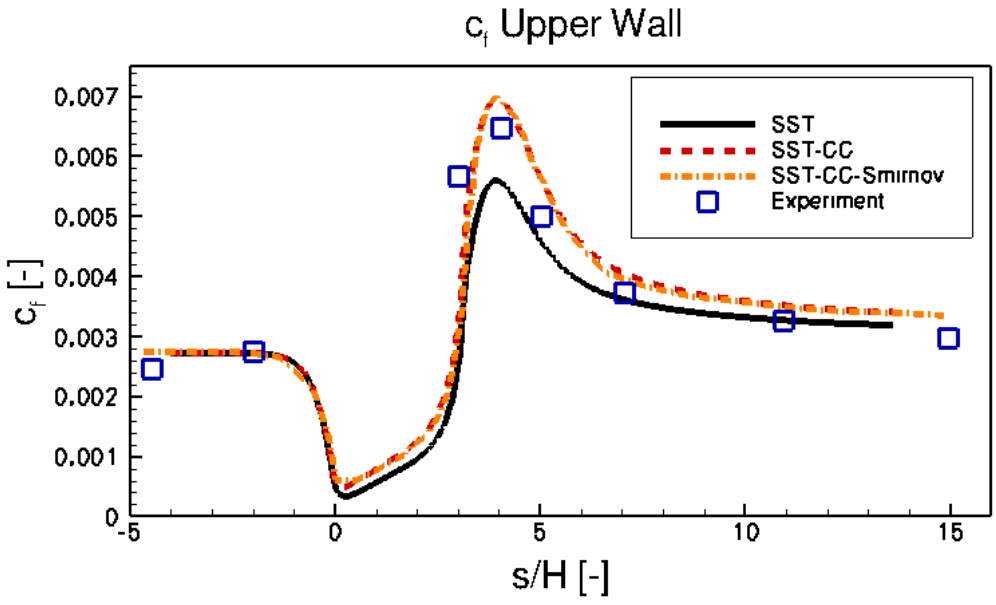

Figure 4-4: Skin friction coefficient c_f along the upper wall of the U-duct. The x axis represents the distance along the central line of the U-duct normalized with respect to the width H.

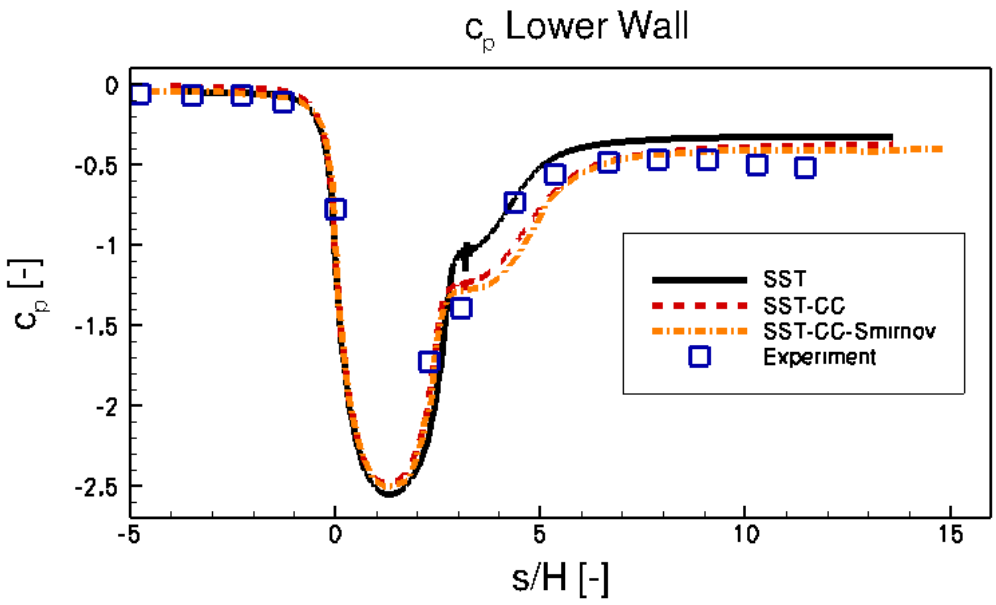

Figure 4-5: Pressure coefficient c_p along the inner wall of the U-duct. The x axis represents the distance along the central line of the U-duct normalized with respect to the width H.

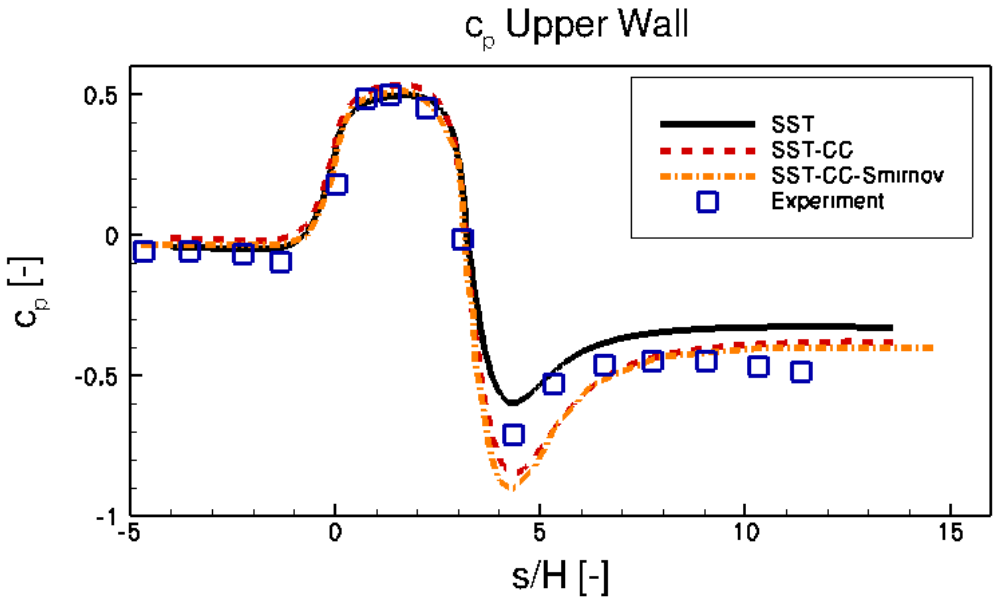

Figure 4-6: Pressure coefficient c_p along the upper wall of the U-duct. The x axis represents the distance along the central line of the U-duct normalized with respect to the width H.

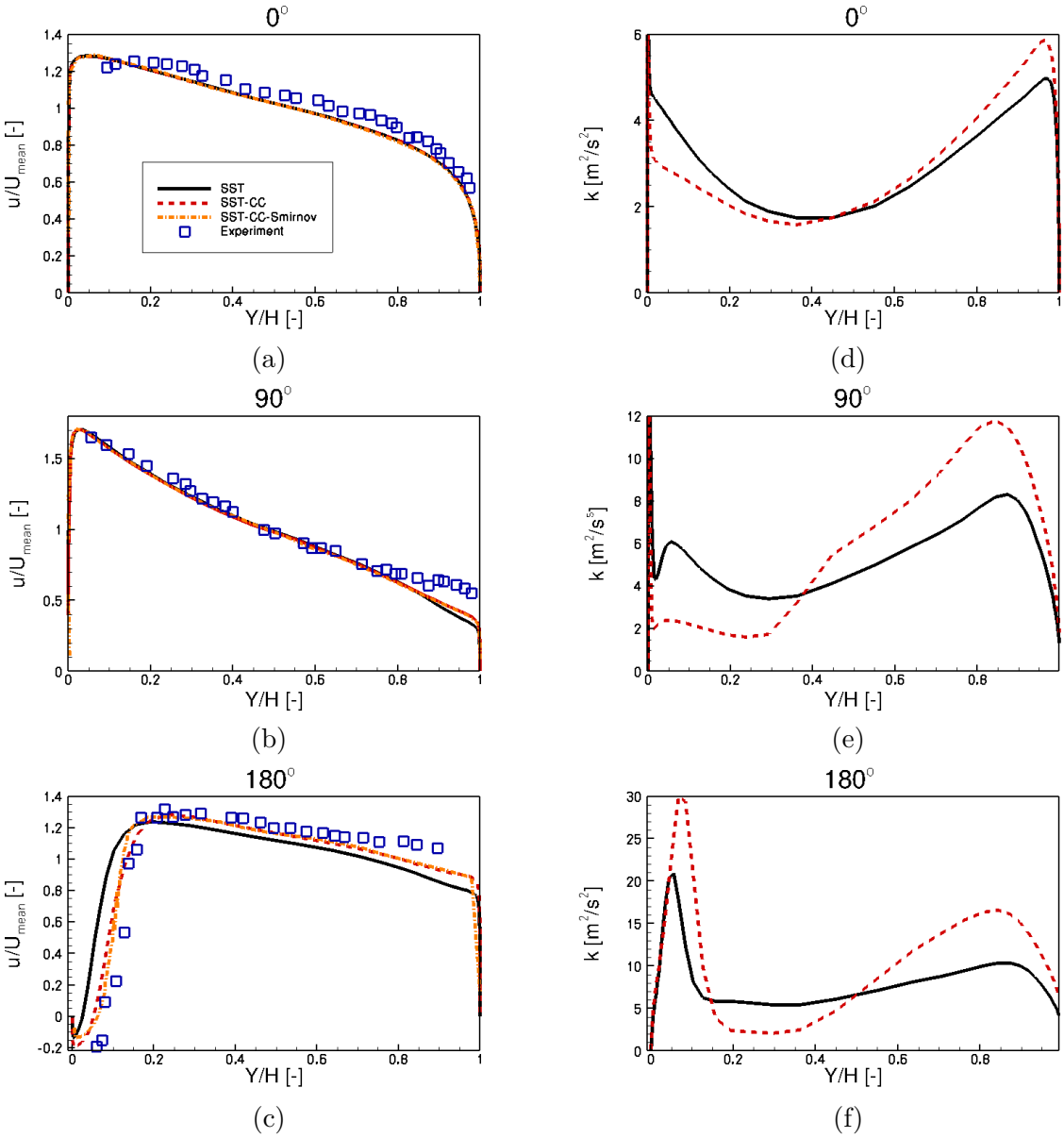

Figure 4-7: Turbulent kinetic energy (right side) and streamwise velocity (left side) profiles at different locations of the U-duct. The velocities are normalized with respect to the mean velocity at the inlet of the channel. The x-axis shows the position coordinate perpendicular to the wall normalized by the channel width.

Table 4-2: Geometrical characteristics of the VKI turbine guide vane.

Parameter	Value	
Chord	67.647	[mm]
Pitch to chord	0.85	[-]
Stagger angle	55^o	[-]
Throat to chord	0.2207	[-]

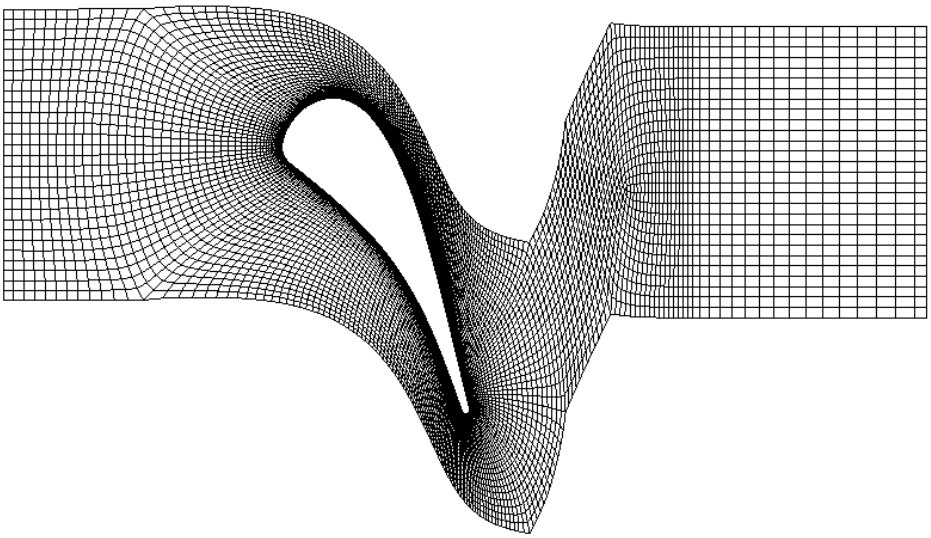

Figure 4-8: Computational domain of the VKI transonic guide vane. The grid consists of 25000 control volumes providing a resolution of $y^+ < 1$ at the first cell-row at the blade surface.

to study the influence of Mach number, turbulence intensity, and Reynolds number on the transitional heat transfer distribution. The most important blade characteristics are given in Tab. 4-2. The computational domain used for the present calculations (Fig. 4-8) was provided by Dr. Rene Pecnik and it consists of 25000 control volumes with a grid resolution of $y^+ < 1$ at the first cell-row at the blade surface. The reference temperature T_∞ is prescribed to be 416 K, while the temperature of the blade T_w is kept constant at 300 K. The heat transfer coefficient h is calculated based on the predicted heat flux q_w and the difference between the total and the wall temperatures:

$$h = \frac{q_w}{T_\infty - T_w}.$$

The numerical calculations are performed for the two different flow conditions (cases MUR235 and MUR241), which are summarized in Tab. 4-3. For each test case, the four different numerical schemes shown in Tab. 4-1 are used in order to assess the influence of the transition model and the curvature correction on the solution. The specific values of the boundary conditions used for the the MUR235 and MUR241 test cases can be found in Appendix B.

Figures 4-9 and 4-10 show the heat transfer coefficient as a function of the curvilinear coordinate along the blade s/c normalized by the chord for the MUR235 and the MUR241 test cases. Positive values of s/c indicate the suction side, while negative values of s/c correspond to the pressure side of the blade. From the experimental data it is possible to observe laminar to turbulent transition on the suction side due to a sharp increase in the heat

Table 4-3: Data of the VKI turbine guide vane test cases, where $M_{is,out}$ and $Re_{c,out}$ are the isentropic Mach number and the Reynolds number based on the chord length, both calculated at the outlet region. Re_M is the Reynolds number based on the velocity and mesh spacing of the turbulence grid in the experimental setup, used to calculate the specific dissipation rate ω [4].

	$Tu\%$	$M_{is,out}$	$Re_{c,out}$	Re_M
MUR235	6.0	0.927	1.15×10^6	61700
MUR241	6.0	1.089	2.11×10^6	61700

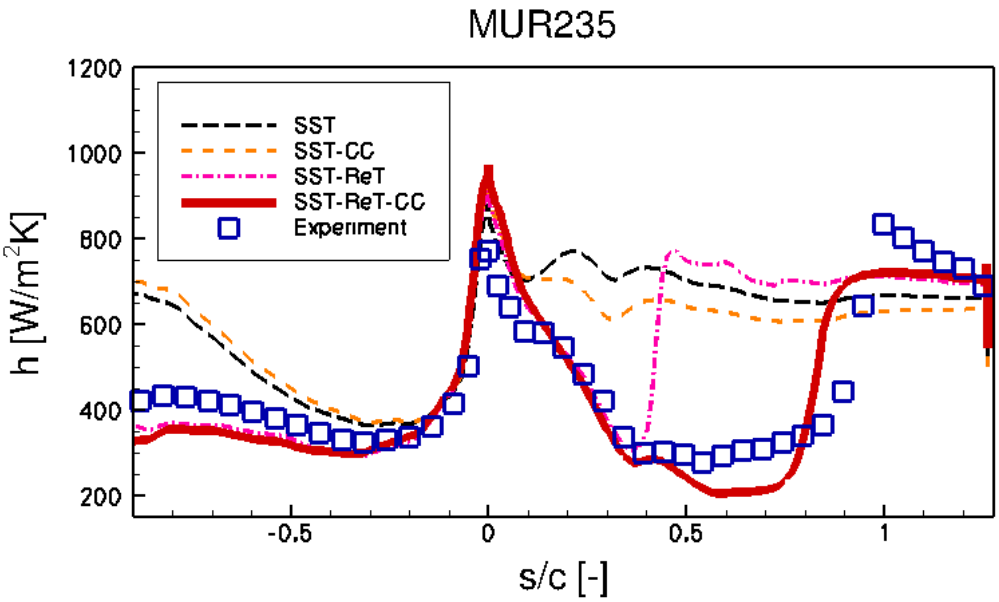

Figure 4-9: Heat transfer coefficient over the VKI blade profile for the MUR235 test case. The different lines represent numerical calculations while the squares represent the experimental results of Arts et al. [3]. Positive values of s/c indicate the suction side, while negative values of s/c correspond to the pressure side of the blade.

transfer coefficient; at $s/c = 0.8$ for the MUR235 and at $s/c = 0.6$ for the MUR241 case. On the other hand, none of the test cases exhibits transition on the pressure side as the variations of the heat transfer coefficients are smooth. From the numerical calculations it is possible to observe that the SST and the SST-CC schemes in general overestimate the heat transfer coefficient along the surface. Both solutions present smooth oscillations in the heat transfer coefficient over the suction side, for this reason no transition point can be distinguished. This is an expected result as the SST model was developed for a fully turbulent boundary layer and does not take transition into account. On the other hand, by comparing these two models some trends in the qualitative behaviour of the curvature corrected solution can be provided. In both test cases, the MUR235 and MUR241 it is possible to observe that the curvature correction term mitigates the turbulence levels on the suction side (concave surface) which translates in a lower heat transfer coefficient of the SST-CC model compared to the fully turbulent SST. Furthermore, the turbulence levels are enhanced by the curvature correction over the pressure side (concave surface), which translates in a higher heat transfer coefficient.

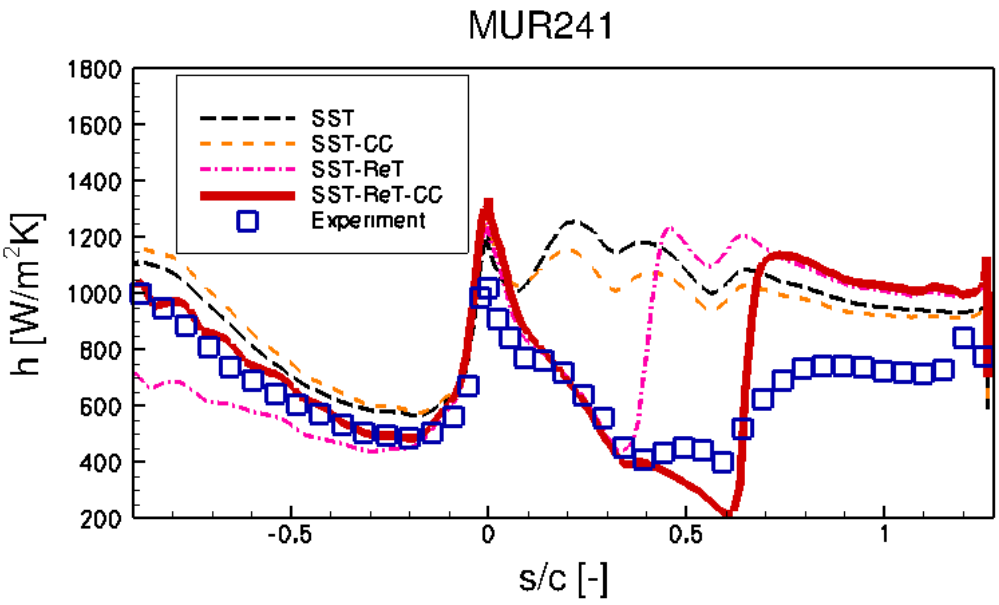

Figure 4-10: Heat transfer coefficient over the VKI blade profile for the MUR241 test case. The different lines represent numerical calculations while the squares represent the experimental results of Arts et al. [3]. Positive values of s/c indicate the suction side, while negative values of s/c correspond to the pressure side of the blade.

From the results of the SST-ReT calculations it is possible to distinguish laminar to turbulent transition over the suction side for both, MUR235 and MUR241 test cases. Nevertheless, despite the ability of the $\gamma - Re_{\theta t}$ model to predict transition there is a large deviation between the calculated transition point and the experimental data. It is necessary to notice that the transition model is based on empirical correlations derived from incompressible flat plate experiments that control the onset and extent of the transition. The critical Reynolds number $Re_{\theta c}$ determines where the intermittency first starts to grow and F_{lenght} controls the extent of transition. Therefore, these deviations from the experimental data can be expected as the complexity of the flow geometry increases.

On the other hand, the results from the turbulence model with transition and curvature correction (SST-ReT-CC) show for both test cases a delay in the transition point which improves the agreement with the experimental data. This effect is the consequence of the curvature correction factor, which decreases the turbulence levels in the boundary layer over a concave surface (suction side). The reduction of the turbulence levels in the boundary layer cause the transition model to trigger the onset further downstream. This can be seen from Fig. 4-12, which shows the turbulent kinetic energy and velocity distributions in the normal direction of the blade for the MUR241 test case at different positions over the surface. These locations are schematically indicated in Fig. 4-11.

Figures 4-12 (a)-(c) show that the turbulent kinetic energy predicted by the curvature corrected model SST-ReT-CC is lower over the suction side than the one predicted by the non-corrected model SST-ReT. In particular, at the position $s/c = 0.6$ the non corrected model predicts a fully turbulent boundary layer which is reflected by the high values of k.

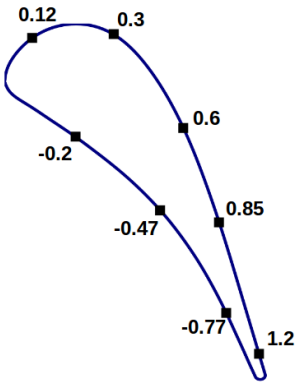

Figure 4-11: Schematic representation of the VKI profile and the different points where the turbulent kinetic energy is calculated.

At positions $s/c = 0.85$ and $s/c = 1.2$ the flow predicted by both models is fully turbulent, however, the turbulent kinetic energy predicted by the corrected solution decays more rapidly. For the pressure side (Figs. 4-12 (f)-(h)), the turbulent kinetic energy predicted by the corrected solution is higher than then the non-corrected one. The pressure side of the profile is a concave surface which translates in a higher value of the correction factor which enhances turbulent kinetic energy production. The same situation occurs for the MUR235 case resulting in similar graphs which are not included here. Figure 4-13 shows the skin friction coefficient c_f for both test cases calculated with the SST-ReT-CC method. As before, it is possible to distinguish the transition point over the suction side of the airfoil which corresponds to a sharp increase in c_f. In addition, the skin friction coefficient always stays positive which indicates that no flow separation occurs over the surface.

4-4 T106 Low-Pressure Turbine Blade

In the present section the curvature correction term is applied to a 2D steady state flow computation around a high-lift low-pressure turbine blade, named T106 in the literature. This test case is of high interest as of today there is a trend to increase the lift coefficients of low pressure (LP) turbine blades in order to reduce engine weight and cost. The Reynolds numbers of LP turbine blades range from about 0.5×10^5 in the final stage at high altitude in small business jet applications to about 5×10^5 at sea level takeoff in the first stage of the largest turbofans [21]. Given these Reynolds numbers and the lift coefficients of modern LP turbines, boundary layer transition and separation play an important role in determining engine performance at different operating conditions.

The T106 profile was experimentally investigated by Opoka et al. in Ref. [21]. The geometrical characteristics of the T106A case are summarized in Tab. 4-4. The inlet conditions correspond to a total temperature T_{in} of 606.5 K and a total pressure P_{in} of 1 bar. The numerical calculations were performed for the two different flow conditions which are summarized in Tab. 4-5. According to Opoka et al. [21], the turbulence intensity values in the second column of Tab. 4-5 are measured in the absence of the blade, at a location corresponding to the leading edge of the profile. In order to guarantee these turbulence levels in the T106

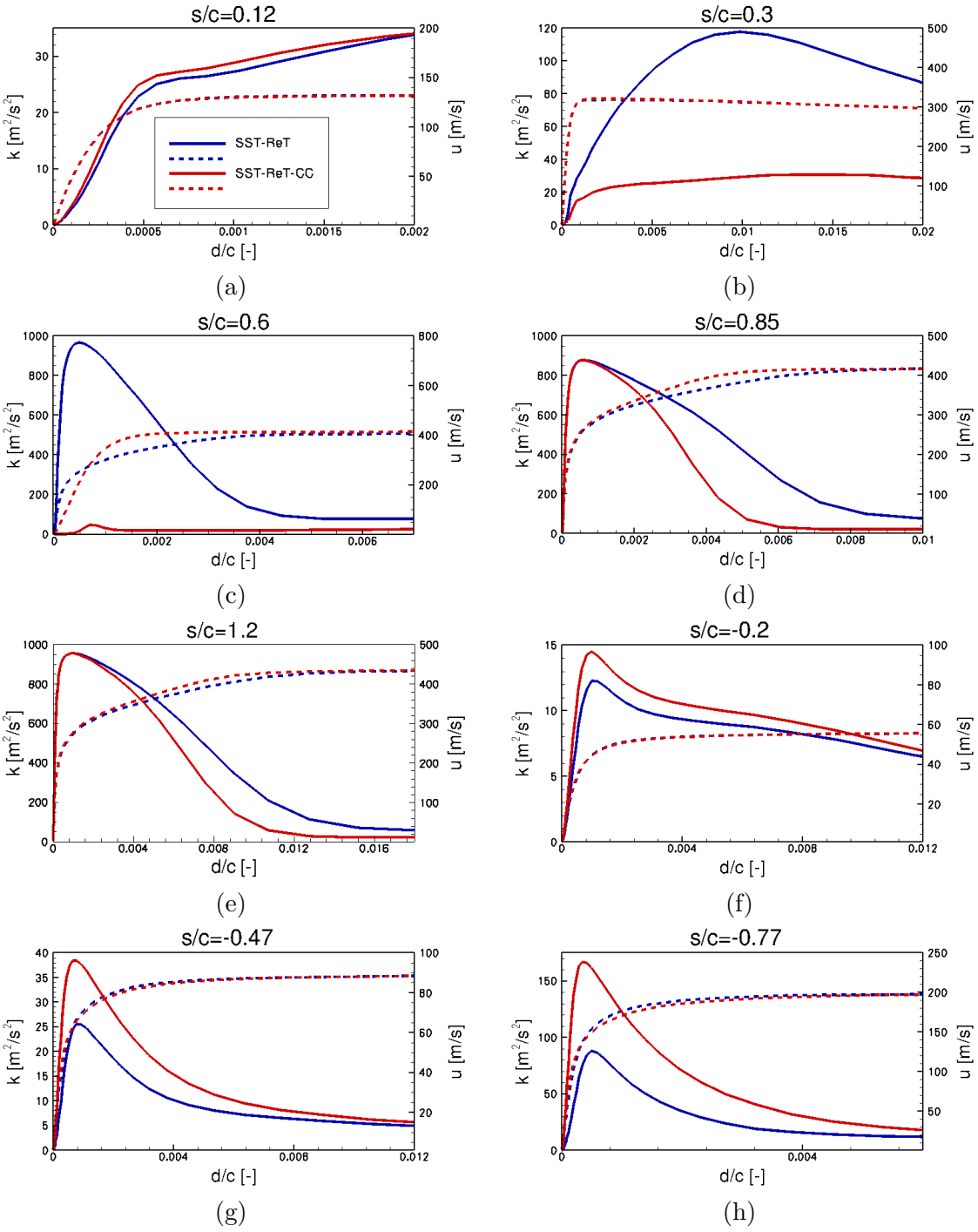

Figure 4-12: Turbulent kinetic energy (solid lines) and velocity distributions (dashed lines) in the normal direction of the surface at different positions over the VKI profile. The distance is normalized by the chord length of the profile.

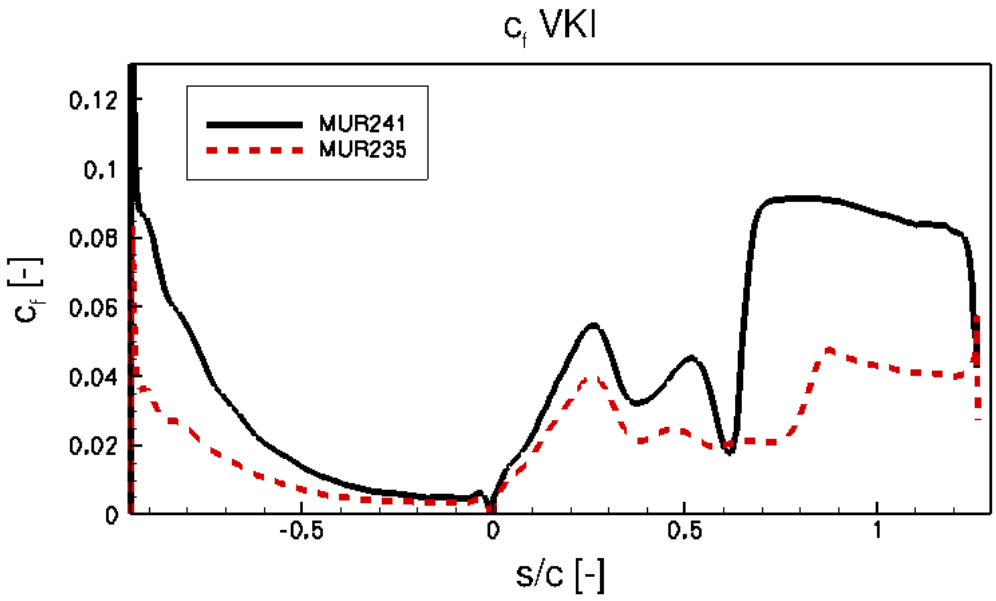

Figure 4-13: Skin friction coefficient over the VKI blade profile for the MUR241 and MUR235 test cases calculated with the SST-ReT-CC method.

Table 4-4: Geometrical characteristics of the T106 low pressure turbine blade.

Parameter	Value	
Chord	99	[mm]
Pitch to chord	0.799	[-]
Stagger angle	59.3^o	[-]
Inlet flow angle	37.7^o	[-]

computational domain, the inlet values of k and ω are first calculated for a straight channel in a pre-processing step. The specific values of the boundary conditions for the T106 test cases are given in Appendix B.

From the previous section it was found that the fully turbulent solution (SST or SST-CC) is not capable of capturing the transition process. For this reason, the present test case is performed only with the numerical models that incorporate the $\gamma - Re_{\theta t}$ transition model (SST-ReT and SST-ReT-CC). The computational domain used for the T106 case (Fig. 4-14) was provided by Dr. Rene Pecnik and it consists of 320 points around the blade surface and 88 points in the normal direction. The maximum value of y^+ at the first cell-row at the blade surface is less than 0.4.

Figures 4-15 and 4-16 show the isentropic pressure coefficient $c_{p,is}$ as a function of the normalized curvilinear coordinate along the blade[1] s/l for the $Tu = 0.5\%$ and the $Tu = 4\%$

[1]This normalization is different to the one used in the VKI test case. The normalization is performed by dividing the position at the suction side and the pressure side by the length of the suction side and the length of the pressure side respectively. This is necessary in order to compare the solutions with the experimental data of Opoka et al. [21]

Table 4-5: Data of the T106A low pressure turbine test cases, where $M_{is,out}$ and $Re_{c,out}$ are the isentropic Mach number and the Reynolds number based on the chord length, both calculated at the outlet region.

	$Tu\%$	$M_{is,out}$	$Re_{c,out}$
Case 1	4.0	0.2986	1.6×10^5
Case 2	0.5	0.2986	1.6×10^5

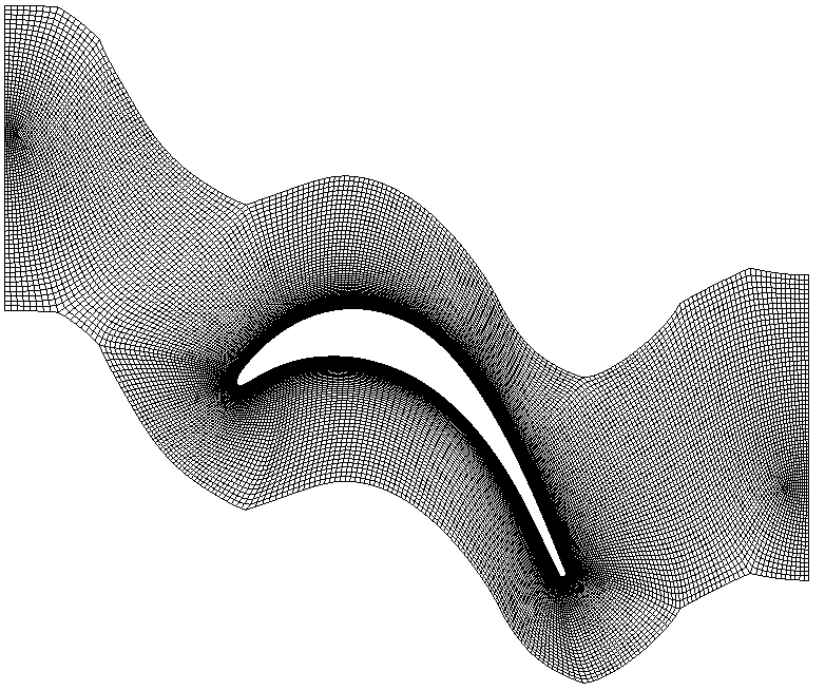

Figure 4-14: Computational domain of the T106 low pressure turbine blade. The computational domain consists of 320 points around the blade surface and 88 points in the normal direction providing a resolution of $y^+ < 0.4$ at the first cell-row over the surface.

test cases. The isentropic pressure coefficient is defined by

$$c_{p,is} = \frac{P_\infty - P}{P_\infty - P_{s2}}, \tag{4-3}$$

where P is the static pressure over the surface, P_∞ is the reference pressure and P_{s2} is the static pressure at the outlet.

From the experimental results it is possible to observe boundary layer separation at $s/l = 0.6$ for the lower turbulence intensity ($Tu = 0.5\%$) case. From this point a pressure *plateau* extends up to a distance $s/l = 0.8$. The end of the pressure plateau indicates the onset of the transition process which manifests through the pressure recovery region. Downstream of $s/l = 0.9$ the boundary layer reattaches. In the higher turbulence intensity ($Tu = 4\%$) case, the distribution of pressure coefficient does not develop a plateau between $s/l = 0.6$ and $s/l = 0.8$, which suggests the absence of a separation bubble.

In general, the numerical results are in good agreement with the experimental data. Moreover, it is possible to observe that the results obtained from the curvature corrected calcula-

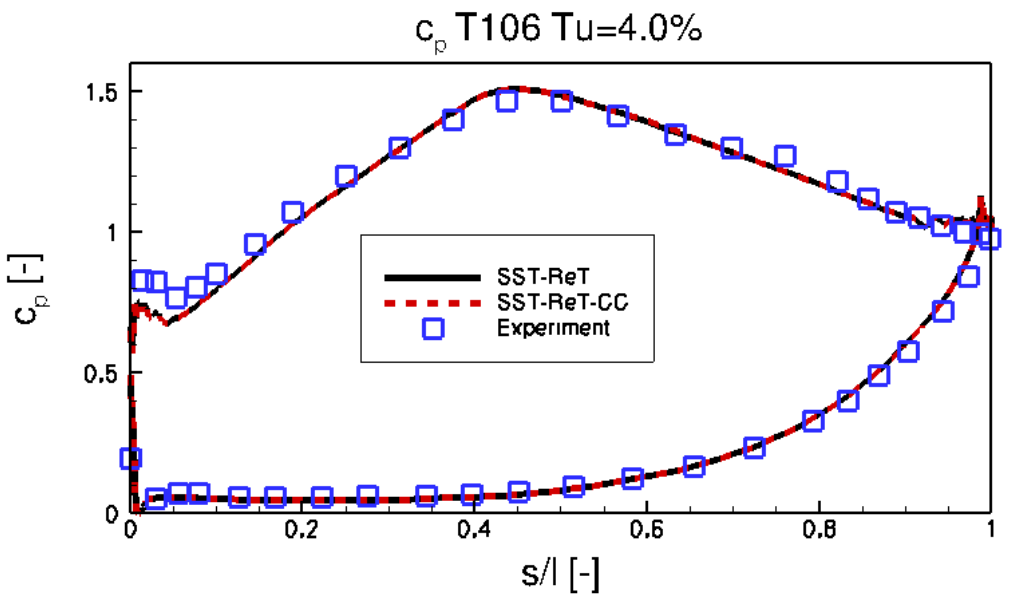

Figure 4-15: Pressure coefficient over the T106 blade profile for the $Tu = 4\%$ test case. The lines represent numerical calculations while the squares represent the experimental results of Opoka et al. The curve on the bottom of the figure corresponds to the pressure side, while the upper one lies on the suction side of the blade.

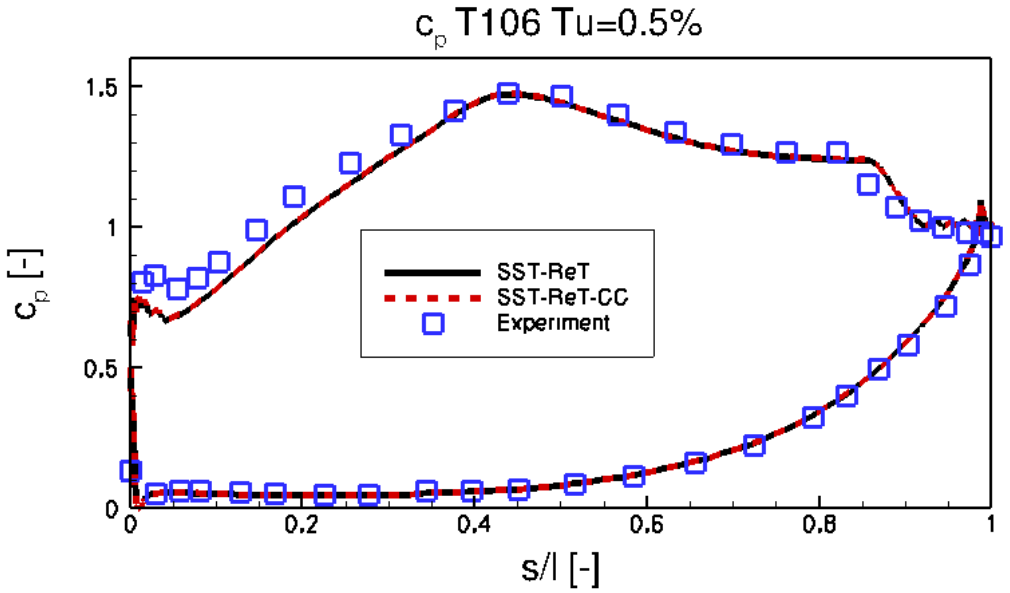

Figure 4-16: Pressure coefficient over the T106 blade profile for the $Tu = 0.5\%$. The lines represent numerical calculations while the squares represent the experimental results of Opoka et al. The curve on the bottom of the figure corresponds to the pressure side, while the upper one lies on the suction side of the blade.

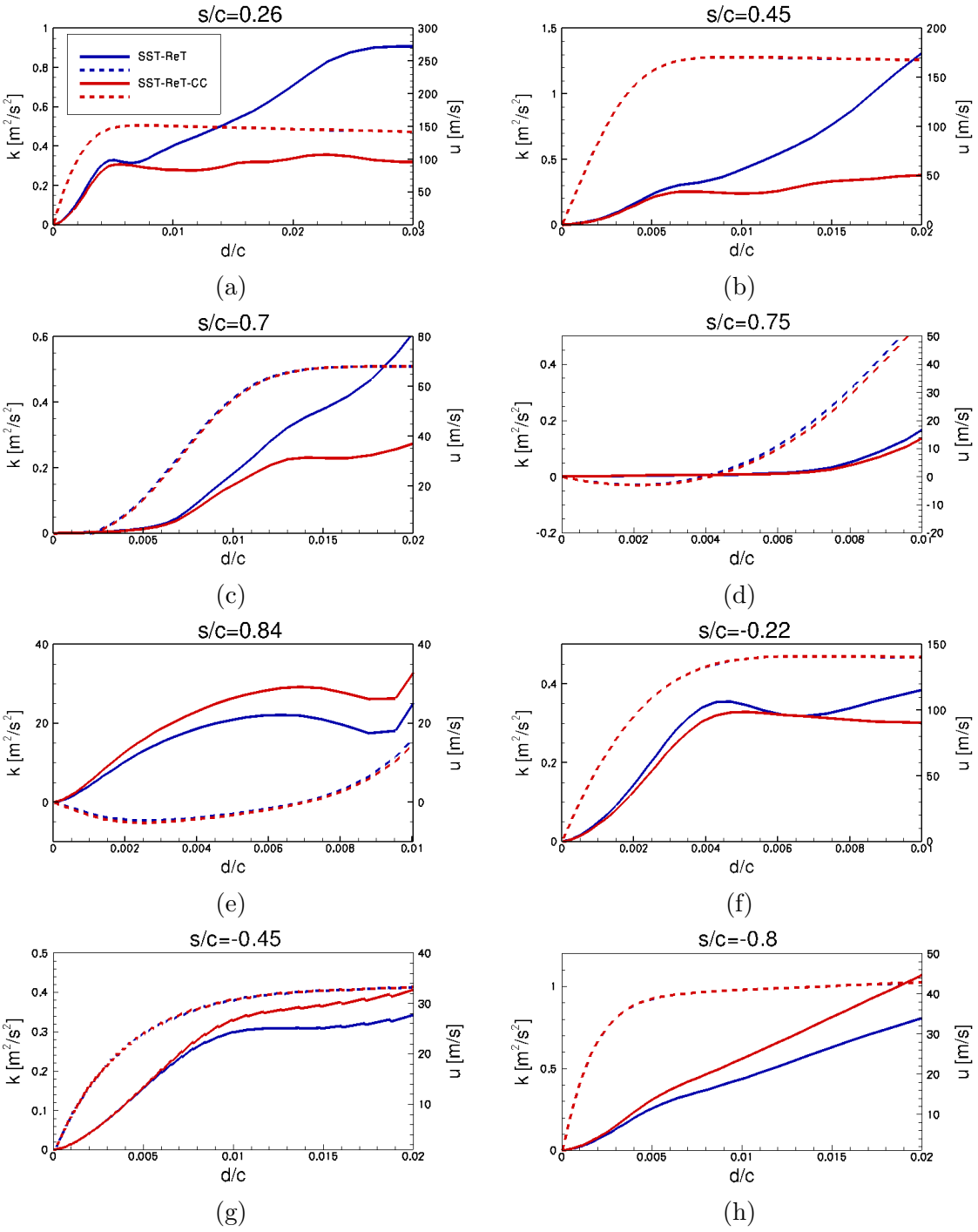

Figure 4-17: Turbulent kinetic energy (solid lines) and velocity distributions (dashed lines) in the normal direction of the surface at different positions over the T106 profile. The distance is normalized by the chord length of the profile.

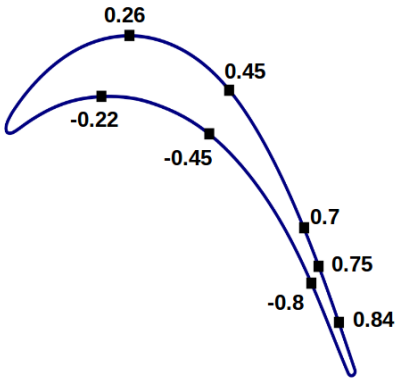

Figure 4-18: Schematic representation of the T106A profile and the different points where the turbulent kinetic energy is calculated.

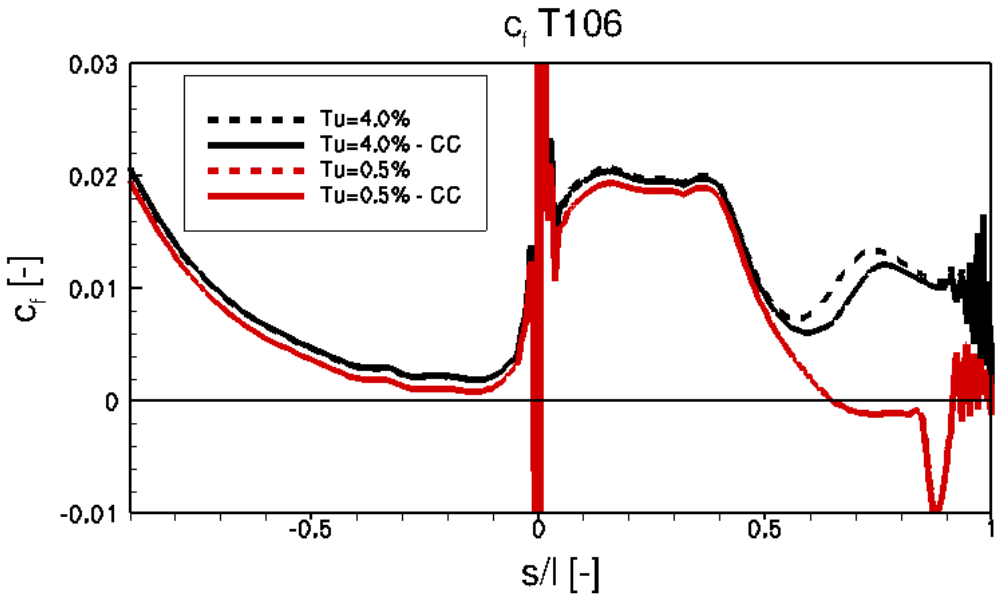

Figure 4-19: Skin friction coefficient over the T106A blade profile for the $Tu = 4.0\%$ and $Tu = 0.5\%$ test cases as a function of the curvilinear coordinate along the blade s/c normalized by the chord. The solid lines represent calculations performed with the SST-ReT-CC model, while the dashed lines are obtained with the SST-ReT scheme. Positive values of s/l indicate the suction side, while negative values of s/l correspond to the pressure side of the blade.

tions (SST-ReT-CC) are the same as from the non-corrected model (SST-ReT). The reason is that, although the boundary layer might separate ($Tu = 0.5\%$), the laminar to turbulent transition occurs in the shear layer above the separation bubble. The increase on turbulent kinetic energy in the boundary layer can be appreciated after the flow reattaches at the very end of the suction side ($s/l = 0.9$). In the case of higher turbulence intensity ($Tu = 4\%$), no transition can be observed over the suction side as the skin friction coefficient changes along the surface are smooth.

Figure 4-17 shows the turbulent kinetic energy and velocity distributions in the normal direction of the surface for the $Tu = 0.5\%$ test case at different positions over the blade, which are schematically indicated in Fig. 4-18. As in the previous VKI test case, it is possible to observe the effect of the curvature correction term within the boundary layer as it increases the turbulent kinetic energy over the pressure side and decreases it over the suction side as compared to the non-corrected solution. Moreover, figures (d)-(e) show the turbulent kinetic energy within the separation bubble. The low values of the turbulent kinetic energy at these positions indicate that no transition occurs across the bubble at this streamwise location.

Figure 4-19 shows the skin friction coefficient for both T106A test cases ($Tu = 4\%$ and $Tu = 0.5\%$) as a function of the curvilinear coordinate s/l. The skin friction coefficient for the low turbulence case becomes negative near the point $s/c = 0.6$ confirming the presence of a separation bubble. For the higher turbulence test case, transition occurs over the suction side of the profile which can be distinguished as a sharp increase of the skin friction coefficient at $s/l = 0.6$. In addition, it can be seen that the curvature corrected solution (CC) shifts the transition onset towards the trailing edge (s/l=1). This effect is the consequence of the curvature correction factor, which decreases the turbulence levels in the boundary layer over a concave surface (suction side). This reduction of the turbulence levels in the boundary layer causes the transition model to trigger the onset further downstream.

Chapter 5

Summary and Conclusions

This thesis presents a thorough analysis of the curvature effects on turbulent flows for turbomachinery applications and documents the steady state simulation of a series of two dimensional test cases characterized by a strong streamline curvature. For this purpose, the Reynolds-Averaged Navier-Stokes (RANS) solver developed by Pecnik et al. [18] is upgraded with two new subroutines which use the local flow field properties, namely the velocity U, the strain tensor S_{ij}, vorticity tensor Ω_{ij} and specific turbulence dissipation rate ω, to calculate the Spalart and Shur [12] curvature correction (CC) term. The correction factor is then implemented in the $k-\omega$ shear stress transport (SST) model of Menter [19] and in the $\gamma - Re_{\theta t}$ (ReT) transition model of Langtry and Menter [8].

The new subroutines are first validated on two well known test cases, namely a subsonic flow over an adiabatic flat plate [22] and the fully turbulent flow inside a U-duct channel [23, 11]. As expected, the results show that the curvature correction term has no effect on the solution of the flat plate test case. For the U-duct channel case, the numerical calculations show that the curvature corrected SST-CC turbulence model agrees better with the experimental data than the original model.
Next, the curvature correction is tested on two well documented turbomachinery test cases. The first one being the prediction of the heat transfer coefficient over a Von Karman Institute (VKI) transonic turbine guide vane [3], and the second the prediction of the pressure coefficient over the high lift T106 low pressure turbine blade [21]. For the VKI test case, two flow configurations (MUR235 and MUR241) are considered, both characterized by the presence of a transition spot over the suction side of the profile. The results show that the SST-CC and the original SST turbulence models overestimate the heat transfer coefficient over the surface of the blade and they are not able to capture the transition process. On the other hand, the results obtained from using the ReT transition model exhibit laminar to turbulent transition over the suction side of the blade and have a better agreement with the experimental data. However, the transition point is still located too far upstream when compared to the experimental values. The results obtained by the curvature corrected ReT model present a significant improvement with respect to the original ReT model as the curvature correction term reduces the turbulence levels over the suction side which cause the transition model to

trigger the onset further downstream.
Finally, the high lift T106 low pressure turbine blade is considered for two different turbulence intensities: $Tu = 4\%$ and $Tu = 0.5\%$. In the case of high freestream turbulence, transition occurs before the boundary layer separates. However, for the lower freestream turbulence case the boundary layer separates and transition occurs in the shear layer above the laminar separation bubble. Here, the transition model is essential for the predictive capability of the simulation and the results are in good agreement with experimental data. For the two different flow configurations no significant improvements are observed when using the curvature correction term.

In this work it has been shown that turbulence in a boundary layer entering a convex curve is diminished by the centrifugal acceleration, while the turbulence of a flow entering a concave surface is amplified. The curvature correction term interacts with the SST turbulence model by modulating the turbulent kinetic energy production. This is particularly beneficial for the ReT transition model performance, which is based on empirical correlations obtained from flat plate experimental data. For a convex surface it has been found that the original SST turbulence model overpredicts the value of the turbulent kinetic energy which leads to an early prediction of the transition point by the ReT model. The effect of the curvature correction term is to reduce the turbulent kinetic energy within the boundary layer delaying the transition point further downstream. On the other hand, the original SST model underpredicts the turbulent kinetic energy over a concave surface. For this reason, although none of the test cases in the present thesis exhibits transition over a concave surface, a delayed transition onset can be expected from the ReT transition model if the curvature correction is not used.

In general, the results obtained in this work show a positive effect of the curvature correction on the flow solutions. Furthermore, the additional computational cost of calculating the correction term is not significant as compared to the operations required by the solver, as the complexity of the algorithm is linear (i.e. the amount of operations is proportional to the number of cells in the computational domain). It is necessary to notice that the curvature correction proposed by Spalart and Shur [12] has been originally developed for weak rotation or curvature. As none of the present test cases exhibit system rotation it becomes necessary to further assess the predictive capability of the correction term by including this effect. In addition, the upper and lower limits of the curvature correction are based on the tests performed by Smirnov and Menter [11]. For this reason, a recalibration of these limits must be considered when applying the curvature correction for turbomachinery test cases .

Appendix A

Subroutines to calculate the Spalart and Shur Correction Term

In the present chapter the subroutines to calculate the Spalart and Shur correction term implemented in the RANS solver are presented. The first subroutine is used to calculate the $\frac{DS_{ij}}{Dt}$ (Equation 2-62) over each cell center of the grid:

```
1
2       virtual void shearstressface()
3       {
4
5         int oo,ii;
6         double d1,d2,VA1,VA2;
7
8          for (int i=0; i<ncv; i++)
9          for (int j=0; j<3; j++)          //Set dsdt to 0 for each time
               step
10         for (int k=0; k<3; k++)
11           {
12          dsdt[i][j][k]=0;
13           }
14
15      //INTERNAL FACES
16      for (int i=nfa_b; i<nfa; i++)           //Recalculate dsdt for the
            new time step
17      {
18
19       oo=cvofa[i][0];
20       ii=cvofa[i][1];
21       d1=sqrt(pow(x_cv[oo][0]-x_fa[i][0],2.0)+pow(x_cv[oo][1]-x_fa[i
             ][1],2.0)+pow(x_cv[oo][2]-x_fa[i][2],2.0));
22       d2=sqrt(pow(x_cv[ii][0]-x_fa[i][0],2.0)+pow(x_cv[ii][1]-x_fa[i
             ][1],2.0)+pow(x_cv[ii][2]-x_fa[i][2],2.0));
23
```

```
24
25      double vel_fa[3];         //VELOCITY AVERAGE
26      double vel_fa0[3];
27      double vel_fa1[3];
28      for (int j=0; j<3; j++){
29      vel_fa0[j]=vel[oo][j]+grad_u[oo][j][0]*(x_fa[i][0]-x_cv[oo][0])+
            grad_u[oo][j][1]*(x_fa[i][1]-x_cv[oo][1])+grad_u[oo][j][2]*(x_fa[
            i][2]-x_cv[oo][2]);
30      vel_fa1[j]=vel[ii][j]+grad_u[ii][j][0]*(x_fa[i][0]-x_cv[ii][0])+
            grad_u[ii][j][1]*(x_fa[i][1]-x_cv[ii][1])+grad_u[ii][j][2]*(x_fa[
            i][2]-x_cv[ii][2]);
31      }
32
33
34
35      for (int j=0; j<3; j++){
36      vel_fa[j]= (vel_fa0[j]*d2+vel_fa1[j]*d1)/(d2+d1);
37      }
38
39      VA1 =  (vel_fa[0]*fa_normal[i][0]+vel_fa[1]*fa_normal[i][1]+vel_fa
            [2]*fa_normal[i][2])/cv_volume[oo];
40      VA2 =  (vel_fa[0]*fa_normal[i][0]+vel_fa[1]*fa_normal[i][1]+vel_fa
            [2]*fa_normal[i][2])/cv_volume[ii];
41
42          for (int j=0; j<3; j++)
43          for (int k=0; k<3; k++)
44            {
45              dsdt[oo][j][k]+= (0.5*(grad_u[oo][j][k]+grad_u[oo][k][j])*d2
                    +0.5*(grad_u[ii][j][k]+grad_u[ii][k][j])*d1)*VA1/(d2+d1);
                      //dsdt_node=dsdt_node-Sij*VA/vol_node
46              dsdt[ii][j][k]-= (0.5*(grad_u[oo][j][k]+grad_u[oo][k][j])*d2
                    +0.5*(grad_u[ii][j][k]+grad_u[ii][k][j])*d1)*VA2/(d2+d1);
47            }
48
49      }
50
51    //BOUNDARY FACES
52     for (int i=0; i<nfa_b; i++)
53      {
54      oo=cvofa[i][0];
55      VA1 =  (vel_bfa[i][0]*fa_normal[i][0]+vel_bfa[i][1]*fa_normal[i][1]+
            vel_bfa[i][2]*fa_normal[i][2])/cv_volume[oo];
56              for (int j=0; j<3; j++)
57              for (int k=0; k<3; k++)
58                   {
59                   dsdt[oo][j][k]=dsdt[oo][j][k] + (0.5*(grad_u[oo][j][k]+
                        grad_u[oo][k][j]))*VA1;
60                   }
61      }
62
63  }
```

Once the total derivative of the strain tensor $\frac{DS_{ij}}{Dt}$ has been computed over every cell center of the mesh, the following subroutine is used to evaluate the curvature correction term f_r (equations 2-48 and 2-49) at every cell center of the grid.

```
1     virtual void CurvatureCorrection(int icv)
2     {
3         double f_rotation,norm_s,norm_om,r_tilde,r_star,D;
4         double c1=1,c2=2,c3=1;
5
6           norm_s  = 0;
7           norm_om = 0;
8
9                for (int j=0; j<3; j++)          //Set dsdt to 0 for each
                     time step
10               for (int k=0; k<3; k++)
11                 {
12                Aux1[icv][j][k]=0;
13                 }
14
15
16          r_tilde = 0;
17
18            for (int f=0;f<3;f++){                    //Here compute S
                  and Omega
19            for (int g=0;g<3;g++){
20              s[icv][f][g]  = 0.5*(grad_u[icv][f][g]+grad_u[icv][g][f]);
21              om[icv][f][g] = 0.5*(grad_u[icv][f][g]-grad_u[icv][g][f]);
22            }  }
23
24            for (int f=0;f<3;f++){                    //Here compute S
                  and Omega norm
25            for (int g=0;g<3;g++){
26              norm_om = norm_om + om[icv][f][g]*om[icv][f][g];
27              norm_s  = norm_s  + s[icv][f][g]*s[icv][f][g];
28            }}
29              norm_om = sqrt(2*norm_om);
30            norm_s  = sqrt(2*norm_s);
31              D       = sqrt(max(norm_s*norm_s,0.09*omega[icv]*omega[icv
                    ]));
32              r_star  = norm_s/norm_om;
33
34            for (int i=0;i<3;i++){                    //Here compute
                  omega_ik*S_jk=omega_ik*S_kj=Aux_ij
35            for (int j=0;j<3;j++){
36              for (int k=0;k<3;k++){
37               Aux1[icv][i][j]=Aux1[icv][i][j]+om[icv][i][k]*s[icv][j][k
                    ];
38            }}}
39
40            for (int f=0;f<3;f++){                    //Here compute
                  Aux1_ij*dsdt_ij=f
41            for (int g=0;g<3;g++){
42              r_tilde  = r_tilde  + 2*Aux1[icv][f][g]*dsdt[icv][f][g];
```

```
43              }  }
44              r_tilde = r_tilde/(norm_om*pow(D,3));
45
46                f_rotation = (1+c1)*(2*r_star/(1+r_star))*(1-c3*atan(c2*
                    r_tilde))-c1;
47                f_r1[icv] = max(min(f_rotation,1.25),0.0);
48
49      }
```

Appendix B

Additional Test Case Data

For the sake of completeness, the particular values of the boundary conditions used for the different test cases of this thesis are presented in this appendix. Tables B-1 to B-3 show the values of the boundary conditions used for the flat plate, the U-duct channel and the straight channel. The turbomachinery test cases, namely the VKI transonic turbine guide vane and the T106 low pressure turbine blade are summarized in table B-4.

Table B-1: Boundary conditions used for the T3A flat plate test case.

Boundary	**Parameter**	**Value**
Reference Values	ρ_∞ [kg/m^3]	1.2
	P_∞ [Pa]	101634
	T_∞ [K]	293.1
	μ_∞ [Pa·s]	6.743e-05
Inlet	P_{in} [Pa]	101634
	T_{in} [K]	293.1
	k_{in} [m^2/s^2]	30
	ω_{in} [1/s]	40000
Outlet	P_{out} [Pa]	0.953e5
Wall	Type	Adiabatic
	U_{wall} [m/s]	0
	k_{wall} [m^2/s^2]	0

Table B-2: Boundary conditions used for the straight channel.

Boundary	Parameter	Value
Reference Values	ρ_∞ [kg/m^3]	15.1
	P_∞ [Pa]	12e5
	T_∞ [K]	277.1
	μ_∞ [Pa·s]	1.841e-5
Inlet/Outlet	ΔP [Pa]	1113
Wall	Type	Adiabatic
	U_{wall} [m/s]	0
	k_{wall} [m^2/s^2]	0

Table B-3: Boundary conditions used for the U-duct channel test case. At the inlet section, fully developed profiles of velocity, density and turbulence properties were calculated for a straight channel in a pre-processing step and then specified as the boundary condition.

Boundary	Parameter	Value
Reference Values	ρ_∞ [kg/m^3]	15.08
	P_∞ [Pa]	12e5
	T_∞ [K]	277.1
	μ_∞ [Pa·s]	1.841e-5
Inlet	U_{in} [m/s]	Straight channel
	ρ_{in} [kg/m^3]	Straight channel
	k_{in} [m^2/s^2]	Straight channel
	ω_{in} [1/s]	Straight channel
Outlet	P_{out} [Pa]	12e5
Wall	Type	Adiabatic
	U_{wall} [m/s]	0
	k_{wall} [m^2/s^2]	0

Table B-4: Boundary conditions used for the turbomachinery test cases, namely the VKI transonic turbine guide vane (MUR235 and MUR241) and the T106 low pressure turbine blade (Tu=0.5% and Tu=4.0%).

Boundary	Parameter	MUR235	MUR241	T106 (Tu=0.5%)	T106 (Tu=4.0%)
Reference Values	ρ_∞ [kg/m^3]	1.54	2.72	0.574	0.574
	P_∞ [Pa]	1.828e5	3.257e5	1e5	1e5
	T_∞ [K]	416.3	416.3	606.5	606.5
	μ_∞ [Pa·s]	1.716e-5	1.716e-5	4.971e-5	4.971e-5
Inlet	P_{in} [Pa]	1.828e5	3.257e5	1e5	1e5
	T_{in} [K]	416.3	416.4	606.5	606.5
	k_{in} [m^2/s^2]	20.55	20.55	0.18	15
	ω_{in} [1/s]	5e4	1.1e5	170	170
Outlet	P_{out} [Pa]	1.049e5	1.547e5	0.94e5	0.94e5
Wall	T_{wall} [K]	300.0	300	606.5	606.5
	U_{wall} [m/s]	0	0	0	0
	k_{wall} [m^2/s^2]	0	0	0	0

Bibliography

[1] M. Finnis and A. Brown, "Stability of a laminar boundary layer flowing along a concave surface," *Journal of Turbomachinery*, vol. 111, pp. 376–386, 1989.

[2] P. Dubrin and B. P. Reif, *Statistical Theory and Modeling for Turbulent Flows*. John Wiley and Sons, 2010.

[3] T. Arts and M. L. de Reuvroit, "Aero-thermal performance of a two-dimensional highly loaded transonic turbine nozzle guide vane: A test case for inviscid and viscous flow computations," *Journal of Turbomachinery*, vol. 114, pp. 147–154, 1992.

[4] R. Pecnik, J. A. Witteveen, and G. Iaccarino, "Assessment of uncertainities in modeling of laminar to turbulent transition for transonic flows," *Flow Turbulence and Combustion*, vol. 91, pp. 41–61, 2013.

[5] G. Nowak and W. Wroblewski, "Optimization of blade cooling system with use of conjugate heat transfer approach," *International Journal of Thermal Sciences*, vol. 50, pp. 1770–1781, 2011.

[6] R. Langtry and F. Menter, "Transition modeling for general cfd applications in aeronautics," *American Institute of Aeronautics and Astronautics*, vol. 522, pp. 1–14, 2005.

[7] R. B. Langtry, *A Correlation-Based Transition Model using Local Variables for Unstructured Parallelized CFD codes*. PhD thesis, Universitat Stuttgart, 2006.

[8] R. B. Langtry and F. R. Menter, "Correlation-based transition modeling for unstructured parallelized computational fluid dynamics codes," *American Institute of Aeronautics and Astronautics Journal*, vol. 47 No. 12, p. 2894, 2009.

[9] W. Elsner, "Transition modelling in turbomachinery," *Journal of theoretical and applied mechanics*, vol. 45, pp. 539–556, 2007.

[10] M. Shur, M. Strelets, A. Travin, and P. Spalart, "Turbulence modelling in rotating and curved channels: Assessing the spalart-shur correction," *American Institute of Aeronautics and Astronautics*, vol. 38 No.5, pp. 784–792, 2000.

[11] P. E. Smirnov and F. R. Menter, "Sensitization of the sst turbulence model to rotation and curvature by applying the spalart-shur correction term," *Journal of Turbomachinery*, vol. 131, pp. 041010–1, 2009.

[12] P. Spalart and M. Shur, "On the sensitization of turbulence models to rotation and curvature," *Aerospace Science and Technology*, vol. 5, p. 297, 1997.

[13] M. Clauser and F. Clauser, "The effect of curvature on transition from laminar to turbulent boundary layer.," tech. rep., NACA TN 613, 1937.

[14] H. Gortler, "On the three dimensional instability of laminar boundary layers on cancave walls," tech. rep., NACA TM 1375, 1940.

[15] L. Han and W. Cox, "A visual study of turbine blade pressure-side boundary layers," *Journal of Engineering for Power*, vol. 105, pp. 47–52, 1983.

[16] J. Howard, S. Patankar, and R. Bordynuik, "Flow prediction in rotating ducts using coriolis-modified turbulence models," *Journal of Fluids Engineering*, vol. 102, pp. 456–461, 1980.

[17] B. Launder, C. Priddin, and B. Sharma, "The calculation of turbulent boundary layers on spinning and curved surfaces," *Journal of Fluids Engineering*, vol. 99 No. 1, pp. 231–239, 1977.

[18] R. Pecnik, V. E. Terrapon, F. Ham, G. Iaccarino, and H. Pitsch, "Reynolds-averaged navier-stokes simulations of the hyshot ii scramjet," *American Institute of Aeronautics and Astronautics*, vol. 50 no. 8, p. 1717âĂŞ1732, 2012.

[19] F. R. Menter, "Two-equation eddy-viscosity turbulence models for engineering applications," *American Institute of Aeronautics and Astronautics Journal*, vol. 32 No 8, p. 1298, 1994.

[20] R. E. Mayle, "The role of laminar-turbulent transition in gas turbine engines," *Journal of Turbomachinery*, vol. 113, pp. 509–536, 1991.

[21] M. Opoka, R. Thomas, and H. Hodson, "Boundary layer transition on the high lift t106a low pressure turbine blade with an oscillating downstream pressure field," *Journal of Turbomachinery*, vol. 130, pp. 1–10, 2008.

[22] A. Savill, *Numerical Simulation of Unsteady Flows and Transition to Turbulence*, ch. A Synthesis of t3 Test Case Predictions, pp. 404–442. Cambridge University Press, 1992.

[23] D. Monson, H. Seegmiller, P. M. Connaughey, and Y. Chen, "Comparison of experiment with calculations using curvature corrected zero and two equation turbulence models for a two-dimensional u-duct," *American Institute of Aeronautics and Astronautics*, vol. 90-1484, pp. 1–19, 1990.